This is to certify that the
dissertation entitled

Exploring the Milky Way Halo with SDSS-II SN Survey RR Lyrae Stars

presented by

Nathan De Lee

has been accepted towards fulfillment
of the requirements for the

Ph.D. degree in Physics and Astronomy

Horace A. Smith
Major Professor's Signature

7/25/08

Date

PLACE IN RETURN BOX to remove this checkout from your record.
TO AVOID FINES return on or before date due.
MAY BE RECALLED with earlier due date if requested.

DATE DUE	DATE DUE	DATE DUE
MAR 14 2013		

EXPLORING THE MILKY WAY HALO WITH SDSS-II SN SURVEY RR LYRAE STARS

By

Nathan De Lee

A DISSERTATION

Submitted to
Michigan State University
in partial fulfillment of the requirements
for the degree of

DOCTOR OF PHILOSOPHY

Department of Physics and Astronomy

2008

ABSTRACT

EXPLORING THE MILKY WAY HALO WITH SDSS-II SN SURVEY RR LYRAE STARS

By

Nathan De Lee

This thesis details the creation of a large catalog of RR Lyrae stars, their lightcurves, and their associated photometric and kinematic parameters. This catalog contains 421 RR Lyrae stars with 305 RRab and 116 RRc. Of these, 241 stars have stellar spectra taken with either the Blanco 4m RC spectrograph or the SDSS/SEGUE survey, and in some cases taken by both. From these spectra and photometric methods derived from them, an analysis is conducted of the RR lyrae's distribution, metallicity, kinematics, and photometric properties within the halo.

All of these RR Lyrae originate from the SDSS-II Supernova Survey. The SDSS-II SN Survey covers a 2.5 degree equatorial stripe ranging from -60 to +60 degrees in RA. This corresponds to relatively high southern galactic latitudes in the anti-center direction. The full catalog ranges from g_0 magnitude 13 to 20 which covers a distance of 3 to 95 kpc from the sun.

Using this sample, we explore the Oosterhoff dichotomy through the $\Delta \log P$ method as a function of $|Z|$ distance from the plane. This results in a clear division of the RRab stars into OoI and OoII groups at lower $|Z|$, but the population becomes dominated by OoI stars at higher $|Z|$.

The idea of a dual halo is explored primarily in the context of radial velocity distributions as a function of $|Z|$. In particular, V_{gsr}, the radial velocity in the galactic standard of rest, is used as a proxy for V_{ϕ}, the cylindrical rotational velocity. This is then compared against a single halo model galaxy, which results in very similar

V_{gsr} histograms for both at low to medium $|Z|$. However, at high $|Z|$ there is a clear separation into two distinct velocity groups for the data without a corresponding separation in the model, suggesting that at least a two-component model for the halo is necessary.

The final part of the analysis involves [Fe/H] measurements from both spectra and photometric relations cut in both $|Z|$ and radial velocity. In this case, there is less of a clear change as a function of these cuts, although that may be due to metallicity effects on the shape of the horizontal branch. The metallicity groups may be truncated at both the metal-rich and metal-poor end of the histograms because at those metallicities the horizontal branch stars may occur primarily out of the instability strip, removing them from our sample.

To Mom and Dad

ACKNOWLEDGMENTS

There are many people I would like to thank for helping make this possible. Of course my advisers Horace Smith and Timothy Beers, whose invaluable guidance was key to the success of this project. I would also like to thank all those who did work at the 24inch telescope for providing a basis to test some of the relationships used in this work. I am deeply indebted to Young-Sun Lee for all of his help in processing SDSS data as well as helping me understand the field of galactic structure generally. Ronald Wilhelm for his help with the RR Lyrae metallicities. Suzanne Hawley and Andrew West for providing the single-epoch spectra so critical to this work. My collaborators at Cambridge University and the Univ. of Washington, without their photometric catalogs, there would be no RRL survey. Barbara Anthony-Twarog and Bruce Twarog for starting me on the path of Astronomy in the first place. Chris Waters and Adam Kraus for their insight into statistics. Thanks to Cluze for listening to my endless talking about this, and finally, Shannon Bell for her patience and keeping me on task till the end. Thanks to Christopher Waters for the LaTeX class used to format this thesis.

TABLE OF CONTENTS

LIST OF TABLES

LIST OF FIGURES

Images in this dissertation are presented in color.

LIST OF SYMBOLS

CHAPTER 1: INTRODUCTION

The Milky Way galaxy has been an eternal backdrop to our stories, our myths, and our lives since time immemorial. Yet, it was not until relatively recently, only since the early decades of the last century, that we've begun to understand what it is and as a result, understand our place in the universe. It has not been because of a lack of interest or intellect that the questions surrounding the nature of our galaxy have been so hard to answer. Rather it is because the Earth is embedded in the Milky Way's spiral disk. The problem with being in the disk of the Milky Way is two-fold. The first issue is that there is a large amount of dust that absorbs light in the disk, so there is a visual limit to what we can observe. This can be avoided to some extent by going to redder wavelengths, but it is still a problem. The second issue, and by far the most problematic, is that we have only one vantage point. The farthest human technology has ever made it is to the very edge of our solar system, which from a galactic stand-point, is an insignificant distance. This leads to the great irony that we know quite a lot about the structure of other galaxies, millions of parsecs (1 pc $\sim 10^{16}$ meters) away, but have only in the last few years begun to understand the structure of our home.

One major component of the Milky Way is the galactic halo. It is a spherically distributed collection of stars that engulfs the more familiar disk of the Milky Way. It is composed primarily of older stars that are on a random collection of orbits, although there are definite kinematically defined structures. These structures, or streams are likely the result of the our galaxy cannibalising smaller, dwarf galaxies. Beyond this, there is still rigorous debate about the particulars of the populations of stars that the halo contains, how it was formed, and what it's exact structure is.

One method of tracing the structure of the halo is to use some sort of object as a test particle. One kind of object that is useful for this purpose is an RR Lyrae star. RR Lyrae stars are radially pulsating stars, that have a known intrinsic brightness. As they pulsate their brightness changes, tracing out a lightcurve in less than a day. These properties are important because it means that not only are they identifiable by their lightcurve shape, but since their intrinsic brightness is known, the distance to them can be calculated. Distances are a precious commodity in astronomy since the sky is basically a two-dimensional projection of three-dimensional space. One of the fundamental questions in mapping any object is knowing the distance from one place to another, and RR Lyrae are one of the few tools that can serve that purpose well.

The purpose of this work is two-fold. The first is to create a catalog of RR Lyrae stars with complete lightcurves in the five SDSS filters *ugriz*. This catalog will also include photometric parameters such as the period of pulsation for each star, as well as observed brightness, and thus distance. For a substantial part of the catalog there will be additional information about the kinematics of the RR Lyrae and their chemical composition. The second purpose of this work is to use this catalog to investigate the structure of the halo. The main question is the following: "Is the halo a single coherent object, or does it contain two or more discrete parts?" The following chapters will discuss the previous work on this subject, how the catalog was made, and, ultimately, what the analysis shows.

CHAPTER 2: GALACTIC FORMATION AND STRUCTURE

In this chapter, the current picture of the Milky Way galaxy and our understanding on how it was formed will be explored. This is meant as an overview, and as such will not worry too much about the details of the current work in these fields. In the case of the halo, however, particular attention will be paid to its structure and even more so to formation models.

2.1 THE CANONICAL STRUCTURE OF THE MILKY WAY

The Milky Way is a barred-spiral galaxy composed of three distinct luminous parts, each representing very different populations of stars, and each with it's own structure and formation history. Figure 2.1 gives a schematic break down of the Milky Way. Each of these parts: the bulge, the disk, and the halo will be considered in turn in the following sections.

2.1.1 BULGE

The bulge of the Milky Way is located at the very center of the galaxy. It is a bar-shaped region with an axial ratio of 1:0.35:0.26 (Rattenbury et al., 2007). This region contains a population of stars the covers a wide range in metallicity $-1.5 \leq$ [Fe/H] ≤ 0.75 (Zoccali et al., 2008). The metallicity, [Fe/H], is a shorthand method

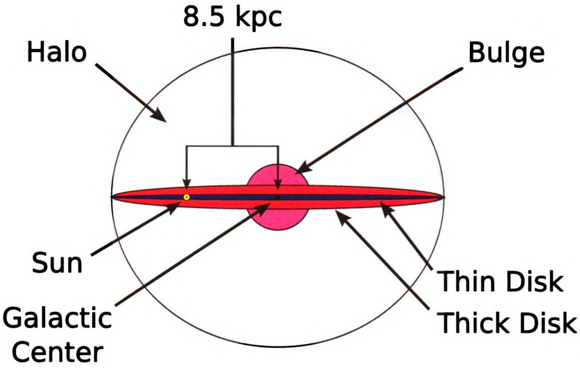

Figure 2.1 A schematic version of the Milky Way labeling the many constituents including the bulge, the disk, and the halo.

of describing the amount of non-primordial elements in a star. It is usually defined as the logarithm of the ratio of number density of Fe to H in a star compared to that value in the Sun, or $\log(N_{Fe}/N_H)_{star} - \log(N_{Fe}/N_H)_{\odot}$. In general, most of the other elements not generated in the big bang track the iron to hydrogen ratio. The mean metallicity of the Bulge is around +0.25, which is roughly twice as metal rich as the Sun. The bulge is filled with stars of a wide variety of ages. This may be due to a series of star formation epochs or intermixing between the bulge and the disk. The bulge rotates with a peak velocity of 75 km/s and exists as an intermediate between a purely rotating disk and the much more kinematically hot halo (Minniti & Zoccali, 2007). In general it is relatively hard to work on things in the bulge because there is a large amount of interstellar dust along the line of sight toward the galactic center, which blocks our view, especially in the optical wavelengths, although recent advances with infrared observatories have opened up the field.

2.1.2 Disk

The disk is the part of the galaxy most familiar to the public. Its spiral arms perhaps being the component that most catches the eye. Of course there are no face-on images of the Milky Way, since the Sun is located in the disk, so our mental construct of what the disk looks like is formed from a combination of observational data and analogy to other spiral galaxies. The disk itself is composed of a series of substructures of different ages and components. The young thin disk is very metal-rich with $[Fe/H] > +0.1$, with a scale height of 50pc , and is the site of current star formation. The old thin disk has a scale height of 325pc and is a little more metal poor with $-0.5 < [Fe/H] < +0.3$. The final component is the thick disk which is more metal-poor with an $-1.6 < [Fe/H] - 0.4$ and a scale height of 1.4 kpc (Ostlie & Carroll, 1996).

2.1.3 Halo

The halo is one of the oldest and most metal-poor, although arguably the most complex, component of the galaxy. It is roughly spherical and is kinematically distinguished by being mostly non-rotating and having high velocity dispersions. For some time it has been known that the halo consists of two parts, an inner and an outer halo, although the origins and distinction between them has been in dispute. In general, the inner halo is taken to be flattened with an axial ratio between 0.6 and 0.7 (Helmi, 2008). The outer halo is much more spherical with an axial ratio of ≈ 1. There is also a significant dark matter component to the halo. The dark matter component of the galaxy cannot radiate away its energy since it only interacts gravitationally, and as a result it is the dominant source of mass in the halo. One of the major differences between older and more recent models of halo formation is the consideration of the dark matter component of the halo. In the following sections, we will discuss the formation and structure of the halo.

2.2 Formation Models of the Milky Way Halo

The question of how the Milky Way halo formed is still an open area of research, and is the question that this work will ultimately address. There are few fields in science where one can find referenced work back to the 18th century, but this is one such place. In particular, Immanuel Kant in his 1755 treatise *Universal Natural History and Theory of the Heavens* discussed the formation of the galaxy from a more dispersed state under the influence of gravity. Since then, there have been a number of theories over the years and in the following section we will discuss the canonical papers and more recent work.

2.2.1 ELS

One of the first major attempts to understand the formation history of the halo based on observations of halo stars was by Eggen, Lynden-Bell & Sandage (1962) or ELS. Eggen et al. (1962) put forward the idea that the interaction time scale between stars and the galaxy is long compared to the age of the galaxy. Thus it should be possible to reconstruct the original dynamics of the proto-galaxy by looking at old stars. They examined the full space motions (U,V,W) of 221 dwarf stars in the solar neighborhood using information about their orbits and their metallicity to determine where they initially formed.

The metallicity of a star is a measurement of the fraction all elements heavier than hydrogen and helium in that star. These heavier elements are referred to collectively as metals. Knowing the metallicity of a star tells one two things; first it gives some suggestion as to the interstellar medium that the star was formed from. Different stellar formation sites tend to have a particular metallicity, for instance all the stars in a given globular cluster have the same metallicity. The second is that metallicity can be used as an age dating device. Since only hydrogen and helium (with a small amount of lithium and other light elements) were created in the Big Bang, all other elements must have been created by processes since then. The primary site for this is the nuclear fusion that powers stars. These elements are then released into the surrounding medium by supernova explosions. As time progresses, more metals are injected into the interstellar medium (ISM) and the stars that form from this ISM have a higher metallicity. It should be noted that the metallicity of a star does not in general change over time, so the metallicity is a measurement of the metal abundance of the local ISM when and where the star was born. Thus on average low metallicity stars tend to be old, and high metallicity stars tend to be young.

To get metallicities, ELS used a technique called the ultra-violet excess, δ(U-B), which compares the difference in the (U-B) color of a star against what would be expected from a (U-B) versus (B-V) color-color diagram of the Hyades open cluster. A higher δ(U-B) is indicates a lower metallicity. Their first area of study was to look at the eccentricities of the orbits of their sample stars. They observed was that δ(U-B) was highly correlated with the eccentricity of a star's orbit which implied that eccentricity is correlated with age. Furthermore, they found the maximum Z, vertical height above the disk, for metal-rich stars tends to be near the plane (disk) of the Milky Way, while metal-poor stars can be found at all heights.

In their model for Galaxy formation, the Galaxy starts as a large self-gravitating cloud of gas that condenses down forming stars and ultimately the disk of the Milky Way. Once a star forms, it only interacts by gravity, so its orbit tends to maintain the kinematics of the gas it formed from. Gas, on the other hand, can interact through friction, and so tends to lose energy and angular momentum over time.

Using this information, ELS came up with the following scenario. A large gas cloud roughly 10^{10} years ago began to collapse. The first stars began to form, as well as the globular clusters, and as the stars formed they would have eccentric orbits depending on their location in the cloud. As time progressed, the remaining gas continued to contract while radiating away energy, and centrifugal forces led to the formation of the disk. This then is where the second batch of stars formed with higher metallicity and now relatively circular orbits.

This scenario predicts that there should be a relationship between [Fe/H] and galactic radius and that overall there should be a small range in ages for halo objects. However, more recent work has suggested that there was perhaps a bias in the sample of stars used by ELS (Chiba & Beers, 2000 and references therein).

2.2.2 SZ

ELS reigned as the primary description of the formation of the Galaxy until a paper by Searle & Zinn (1978), SZ, came out. In this paper, they analyzed low-resolution spectra of 177 red giant stars located in 19 globular clusters in the halo of the Milky Way. They used an interstellar-reddening independent method of determining the metallicity of the giants and thus the globular clusters in which they are found. One expectation from an ELS galactic formation scenario is that there should be a metallicity gradient as a function of galactocentric radius, R_{GC}, with metal-rich globulars having small R_{GC} and metal-poor ones having large R_{GC}. When SZ combined their work with results from the literature they realized that their were in fact two distinct populations of globulars. They define the inner halo clusters to be at a $R_{GC} < 8$ kpc and outer halo clusters to be $R_{GC} > 8$ kpc. The inner halo globulars do appear to have a metallicity gradient, but the outer halo ones do not. This suggests that the outer halo clusters were not formed from a quickly, 10^8 years, contracting gas cloud, rather they were formed in some other fashion.

They also found another difference in the two groups of clusters, the morphology of the horizontal branches of these clusters was different (for a description of the horizontal branch see Section 3.1). It has been known for some time that the shape of the horizontal branch is a function of metallicity and some unknown second parameter (van den Bergh, 1967; Sandage & Wildey, 1967). For more information on the second parameter problem see Section 3.5). SZ found that the correlation between metallicity and horizontal branch morphology had very low dispersion for the inner halo, but the outer halo showed a large spread in morphologies at a given metallicity. They postulate that the second parameter may in fact be age, and that the outer halo globulars may have formed well after the initial contraction of the galaxy.

One final argument in SZ, suggests that the observed chemical abundance, metallicity, distribution can not be explained by a homogeneous collapse of a single cloud. Rather an accretion of smaller clouds could free-fall into the larger cloud. This, combined with their two previous observations, led them to a theory of the formation of the halo by accretion of smaller clouds onto the already collapsed inner region. The stars and clusters formed in these accreted clouds would then dynamically mix with the Galaxy and form the constituents of the outer halo. Another result of this model is that there could be a much larger spread in stellar ages than in the homogeneous collapse scenario. This scenario continued to be explored in a series of papers by Zinn and collaborators, most notably Zinn (1980, 1986).

2.2.3 From the Ground up Hierarchical Halo Formation

Both the ELS model and SZ model dominated the theoretical landscape for quite some time, but each had its own failings, which became more apparent as larger samples of stars with good kinematics became available (Chiba & Yoshii, 1998; Chiba & Beers, 2000). In particular the relationship between eccentricity of stellar orbits and [Fe/H], which had been one of the major motivators of ELS, was found to be non-existent in larger samples and may have been an effect of their the proper-motion selected sample (Chiba & Beers, 2000). Also the metallicity gradient as a function of galactic radius predicted by the ELS model, did not materialize. As for SZ, the existence of a relationship between rotation velocity and distance above the plane, and observations that their appeared to be two distinct halos, seemed to be at odds with their idea of chaotically merging sub-galactic fragments. Also there are issues with forming a quickly rotating disk in the SZ scenario (Freeman, 1996).

While better observations were challenging these canonical models, there were major changes occurring in cosmology. In the 1990's a new paradigm for the formation of the universe was taking hold. The new model called lambda-cold-dark-matter,ΛCDM, which favored a formation of galaxies through hierarchical assembly, described a universe in which small dark matter halos formed in filaments called the cosmic web, originating from smaller perturbations in the original distribution of matter in the universe. In this scenario, since dark matter can only interact through gravity, larger halos of dark matter were built up slowly from accreting smaller halos, thus leading to the idea of galaxies being built from the bottom up (White & Rees, 1978; Peacock, 1999)

Building on the large kinematic studies of Chiba & Yoshii (1998) and Chiba & Beers (2000), a new theoretical framework was proposed by Bekki & Chiba (2001). They used a dark matter simulation consistent with ΛCDM and allowed it to evolve from a redshift of 25 to the present. Into this model, baryonic gas was added along with a prescription for changing that gas into stars, and for increasing the metallicity of the gas as a function of star formation. By using the complete kinematic and metallicity information from their model, they were able to track the formation of the three primary parts of the galaxy: the bulge, the disk and the halo. In Bekki & Chiba (2001), the stars initially form in small clumps and some of these clumps slowly meld together to form larger clumps. Ultimately they had two relatively large sub-galactic fragments surrounded by some smaller clumps. The smaller clumps are disrupted by the larger fragments and spread their stars into what will become the outer halo. The two sub-galactic fragments then merge which produces an inner halo. During this merger there is also a massive in-fall of gas into the center creating a starburst that eventually becomes the bulge. After the merger, more small clumps accrete onto the inner halo, dumping their gas into a disk producing a primordial thin-disk where more star formation occurs. The production of this disk has the side effect of taking the initially spherical inner halo and flattening it. At a later point, one or more relatively large clumps collide with the disk puffing it up into a thick disk. The rest of the gas falls back into the plane creating a new thin disk, and the galaxy as we know it has formed.

2.2.4 Stellar Streams

The galactic formation model described by Bekki & Chiba (2001) is very good at explaining the structures that are seen in the galaxy today. However, there is one component that is not accounted for. The simulation created by Bekki & Chiba (2001) is entirely self-contained and, as a result, does not take into account the possibility of accretion of dwarf galaxies, in the present day. It has been known for some time that the Milky Way and the Andromeda galaxy are surrounded by, though not necessarily always gravitationally bound to, a large number of dwarf galaxies, the whole amalgamation being referred to as the local group. It is clear that over time, the smaller dwarf galaxies should be consumed by the much larger spirals as they gravitationally interact (Bullock & Johnston, 2005).

The first indication that this actually did occur was found by Ibata et al. (1994) when they discovered the Sagittarius stream. This stream of stars with similar kinematics was then fully described by Majewski et al. (2003). In the years since, many more streams have been found (Newberg et al., 2002; Belokurov et al., 2006). Even more recently, work with the Sloan Digital Sky Survey, SDSS, has discovered several more dwarf galaxies within the halo of the Milky Way (Belokurov et al., 2007).

Although the ΛCDM and the galactic formation models discussed are generally in agreement, the specifics are still in dispute. One major issue is the missing halos problem. Simulations by Klypin et al. (1999) and Moore et al. (1999) suggest that there should be many more dwarf galaxies than have been found. A number of attempts have been made to figure out these difficulties (Bullock & Johnston, 2005), but there are still issues to resolve.

2.3 THE DUAL HALO AND BEYOND

The concept of the halo being composed from two distinct parts, an inner and an outer, has been around since SZ. Zinn (1993) did a good job of summarizing the situation up to that point, focusing primarily on the properties of globular cluster systems. One of the most recent works on this subject was done by Carollo et al. (2007). In their work they used over 20,000 stars with spectroscopy out of the SDSS survey (see Section 4.1). They found strong evidence for the existence of two chemically and kinematically distinct halos, the properties of which are shown in Table 2.1.

Table 2.1: Properties of the Inner and Outer Halos

Property	Inner	Outer
Location	Distance < 10-15 kpc	Distance > 15-20 kpc
Rotational Velocity	0 to 50 km/s	-40 to -70 km/s
Peak metallicity	-1.6	-2.2
Axial Ratio	~ 0.6	$\sim 0.9 - 1.0$

These two halos have very different histories and the formation scenario is similar to Bekki & Chiba (2001). In this case, the inner halo is comprised from the dissipative accretion of sub-galactic fragments. Since these fragments still have interstellar gas in them, star formation continues and the mean metallicity increases. Ultimately the disk forms, which leads to an overall flattening of the halo. Later dwarf galaxies are accreted onto the galaxy and form the outer halo. Since the dwarf galaxies have already made all of their stars, the merger is dissipationless. Also, there is less star formation and thus less metal enrichment in the dwarf galaxies compared to the Galaxy so their overall metallicity is lower. Finally, the retrograde motion may be a result of the stronger dynamical friction for stars on prograde as versus retrograde orbits (Quinn & Goodman, 1986).

The finding of a statistically significant retrograde orbit was one of the primary results of the Carollo et al. (2007) study. To put this into context, their Table 1 summarizes the previous work done on determining the retrograde motion of the outer halo. The final result being, that although previous studies provided hints of an outer halo, Carollo et al. (2007) were able to provide the reliable numbers found in Table 2.1

Chapter 3: RR Lyrae Stars

RR Lyrae (RRL) stars are intrinsically pulsating variable stars, stars that change in brightness over short timescales, that have a long history in the study of astronomy dating back to the end of the nineteenth century. These stars were eventually realized to be of extraordinary usefulness in a variety of astronomical and astrophysical pursuits. These stars have proven immensely useful in the understanding of distances in the Milky Way and beyond. Easily identifiable by their unique lightcurve shape, RRL stars are excellent standard candles because of their relatively uniform absolute magnitude. Also, their relatively high intrinsic brightnesses makes them visible out to the edges of the Local Group. The pulsational properties of RRL have also been used to test aspects of stellar evolution theory. In particular, the masses of RRL stars that pulsate simultaneously in two distinct modes can be determined from pulsation theory and compared with the expectations of stellar evolution models.

In the following sections, the underlying nature of RRL stars will be discussed as well as the basic techniques used to analyze these stars. Furthermore, the source of their variability and their use as kinematic tracers will be discussed.

3.1 Basic Properties

RRL stars are core-helium burning stars that are radially pulsating due to opacity-driven mechanisms (see section 3.4). They are older (population II) low mass stars which have a range of metallicity, $0.0 > [\mathrm{Fe/H}] > -2.5$. This should not be surprising since they were originally found in globular clusters, although they have been found in more metal-rich places like the thick disk. Regardless, they are generally considered representative of Baade's population II stars. RRL stars are periodic variables with periods between 0.2 and 1.2 days and amplitudes in the V magnitude between 0.2 and 2.0 mags (Kholopov et al., 1998). The properties of RRL are summed up in Table 3.1. RRL are giant stars that lie on the horizontal branch (HB) in a Hertzsprung-Russell (HR) diagram. An HR diagram originally plotted the absolute magnitude, M_V, versus spectral type, but it has evolved over the years to include other quantities. For instance, a more theoretical HR diagram can be used to deduce the evolutionary state of a star by plotting luminosity versus photospheric surface temperature. In another variant called the color-magnitude diagram (CMD), the theoretical quantities are replaced by observable substitutes of a magnitude in some photometric pass-band, V for instance, for the luminosity and the subtraction of two pass-bands to yield a color, for example B-V, as a proxy for the temperature. A schematic example of this can be seen in Figure 3.1. The horizontal branch is so named because it is a relatively narrow band that lies roughly horizontal in the HR diagram, which is one of the first indications that RRL stars can be used as standard candles.

Table 3.1: Properties of RR Lyrae Stars (Smith, 1995)

Property	Value
[Fe/H]	0.0 to -2.5
$\log g$	2.5 to 3.0
M_V	+0.6 $\pm$ 0.2 mag
T_{eff}	7400 K to 6100 K
Amplitude	0.2 to 2.0 mag in V
Mass	$\approx$ 0.7 $M_\odot$
Period	0.2 to 1.2 days
Radius	4 to 6 $R_\odot$

Table 3.1: Properties of RR Lyrae stars. (continued)

Property	Value
Spectral Type	A through F

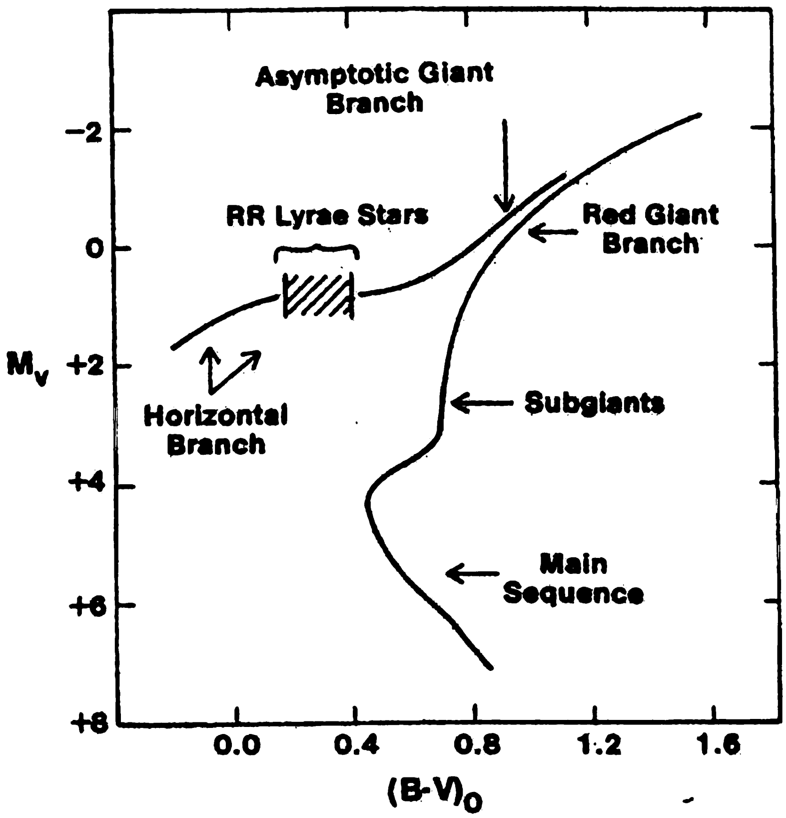

Figure 3.1 A schematic HR diagram showing the position of RRL stars in the instability strip. Figure from Smith (1995).

RRL stars appear at the cross-section of the horizontal branch and another distinct region in the HR diagram called the instability strip. This nearly vertical strip represents those areas in the HR diagram where stars become unstable to pulsation. As a result, it is home to many classical variable star types including Cepheids and main-sequence pulsators such as δ Scuti and SX Phe stars. A more in depth discussion of the instability strip is in section 3.4.

Although there is some dispute about who originally discovered RRL stars, one astronomer who is particularly associated with them is Solon I. Bailey. In 1893, he began a photographic study of globular clusters at the Harvard College Observatory in Arequipa, Peru (Smith, 1995). Through this project he came to discover many hundreds of RRL stars, and in his 1902 paper on the variable stars in Omega Centauri he describes the major breakdown of RRL into three discrete groups based on lightcurve shape: RRa, RRb and RRc, now referred to as the Bailey types (Bailey & Pickering, 1902). These are shown in Figure 3.2. It was later realized that the RRa and RRb stars were in fact the same class of stars and they became known as RRab. RRab stars pulsate in the fundamental radial mode, and tend to have a saw-tooth like lightcurve shape. They also have larger amplitudes and periods on average compared to the RRc stars. As seen in Figure 3.2, the RRc stars have a much more sinusoidal shape and have a smaller amplitude on average than the RRab. The RRc stars pulsate in the first overtone radial mode and thus in more recent works RRab are sometimes called RR(0) and RRc, RR(1). The *General Catalogue of Variable Stars* defines RRab stars as having periods from 0.3 to 1.2 days and amplitudes from 0.5 to 2 magniutes in the V filter. For RRc stars, the periods range from 0.2 to 0.5 days with amplitudes no greater than 0.8 magnitudes in V (Kholopov et al., 1998).

RRL stars are intrinsically variable, so they physically grow larger and smaller as they go through there pulsation cycle. This has a number of effects on the measurements of the star. In the 1980's several attempts were undertaken to get a more complete picture of RRL stars. These programs were interested in using the Baade-Wesselink method of determining stellar radii. As part of these programs, multicolor photometry and high resolution spectroscopy were taken to determine magnitudes, temperatures, and radial velocities. An example of this is work on the RRL star RS

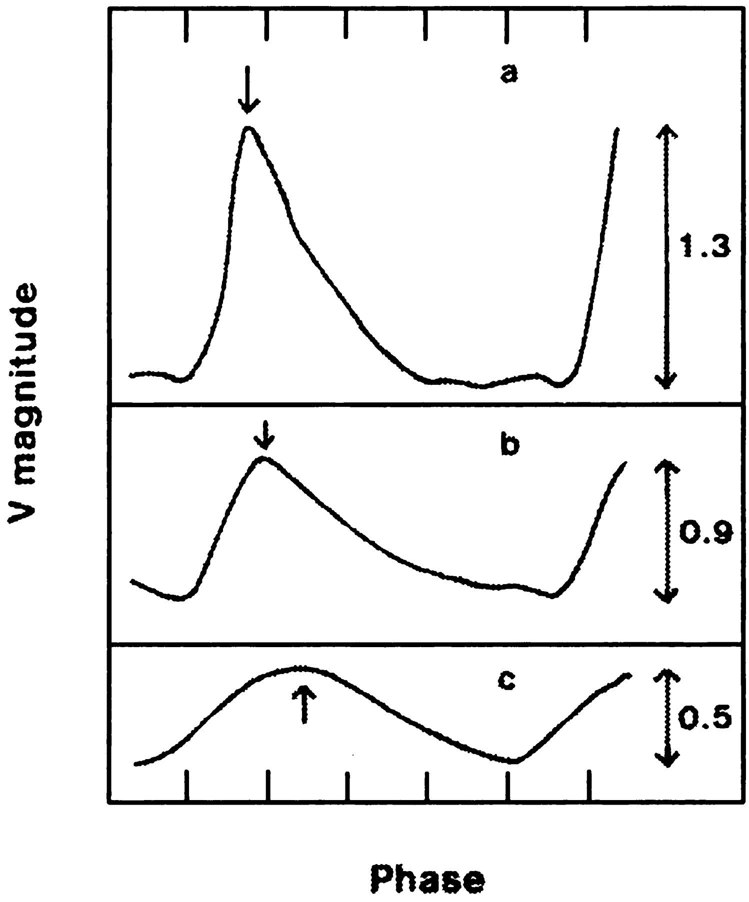

Figure 3.2 This figure shows the three Bailey types of RRL stars originally described in Bailey & Pickering (1902). Figure from Smith (1995).

Boo by Jones et al. (1988). The photometry in the B,V, and K filters can be seen in Figure 3.3. The lightcurves move from the blue to the red part of the spectrum as one goes from B to K (for more information about the B and V filters look in section 4.1). The K filter is a broad band filter that is centered on 22,152 Å out in the infrared. Clearly the amplitude of the lightcurve changes significantly as one proceeds to the red part of the spectrum, and perhaps more importantly the shape of the lightcurve is different in each filter. This means that RRL stars go through a significant color change as they go through their pulsation cycle. As expected, this is mirrored in their spectral type determined by hydrogen absorption lines where an RRab can go from

A7 or A8 at maximum to F5 or F6 at minimum light. RRc stars are a little bluer and have a smaller amplitude in general going from A7 or A8 at maximum to F1 or F2 at minimum (Smith, 1995).

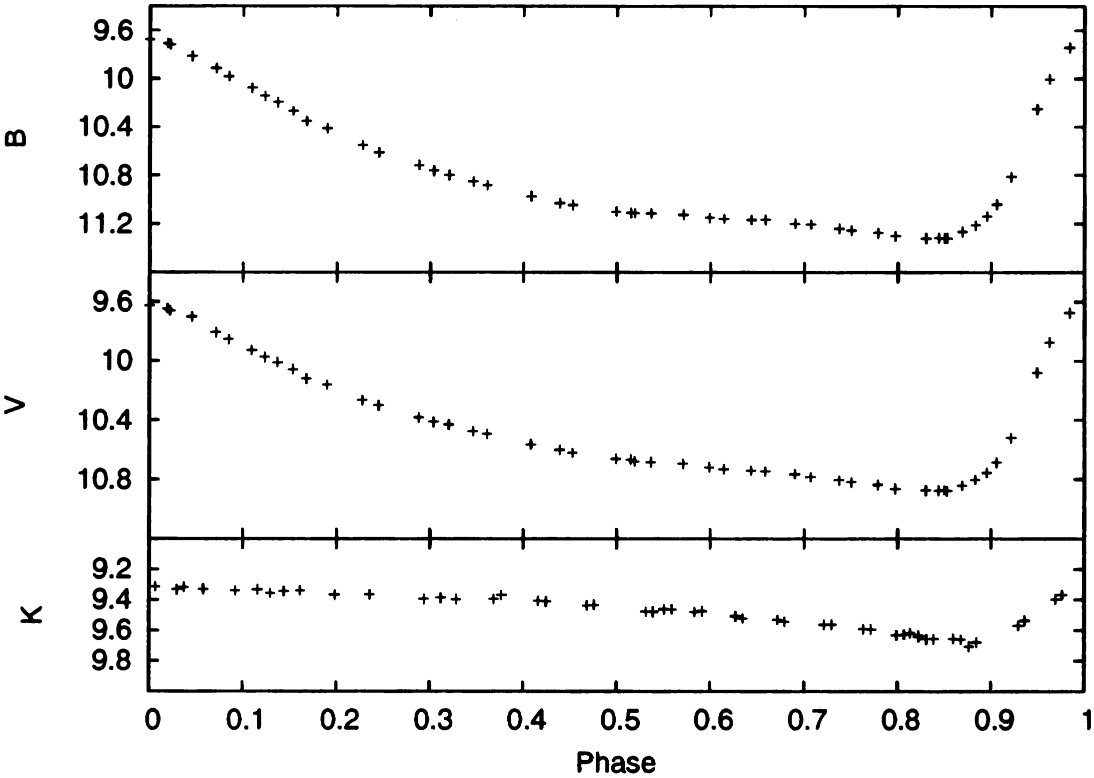

Figure 3.3 Photometry of the RRL star RS Boo in the B,V, and K filters. This figure is based on data from Jones et al. (1988).

Since RRL stars are physically pulsating it is also possible to measure their Doppler shift by taking spectra. The resultant radial velocity curve is largely the inverse of the photometric lightcurve. For example, the radial velocity lightcurve of RS Boo is shown in Figure 3.4. The phase in this figure is the same as in Figure 3.3. The radial velocity curve reaches its minimum at the maximum of the photometric lightcurve, which means that the star is already shrinking by the time maximum light is reached. Ultimately the pulsation in the star represents a change in radius of roughly 15% when compared to the median radius for the star. This intrinsic radial velocity change will become important when using RRL as kinematic tracers, and must be corrected for .

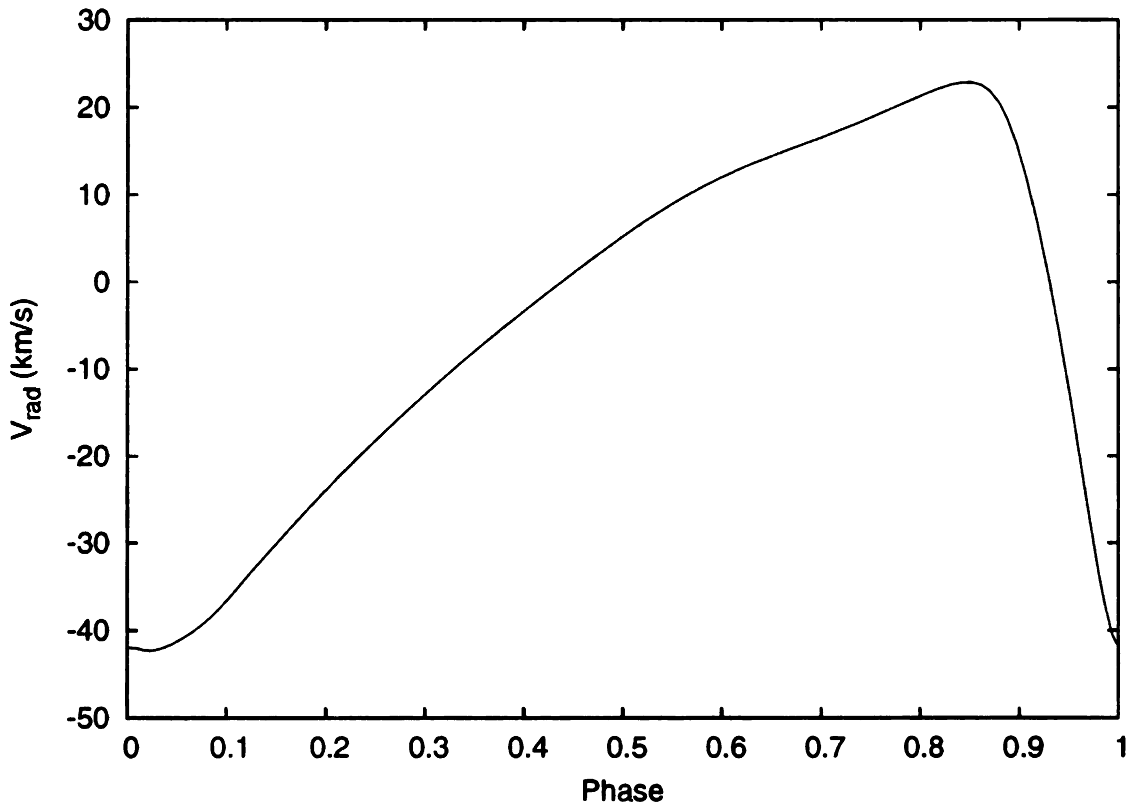

Figure 3.4 Radial velocity curve for RS Boo phased in the same way as Figure 3.3. This figure is based on data from Jones et al. (1988).

3.2 Methods of Analysis

The fact that RRL stars are variable is both what makes them uniquely powerful tools and also makes them much harder to study than the more static objects, which make up much of the rest of astronomy. Working with objects in the time-domain presents several interesting challenges. The first is defining a consistent way of treating time. At first pass it would seem that using days, months, and years would be an adequate way of dealing with time, but there are some significant difficulties including the fact that months do not have the same number of days and that leap years exist. Dealing with these peculiarities can be cumbersome especially when dealing with data over the course of many years. To deal with this, the idea of a Julian Date (JD) was devised. The Julian date tells you how many days, including fractions of a day, have passed since noon Monday, January 1, 4713 BC. There are a number of standards for measuring the time of day, which can be used to make Julian dates. Two of them that are used in this project are the International Atomic Time (TAI) and the Coordinate Universal Time (UTC), which is the solar mean time in Greenwich, England. These two times differ by roughly 30 seconds, and as such are used interchangeably to make Julian dates as is convenient in this analysis.

There is a more subtle issue when trying to measure the exact time of an observation, which plays an important part in making observations of short period variable stars. This issue arises from the finite speed of light. When we measure the time that an observation took place we implicity assume that the time we measure on Earth is directly related to the time at the object we are studying. This is not true because as the Earth moves around the Sun, there is up to a 16 minute travel time difference depending on where the Earth is in its orbit. Since 16 minutes is a significant fraction of certainly the lower period RRL, this must be corrected for. The corrected observation time is called the Heliocentric Julian Date (HJD). The HJD is the date and time of the observation if it had been taken at the Sun, instead of on Earth. This time correction needed to go from the JD to HJD is called the heliocentric correction.

When observing a variable star, the intention is to get a complete lightcurve for it. A problem is that the periods of many RRL are long enough that a single night is not long enough to measure a whole lightcurve. Beyond that, in a practical sense, one would want to combine data from multiple nights, and so there is a method called phasing that puts all of the observations onto one period. Lightcurves for periodic variables like RRL are plotted from 0 to 1 in phase where this represents one complete cycle of pulsation. This is shown in Figure 3.5. Phase, like any cyclic function, can be shifted by a constant and still be correct, so often the HJD of maximum brightness, epoch of maximum, is used as the zero-point for the phase. In order to phase the observations, it is necessary to have an accurate period for the variable.

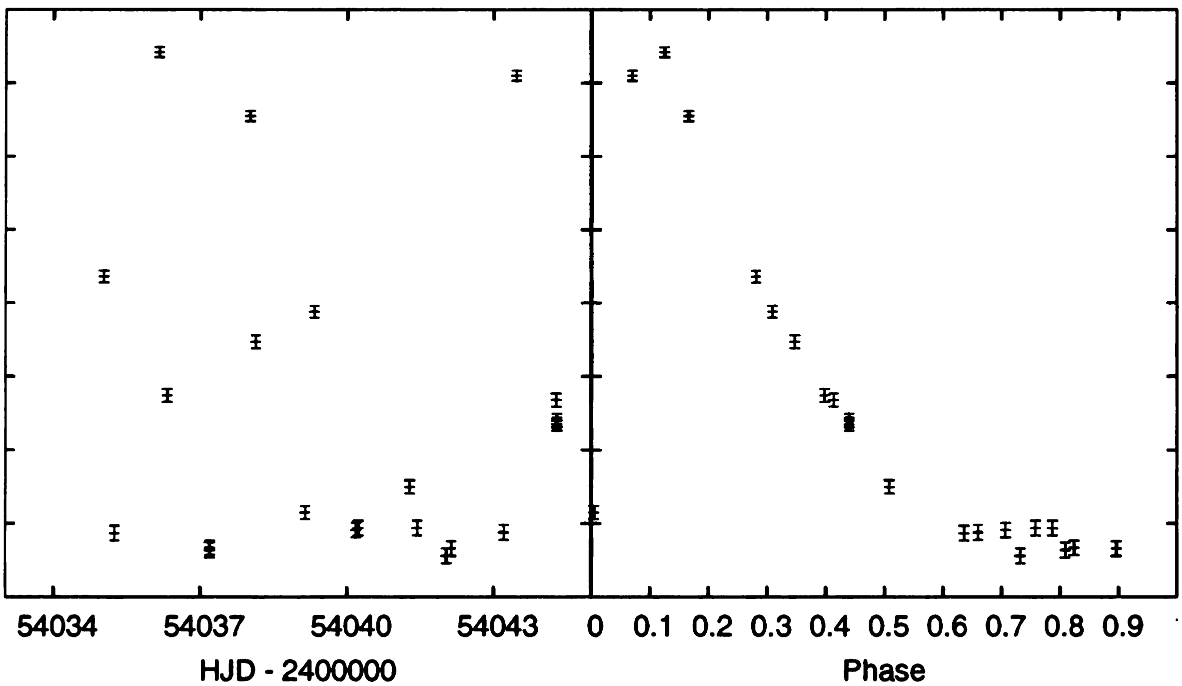

Figure 3.5 These two plots shows an example variable star. On the left is a plot of magnitude as a function of HJD. These same points are then phased using a period of 0.6114 days producing the phase diagram on the right.

3.3 Methods for Period Determination

In general, determining the period of a periodic variable star is relatively difficult, and so there have been an number of methods created to handle this, four of the most prevalent will be discussed here. The Lomb-Scargle periodogram (Lomb, 1976; Scargle, 1982) is one of the original ways of determining periods, P ($P = 2\pi f$ where f is the frequency). It is based on the "classic" periodogram which uses a discrete

Fourier transform to determine the most likely frequencies which can then be turned into periods. Scargle (1982) advanced upon this by developing a new statistic that was equivalent to a least-squares fit of a sine wave to the data. This was further advanced by Press & Rybicki (1989) who developed a method of rapidly calculating the Lomb-Scargle periodogram using Fast Fourier Transforms, FFT. The downsides to this method are that it does not use photometric errors to calculate the periodogram and thus requires a relatively uniform set of data, and that its frequency estimation is highly dependent on how well a cosine describes the shape of the lightcurve (Reimann, 1994).

Another prevalent method is the Phase Dispersion Minimization (PDM) method described in Stellingwerf (1978). This method carves up a phase interval into a series of bins. It then calculates a Θ statistic to describe the amount of scatter in the points. The bin with the lowest scatter, which is the one with the lowest Θ, should be the one with the correct period. The PDM method is quite commonly used because it is distributed with the popular astronomy software IRAF. The drawback to PDM, from the point of view of a survey, is that it is very user intensive.

A more recent method uses cubic splines to determine the period. The method as discussed in Akerlof et al. (1994), uses a series of knots spaced over the phased lightcurve and then calculates cubic splines in between the knots. The χ^2 is then taken between the spline and the data. The period that gives the best fitting between the splines and the data is the period of the lightcurve. The choice of knots is very important because too few results in a poor fit to the shape of the lightcurve and too many can over constrain the fit. In the cubic spline method, the knots are equally space along the phase interval, which can lead to numerical issues with unequally spaced data (Reimann, 1994).

The final method is the one used in this survey, called Supersmoother (Reimann, 1994). It is part of the smoother class of period finding methods, which includes methods like running means or running linear regressions. Supersmoother uses a variable-span linear smoother that calculates a short, medium, and long smooth and then uses the best fit to the data. The period is determined by whichever frequency gives the best sum of absolute residuals. Supersmoother has the benefit of being entirely automatic, and does not make assumptions about the shape of the lightcurve. The use of variable spans, allows it to perform well even with unevenly sampled data. For a more detailed discussion of the Supersmoother algorithm see Reimann (1994).

3.4 PULSATION THEORY

Understanding the radial pulsation of RRL stars, and other intrinsically variable stars, got one of its first major pushes by August Ritter in 1873 (Smith, 1995). He put forward an equation that relates period to the density of the star.

$$P\sqrt{\rho/\rho_\odot} = Q$$

Where P is the period of the variable in days, ρ is the density of the star and $\rho_\odot$ is the density of the Sun. Q is a constant, which is usually around 0.04 for RRab stars. Although, there was discussion over the years as to the exact nature of RRL stars, the next major discussion of possible pulsation mechanisms was in *The Internal Constitution of the Stars* by Eddington (1926). Using polytropic models of stellar structure Eddington showed that without a driving mechanism the decay time of an oscillation would be on the order of 8000 years, suggesting that it would be nearly impossible to see a star in this state (King & Cox, 1968). He went on to suggest a thermodynamic model by which the pulsation could be driven. This is now referred to as an Eddington "valve". He envisioned the valve as either being something that put heat into the star when it was at full compression and diminished at full expansion, or the opposite, a heat leak which is at a minimum during compression and maximum during expansion. He suggested that the opacity of the star could change and act as the source of this leak with the highest opacity occurring at maximum compression (Smith, 1995).

Eddington initially put the valve at the center of the star suggesting that it was based on the fusion rate in the core. It is now known that the actual location of the valve is in the outer envelope of the RRL star, in a region where helium is doubly ionized as was suggested by Zhevakin (1953) and independently by Cox & Whitney (1958). The valve is related to the Rosseland mean opacity, κ, which is defined as:

$$\kappa = \kappa_0 \rho^n T^{-s}$$

where ρ is the density and T is the temperature. In regions of stars without a dominant element being ionized, the values of $n \approx 1$ and $s \approx 3.5$. This clearly does not work as a valve because the point of maximum compression is also a maximum in temperature, and thus the opacity would be low. In the case of a region with partial-ionization of a dominant element, however, the s drops to 0 or even slightly negative. This means that opacity is primarily a function of density providing exactly what we need for an Eddington valve, a maximum in opacity near maximum compression. This is referred to as the κ-mechanism (King & Cox, 1968).

Although the κ-mechanism is dominant in RRL, there is another significant driver of pulsation. This mechanism is based on the way heat behaves in a medium with a dominant element partially ionized. Heat added to this layer goes into ionizing more of the element rather than changing the temperature, meaning that the partially-ionized region remains cooler than neighboring regions. During compression, this results in more energy being dumped into the partially-ionized region as heat flows from hot to cool, resulting in another driving mechanism for pulsation. This is generally referred to as the γ-mechanism (King & Cox, 1968).

Using this knowledge about the pulsation mechanisms in RRL we can then ask the question: Why does the instability strip exist in the HR diagram, and what are the red and blue edges of this strip? The answer lies in the properties of the partial-ionization zone. In particular, it is the location of this zone which has the most effect on whether a star begins to pulsate (Smith, 1995). If the temperature of the star is too high, then the partial-ionization zone gets driven to the surface of the star, and eventually there is not enough material to drive pulsation. This defines the blue edge of the instability strip. The red edge is somewhat less well understood, but the current best scenario is based on energy transport within the star. In hotter giant stars, like RRL, the cores of the star move energy via convection, and as one progresses out toward the surface the dominant mechanism becomes radiative transport. Since opacity only affects radiative transport, the idea is that the red edge of the instability strip occurs when the star becomes cool enough for convective transport to become significant in the envelope of the star where the partial-ionization zone is located. This means that a significant amount of energy can be transported by convection, which effectively disrupts the Eddington valve.

3.5 Oosterhoff Dichotomy

As work continued in the early part of the twentieth century, it was soon noticed that RRL stars in different globular clusters had different mean properties for the periods and for the ratio of RRab to RRc type variables. This was in particular noticed by P. Th. Oosterhoff (1939) as he studied a handful of globular clusters. He found that there appeared to be two distinct groups. The first group, later called Oosterhoff type I (OoI) had shorter average periods for the RRab stars, and much lower fraction of RRc stars. The second group Oosterhoff type II (OoII), had a higher average period for RRab stars and roughly double the fraction of RRc stars. A prototypical globular cluster for OoI is M3 and for OoII is M15. It was later realized that the Oosterhoff dichotomy was also a dichotomy in metallicity with the OoI clusters being more metal-rich than the OoII clusters. Table 3.2 shows the basic parameters of the two Oosterhoff types (Smith, 1995).

Table 3.2: Properties of the Oosterhoff Groups

Group	$< P_{ab} >$	$< P_c >$	n_{RRc}/n_{RRL}	[Fe/H]	Example GC
OoI	0.55	0.32	0.17	> -1.7	M3
OoII	0.64	0.37	0.44	< -1.7	M15

When the globular clusters in the Milky way are plotted up on an average RRab period versus metallicity plot, it becomes clear that there is a zone of avoidance in both period and metallicity as shown in Figure 3.6a. This clustering of the globular clusters in this diagram suggests that they were perhaps formed in different settings and could give clues to the formation of the halo (Lee & Carney, 1999).

The existence of the Oosterhoff dichotomy is not well understood, and to add to this issue it appears that may be particular to the Milky Way itself. A number of globular clusters in the Local Group have been studied and they do not appear to show the same Oosterhoff dichotomy that the Milky Way ones did. Moreover, looking at Figure 3.6b it becomes abundantly clear that the clusters in the dwarf galaxies of the local group in fact prefer to fill the Oosterhoff gap. This has implications for the formation of the Milky Way halo, and is subject that is currently being explored.

There have been a number of theories as to the origin of the Oosterhoff dichotomy. Some of these include the existence of a hysteresis zone in the instability strip that keeps blueward evolving RRab stars and redward evolving RRc stars from changing their pulsation mode (van Albada & Baker, 1973). This would suggest that OoI clusters are evolving red to blue and OoII clusters the other way, but there has not been sufficient evidence to support this. Another possibility is that the brightnesses

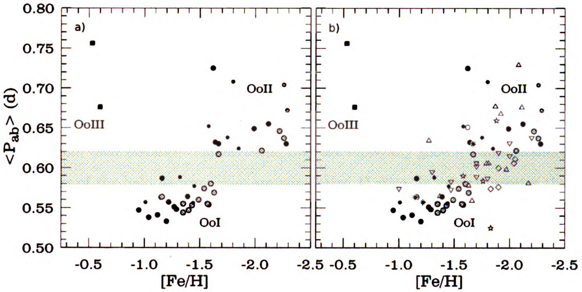

Figure 3.6 Globular clusters from the Milky Way (circles and squares) plotted with globulars from the Local Group (all other symbols). Figure a) includes only the globular clusters from the Milky Way. Figure b) adds in the clusters from the Local Group including Fornax, Sagitarius, and the Canis Majoris dwarf spheroidal galaxies. There are also some clusters from the LMC. The clusters from the Local Group appear to favor the traditional gap seen in the Milky Way. The period gap is shown as a bar. Figure from Catelan (2005).

of the horizontal branches of globular clusters in each group are different. Sandage has a number of papers dealing with the way in which period and intrinsic luminosity are a function of metallicity. In two of his more recent papers (Sandage, 1993a,b) he goes into more detail and takes into account some of the criticism of this method.

Ultimately, this leads into the large question of horizontal branch morphology and the question of the second parameter problem. It is well known that metal-poor clusters have longer bluer HBs and metal-rich ones have more of a red clump. There does appear to be some other factor, the second parameter, that affects HB morphology. One possibility could be helium enrichment through a variety of mechanisms (Sweigart & Catelan, 1998). This issue percolates into our understanding of recently discovered Oosterhoff III clusters, which are very metal-rich bulge globular clusters, that do not follow the period-metallicity trends of the other two groups Pritzl et al.

(2001).

3.6 Usefulness as Kinematic Tracers of the Halo

RRL stars are very good standard candles, which means that they provide a rare bit of information, their distance. Furthermore, they are especially good for understanding the nature of the halo because they are population II stars, in general greater than 10 Gyrs in age, so they trace the old populations of the Galaxy. This fact has been recognized for some time, and the primary limitation in using them is that they are relatively rare stars, which are hard to identify without multi-epoch observations. As a result, other HB stars were used instead. These stars should be standard candles as well, although they occupy a larger color range, so there is a relationship between color and M_V. There are also some contamination issues with main-sequence (MS) stars. An example where both Blue Horizontal Branch (BHB) stars and RRL were used was in Preston et al. (1991). In this paper, they showed a decrease in stellar age as a function of increasing galactic radius. They also used BHB stars and RRL to investigate the shape of the halo.

Layden (1995a,b) undertook a very comprehensive study of the galactic structure using RRL. He used a sample of 302 RRab with good photometry, radial velocity measurements, and metallicity determinations (Layden, 1994) to work out rotational velocities for both disk and halo components of the Milky Way. Combining this information with proper motions from the literature he was able to get full space motions, which allowed him to compare his results with a number of previous studies including Morrison et al. (1990); Beers & Sommer-Larsen (1995). Layden did not see a retrograde motion for the halo, but rather a slight prograde one, $V_\phi = 18 \pm 13$. His sample, however, was highly limited in spacial extent, with the outer-most RRL being only 4 kpc from the Sun.

Another approach was used by Lee & Carney (1999) to look at the kinematics of the halo using RRL in globular clusters. They subscribed to the hysteresis explanation of the Oosterhoff groups discussed in section 3.5, with metallicity being the primary parameter that determines which direction the stars in a cluster will evolve. Furthermore, they suggested that the Oosterhoff groups actually represent different formation epochs. In this case the metal-poor OoII comes from an ELS like scenario forming in the proto-galaxy, whereas the metal-rich OoI clusters come from an epoch of accretion like SZ. They found a possible retrograde motion for the OoI clusters, $< V_{rot} = -68 \pm 56$km/s, and a prograde motion for the OoII clusters, $< V_{rot} >= +94 \pm 47$ km/s. They saw the signature of accretion in the OoI globular clusters with a slight retrograde motion. The OoII globular clusters had a slight prograde motion. This study had the benefit of sampling at a wide range different galactocentric radii, but it was limited to ≈ 40 globular clusters.

Both Layden (1995a) and Lee & Carney (1999) use the same method to determine the bulk rotation of the halo. This method, originally developed by Frenk & White (1980) and summarized by Zinn (1985), determines bulk motions using radial velocities, positions, and distances only. This is extremely useful because proper motions, necessary for full-space motions, are often hard to come by and generally are available only for nearby or fast moving objects. At first look, it appears that there is a discrepancy between these two papers. This may not be the case, however, because Layden (1995a) samples only the local solar neighborhood, which is likely primarily disk and old halo, whereas Lee & Carney (1999) sample well out into the newer outer halo.

A very recent paper by Kinman et al. (2007) presents a more complex view. Kinman's group analyzed 26 RRL stars and 52 BHB stars and found that the two groups may actually trace different components of the halo. They have full proper motion and radial velocity information for these stars and were able to determine full U, V, W space-motions. Furthermore, these stars are located in the SA 57 field, which is located toward the North Galactic Pole (NGP), which should minimize disk contamination. Ultimately, they found the BHB stars had no net rotation whereas, the RRL had a net retrograde rotation. Their sample was limited to within $Z < 8$kpc and apparent V magnitude < 16.

More recently a number of larger RRL surveys have taken place. These surveys, usually the result of looking for other transient objects, have provided significantly more information than has been previously available. The results of these surveys and their individual benefits and pitfalls will be discussed in section 4.4.

CHAPTER 4: THE SLOAN DIGITAL SKY SURVEY AND OTHER SURVEYS

4.1 OVERVIEW

The Sloan Digital Sky Survey, SDSS,(York et al., 2000) is the largest photometric and spectroscopic survey to date. The survey saw first light in May of 1998 and began regular operations April 2000 (Adelman-McCarthy et al., 2008). SDSS was designed initially as a quasar survey; it has far exceeded that original mission with work extending over many different projects relating to both galactic and extra-galactic astronomy. The survey uses a 2.5 meter telescope located at Apache Point, NM. The original survey had two distinct parts, a photometric survey and a spectroscopic survey. The photometric survey used a 120 megapixel camera consisting of 30 2048x2048 CCD imagers spaced in six columns and five rows (Gunn et al., 1998). Due to the extra-galactic focus of the original survey a new photometric system, $u'g'r'i'z'$, was used instead of the more common Johnson-Cousins system. The $u'g'r'i'z'$ system is a broad-band photometric system that covers from 3000 to 10,000Å (Fukugita et al., 1996; Stoughton et al., 2002). The $u'g'r'i'z'$ filter system is compared to the Johnson-Cousins system in Figure 4.1. When discussing the *ugriz* filter system there are two slightly different systems that exist. The un-primed *ugriz* system refers to the filters on the 2.5 meter telescope. The primed system refers to the filters used on any other telescope and are calibrated to the 1.0 meter USNO telescope at the Flagstaff station

(Smith et al., 2002). For the most part these two designations differ by only a small amount and the two can be transformed back and forth with relative ease.

The telescope was used in a drift scan mode, which drifts at the sidereal rate, where the sky is imaged in arcs of great circles where each object is integrated through each of the five filters for 54.1 seconds as shown in Figure 4.2. This results in a 5σ detection limit with 1" seeing of 22.3, 23.3, 23.1, 22.3, and 20.8 magnitudes in the u', g', r', i', and z' filters respectively (York et al., 2000). Each of these scans is referred to as a strip and each strip is observed in pairs with the paired strip being offset from the first by 93% of the CCD width. The combined pair of strips is referred to as a stripe and is 2.54 degrees wide (York et al., 2000).

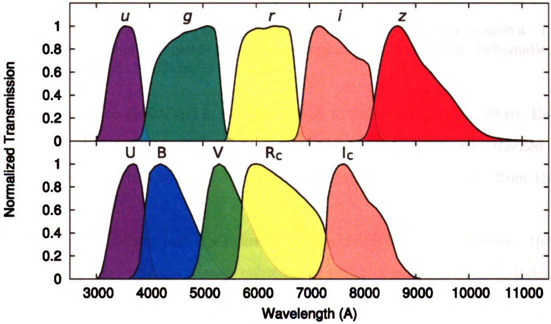

Figure 4.1 Comparison of the SDSS *ugriz* and the Johnson-Cousins UBVRI filters. This figure is adapted from Clem (2005).

The results of the photometric survey are then used to define subsets of objects to be studied in further detail with the spectroscopic survey. The spectroscopic survey uses two fiber-fed spectrographs each with a blue and a red channel. The blue channel

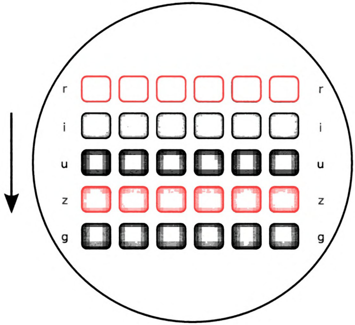

Figure 4.2 A schematic layout of the *ugriz* filters on the SDSS survey camera. The arrows show how the sky passes over the camera in drift scan mode. Schematic is based on description in (Gunn et al., 1998)

runs from 3800Å to 6500Å and in red from 5800Å to 9200Å (York et al., 2000). Each spectrograph has 320 fibers leading to a total of 640 fibers which are attached to pre-drilled plates. The resolution $\delta\lambda/\lambda$ varies as a function of wavelength from 1850 to 2200.

As the SDSS Survey and it's followup survey, SDSS-II, have progressed, there have been a number of data releases culminating with the most recent Data Release 6, DR6, (Adelman-McCarthy et al., 2008). As of DR6, over 9582 sq degrees of the northern sky have been imaged resulting in photometry of 287 million unique objects. The photometry of these objects has been calibrated to 1% accuracy for g,r,i,z and 2% for u. The spectroscopic survey has also produced a massive amount of data, covering 7425 sq. degrees of sky with over 1.27 million spectra including stars, galaxies, quasars and calibration spectra (Adelman-McCarthy et al., 2008).

4.2 SDSS-II SN Survey

After the completion of the original SDSS survey in June 2005, now called SDSS-I, an extension to that survey called SDSS-II was created. SDSS-II consists of three distinct surveys: the SDSS Legacy Survey, SEGUE, and the Sloan Supernova Survey (SN Survey). The SN Survey was designed to study intermediate redshift ($0.5 \leq z \leq 0.35$) type Ia supernovae (Frieman et al., 2008). The SN survey repeatedly images an equatorial stripe using a two day cadence. The imaged region, known as Stripe 82, runs from 20^h to 4^h in right ascension and from 1.25 to -1.25 in declination. This creates a 2.5 degree wide stripe that leads to a total imaged area of 300 sq. degrees (Frieman et al., 2008). For a definition of right ascension and declination, see Section 7.3. This particular stripe was chosen because it is equatorial and thus can be reached by ground-based telescopes in both the northern and southern hemispheres, but also because Stripe 82 has been used as the photometric calibration stripe since the beginning of the SDSS and as such provided them with enough data to co-add the images together to make a very good template image to use in image subtraction (Frieman et al., 2008).

The two day cadence of the observations is due to the nature of the SDSS imaging camera. As seen in Figure 4.2, the CCDs are arranged in six columns with a significant gap in between them. As a result, in order to get a continuous stripe, two interleaving strips, a north and a south one, must be taken. As in the case with the SDSS-I survey, the camera tracks at the sidereal rate, so the individual strips are alternated from night to night leading to the two day cadence. This observation schedule was followed from Sept 1st to Nov 30th for 2005, 2006, and 2007 (Frieman et al., 2008).

Since the SN Survey used the same drift scan rate as the original survey, they have comparable photometric accuracies. However, whereas the SDSS-I survey limited itself only to photometric nights, the SN Survey had a much higher tolerance for poor observing conditions, operating in non-photometric and bright moon time. This was not a major issue for them, because they were interested in differential photometry as versus absolute photometry.

4.3 Variable Star Catalogs

The SN Survey produced large numbers of repeated observations of Stripe 82, however, they used image subtraction techniques to find and quantify their supernovae. This meant that the images taken by the SN Survey were not put through the normal photometric routines that the rest of SDSS imaging had gone through. As a result, it was left to two separate teams, one located at Cambridge and the other at the University of Washington, to create photometric catalogs for all the observed epochs. Each of these lightcurve catalogs will be taken in turn.

4.3.1 Cambridge Catalog

The Light-Motion Curve Catalogue (LMCC) was produced by Bramich et al. (2008) at Cambridge. This catalog took data from the 2005 season of the SN Survey as well as the previous calibration data going back to September of 1998. The catalog has two main purposes; the first is to perform epoch by epoch photometry on all the objects in Stripe 82 complete to a limiting magnitude of $r \sim 21.5$. The second is to make a proper motion catalog for both point and extended sources down to 18th magnitude in r, getting $\sim$ 32 mas and $\sim$ 35 mass RMS accuracy (Bramich et al., 2008). The resulting catalog contains over 4 million objects distributed over a slightly smaller range than the whole of Stripe 82 going from a right ascension of 20.7^h to 3.3^h and a declination of -1.26 to 1.26 degrees as can be seen in Figure 4.3.

The LMCC has a counterpart catalog that contains mean properties such as the proper motions, reddening, and variability indices. This catalog is call the Higher-Level Catalogue (HLC). The HLC consists of a series of binary fits files providing 229 photometric and astrometric parameters (Bramich et al., 2008). Both of these catalogs are publicly available through SDSS-II. The most current version and the one used in this project is version 2.

4.3.2 Washington Catalog

The LMCC and HLC catalogs are very useful for searching for variable objects, but they have one major downside, they only include data from 2005 and before. Increasing the number of epochs in a lightcurve increases the chances of determining the type, period, etc. To this end, another catalog from the University of Washington was used. This catalog, developed by Ivezić et al. (2007) and Sesar et al. (2007), contains data through 2006. It also used a different algorithm for determining the photometric zero points, which helped increase the overall photometric accuracies of the data. This new photometric accuracy had particular effect on the u filter allowing many more u epochs to be included in the lightcurves. Since the LMCC catalog was used for the initial detection of the variable stars, the limits in right ascension and declination are the same.

4.4 Other RRL Surveys

In recent years, there have been a number of large scale variable star surveys, that have either piggy backed on surveys designed for another purpose, QUEST-I and LONEOS, or were companion projects for another program, NSVS. They each have their benefits, either wide sky coverage or deep exposures, and they each have provided a catalog of stars that can be used to explore questions about the structure of the galaxy. As such, they will be discussed during the analysis of this survey's data in Chapter 8.

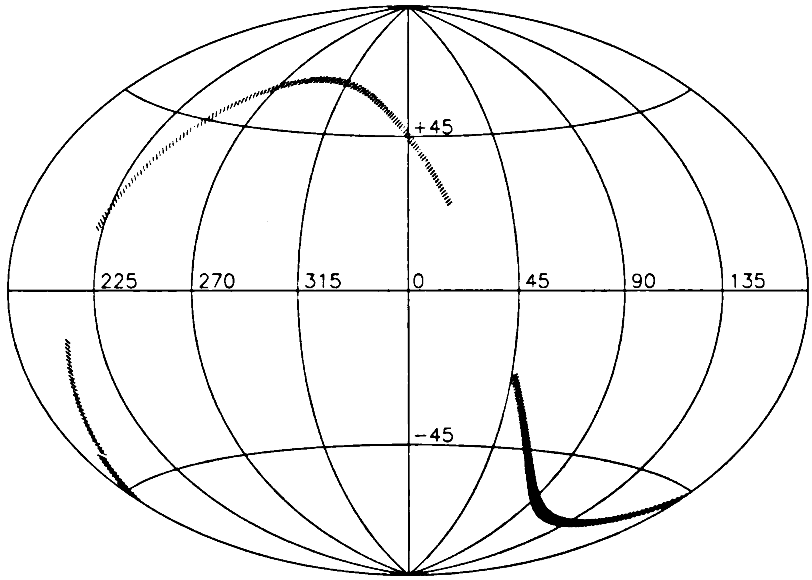

Figure 4.3 The locations in galactic coordinates of the SN Survey, in blue running through negative galactic latitudes, and the QUEST survey, in red primarily running through positive galactic latitudes with an extra section below the galactic equator near galactic longitude of 210.

4.4.1 NSVS

The Northern Sky Variability Survey (NSVS) (Woźniak et al., 2004) was conducted on the Robotic Optical Transient Search Experiment (ROTSE-I) telescope (Akerlof et al., 2000). The survey found 1197 RRab stars down to magnitude of V = 14 Kinemuchi et al. (2006). The survey was conducted on 206 16.4 x 16.4 degree fields, in a nonstandard filter that roughly corresponds to Cousins R. For a map of the fields, consult Akerlof et al. (2000) Figure 1. The project was a companion project to a program designed to do optical follow-ups of Gamma-Ray Bursts. The program benefited from extensive sky coverage, but was limited by their relatively bright cut-off magnitude.

4.4.2 QUEST-I

The Quasar Equatorial Survey Team (QUEST-I) was originally designed for a large scale quasar survey. A number of scientific projects were done on this telescope each with its own filter set, the filter that was common to all of these was V. As a result, the variable star detection and lightcurves are done in the V filter only. The QUEST-I survey is perhaps the most similar to the SN Survey in the sense that it is also a drift-scan equatorial stripe. The position of QUEST-I can be seen in relation to the SDSS Survey in Figure 4.3. The survey produced 498 RRL stars 395 RRab and 103 RRc, down to a limiting magnitude of V = 19.5 (Vivas et al., 2004). The QUEST-I survey provides a strong compliment to the SN Survey in that it clearly covers a region of the galaxy not sampled by the SN Survey to a similar depth.

4.4.3 LONEOS

The Lowell Observatory Near Earth Object Survey (LONEOS) was designed to discover near earth asteroids (Bowell et al., 1995). The LONEOS survey is unfiltered and covers 1430 deg^2 in 5 deg^2 fields. A map of the fields can be found in Figure 1 of Miceli et al. (2008). In their survey they found 838 RRab stars down to R $\sim$ 18.5 (Miceli et al., 2008). The data reduction pipeline for this survey is discussed in Rest (2002)

Chapter 5: Photometric Analysis

5.1 Variable Star Selection

As was mentioned in a previous chapter, the LMCC catalogs, both versions one and two, contain on order four million objects, most of which are stars. Since we are looking for on order a few hundred stars we need several powerful methods to distinguish the variable from the non-variable stars. One of the primary ways in which this is done is to develop a variability index. Variability indices all have the same underlying prinicipal of looking for large deviations from the mean magnitude of the star compared to the photometric error for each point. The Welch-Stetson index is an example of one of these (Stetson, 1996). These sort of indices tend to fail, however, when one approaches the limiting magnitude of a survey. This occurs because often times the stated error in the magnitudes tends to be an underestimate. This leads to false positives which render the index less effective. To compensate for that one can use color cuts. Since RRL stars must exist in the instability strip and are giant stars, one can devise a series of color cuts to separate them out from the rest of the stars. One such attempt was made in Ivezić et al. (2005).

Once the candidate variable stars are found, the next step is to determine which stars are actually RRL and which are not. The first issue is to determine the period of the variable stars. There are a number of programs which can do this, but the one we used is called supersmoother (Reimann, 1994). Supersmoother attempts to determine the period by finding the period that creates the smoothest looking fit to the data.

For RRL stars, this works pretty well, although there are cases where aliases show up, or the smoothest line is not the true period due to errors in the photometry. At this point, the two best periods are looked at and are classified by eye into variable star type, and into ab or c type if they are determined to be RRL stars. To further help with classification, we used Layden's (1998) RRL templates. These templates were fit to each of the 15 best periods found by supersmoother, and the best two fits were then examined. Finally, the results were plotted on a period-amplitude diagram and final classifications were chosen at that point.

5.1.1 Welch-Stetson Index

When searching for variability in a sample of stellar photometry, one is by definition looking for a change in magnitude, which is outside of the specified errors. One can quantify this variability by creating an index that for example becomes larger as more deviations from the mean magnitude are found. One can further increase the robustness of the index by looking at pairs of observations. The idea being that if their is a variation in two separate filters, or paired observations in the same filter, for a given epoch that it is more likely that this is true variation as versus bad photometry, cosmic rays etc. An early example of an index that used this method can be found in Welch & Stetson (1993). In this early index using paired b and v observations (5.1), b_i and v_i are the photometric observations, $\overline{b}$ and $\overline{v}$ are the weighted means in each filter, $\sigma_{b,i}$ and $\sigma_{v,i}$ are the photometric errors, and n is the number of paired b, v observations (Welch & Stetson, 1993; Stetson, 1996).

$$I = \sqrt{\frac{1}{n(n-1)}} \sum_{i=1}^{n} \left(\frac{b_i - \overline{b}}{\sigma_{b,i}} \right) \left(\frac{v_i - \overline{v}}{\sigma_{v,i}} \right) \quad (5.1)$$

This original Welch-Stetson index was improved upon in Stetson (1996) by generalizing this process to any number of observations in any number of filters per epoch.

This new variability index is given in equation (5.2). In this index, the observations taken at a given epoch are grouped into k pairs where each pair is product of the normalized residual of each observation $P_k = \delta_{i(k)}\delta_{j(k)}$. These pairs are then weighted by a value w_k depending on how many distinct frames go into the pair.

$$J = \frac{\sum_{k=1}^{n} w_k \,\mathrm{sgn}(P_k)\sqrt{|P_k|}}{\sum_{k=1}^{n} w_k} \tag{5.2}$$

In the ideal case, one has pair constructed from two observations, and this will have a weight, w_k, of 1. In some instances, there will be no pair for a given frame, so one will have to pair a frame with itself. In that case, one uses a lower weight of 0.5 to account for the loss of information compared to a pair constructed from two frames. In the case of this study, three frames at the same epoch a, b, and c were paired together. This generates three pairs ab, bc, and ac each with a weight of 2/3. When these three pairs are added to the sum, their combined weights $2/3 * 3$ gives a combined weight of 2 thus accounting for the more information provided by using three and making them twice as good as a pair of two frames which is twice as good as a pair of a frame and itself. Pairs are built from normalized residuals:

$$\delta = \sqrt{\frac{n}{n-1}}\frac{v-\overline{v}}{\sigma_v}$$

This formulation is similar to equation (5.1), but has an added statistical factor of $\sqrt{\frac{n}{n-1}}$ to account for the fact that this observation was used in creating the mean. This normalized residual is then used to create a pair. The variability index depends on the fact that for random error the expectation value of $\langle \delta_i \delta_j \rangle$ is zero, and for true variation tends towards a positive number. In the case where one pairs a frame with itself, $i(k) = j(k)$, the expectation value for random error tends to unity for $\langle \delta_i^2 \rangle$. To put both types of pairs on even ground, i.e. going to 0 for non-variable stars the pairs function P_k is defined as:

$$P_k = \begin{cases} \delta_{i(k)}\delta_{i(j)}, & \text{if } i(k) \neq i(j); \\ \delta_{i(k)}^2 - 1, & \text{if } i(k) = i(j). \end{cases}$$

This variability index is useful for detecting a wide variety of variable stars, but it can be made more sensitive to the periodic stars that are the focus of this study. Stetson (1996) developed a kurtosis index shown in equation (5.3). In this equation, N is the total number of observations and δ_i is the normalized residual from before. This index is created such that for Gaussian noise the index tends to 0.798. For a pure sinusoid $K \to 0.900$ and for a sawtooth $K \to 0.866$. In the case of a single bad measurement, $K \to 0$ as $N \to \infty$.

$$K = \frac{1/N \quad \sum_{i=1}^{N} |\delta_i|}{\sqrt{1/N \quad \sum_{i=1}^{N} \delta_i^2}} \tag{5.3}$$

To take advantage of both the J and K indices a final combined L index was created. Stetson's version of it is found in equation (5.4). There is a division by 0.798 in this equation that causes the L index to equal the J index for a Gaussian distribution of magnitudes, but there is a slight enhancement for periodic variables like RRL since they have a more sawtooth or sinusoidal shape. In equation (5.4) $\sum w/w_{all}$ is a weighting factor where w_{all} is the number of possible frames a star could appear in and $\sum w$ is the number of frames the star was actually detected in. Given that the data in this project was taken in stripes in the sky, which were of variable length depending on conditions and time of year, it was not straightforwardly possibly to calculate this weighting factor. As a result $\sum w/w_{all} = 1$ for the Welch-Stetson L index used in this project.

$$L = \left(\frac{JK}{0.798}\right)\left(\frac{\sum w}{w_{all}}\right) \tag{5.4}$$

The LMCC catalog provides u, g, r, i, and z lightcurves for each object in the catalog. The quality of the photometry, however, varies significantly depending on the filter. As a result, only g, r, and i observations were used to create the L index. The pairs varied from three down to one observation per epoch as the photometry allowed, and the weights were assigned as previously discussed.

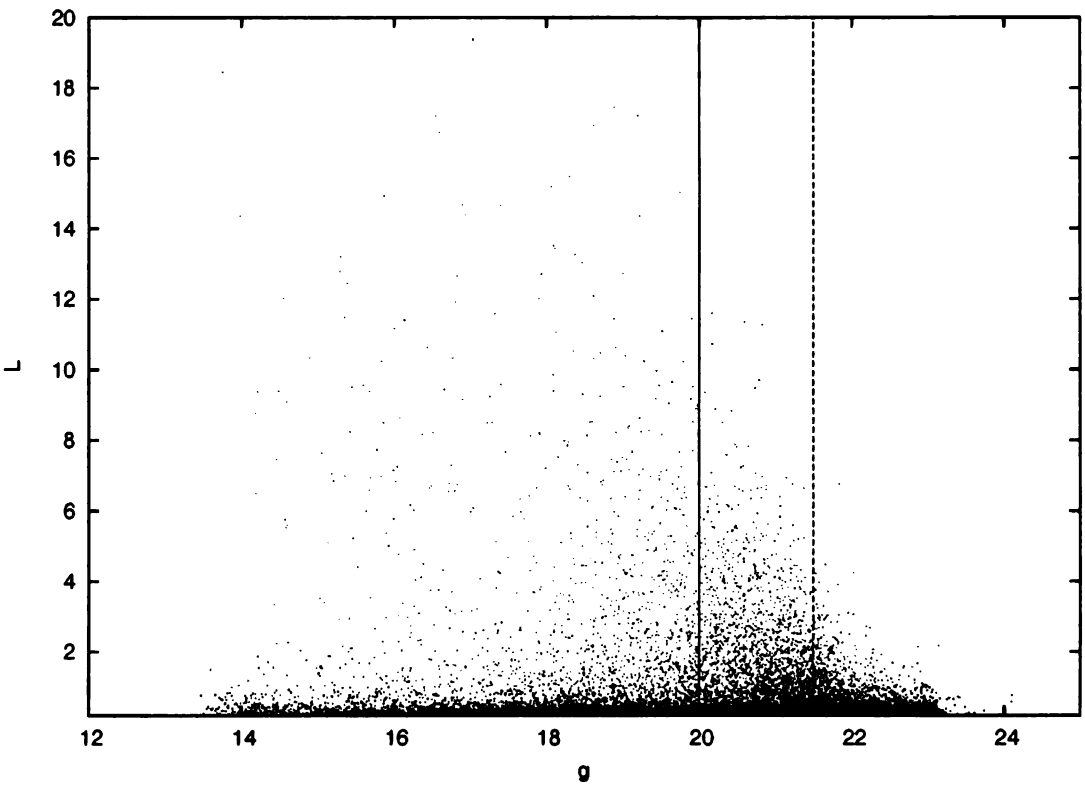

Figure 5.1 This is a 1/10 sample of stars from the LMCC catalog. The solid line is a magnitude cut g of 20.0 and the dotted line is cut at g of 21.5. There is a clear over-density of stars between these cuts.

In figure 5.1 the L variability index has been plotted as a function of g magnitude for stars from the LMCC catalog. It is apparent from this plot that as one goes to dimmer magnitudes, the number of variable candidates increases. This effect is due primarily to the underestimate of photometric errors at high magnitude. As a result, the contamination by non-variable stars of a variable star sample selected using L is magnitude dependant. The number of candidates drops down after g of 21.5 because the database is not complete beyond this magnitude (Bramich et al., 2008).

5.1.2 Finding the Mean

One of the critical steps in creating a robust variability index is developing a mean magnitude to compare individual observations against. The first inclination in a situation like this is to use a weighted mean weighting the observations based on the photometric errors, $1/\sigma^2$. This suffers from the generic problem of means that they are overly influenced by outliers. This is especially true in the case of variable stars, since the photometry by definition is outside of the photometric errors. There are a number of methods that have been developed to deal with this issue including 3σ clipping. Any sort of clipping method is undesirable, because insignificant fluctuations in photometry near the clipping limit can make the difference between a point be included or not. Stetson came up with a solution to this issue by creating a smoothly varying iterative process for finding the mean (Stetson, 1996, 1987). In the first iteration, a weighted mean using photometric errors is used. For all other iterations, a smooth function based on the normalized residuals from section 5.1.1 is used and is shown in equation (5.5). In this case, $a = b = 2$ was used, although the result tends to be insensitive to the choice of values for a and b. The iterations were continued until the mean converged to a tolerance of 0.0001 mags or until 50 iterations were completed.

$$\left[1 + \left(\frac{|\delta|}{a}\right)^b\right]^{-1} \tag{5.5}$$

5.1.3 Color Cuts

The variability index, L, is very effective at picking out the variable stars especially at the brighter end of the magnitude range. In the case of this project, however, we are interested in the RR Lyrae in particular, and not as interested in other variables like eclipsing binaries. Since the instability strip puts relatively narrow constraints on the colors that an RRL star can have, one can exclude many non-rrl stars by making appropriate color cuts. Such cuts were explored by Ivezić et al. (2005). This paper used 153 RRL stars from the QUEST survey (Vivas et al., 2004), of both ab and c type, to define a color box in SDSS colors. This lead to the set of equations (5.6).

$$\begin{aligned} 0.99 &< u_0 - g_0 < 1.28, \\ -0.11 &< g_0 - r_0 < 0.31, \\ -0.13 &< r_0 - i_0 < 0.20, \\ -0.19 &< i_0 - z_0 < 0.23. \end{aligned} \tag{5.6}$$

To determine how well the color cuts of (5.6) worked, a search for RRL stars in version 1 of the LMCC catalog using only variability index L, g magnitude, and classification as a star. To limit the number of false positives a very limited range of L and g were searched ($11 \geq L \geq 5$ with a $g < 18$). The 109 RRab and 63 RRc that resulted from this search are shown in figure 5.2.

It quickly became apparent from figure 5.2 that a large number of RRL stars were being excluded from the sample, primarily due to a lack of u information in the LMCC catalogs. To help correct for this issue, a much less stringent set of color cuts was developed. These cuts, shown in equations (5.7), do not rely on the $u_0 - g_0$ color, which is a powerful discriminator, but one that relies on the often poor u filter. Due to incomplete sampling of the lightcurves, the average colors used to select RRL candidates missed a few on the edge, so the new cuts were expanded by 10% to bring in close cases. The old and new color cuts are compared in figure 5.2 where the solid lines represent the original color cuts from (5.6) and the dotted lines represent the expanded cuts from (5.7).

$$\begin{aligned} -0.13 &< g_0 - r_0 < 0.33, \\ -0.14 &< r_0 - i_0 < 0.23, \\ -0.21 &< i_0 - z_0 < 0.25. \end{aligned} \tag{5.7}$$

5.1.4 Final Candidate List

Optimizing RRL candidate selection requires balancing the two methods for finding RRL in a large sample of stars: the variability index and color cuts. As described in subsection 5.1.1, the variability index L is very good at picking out variable stars. There are two ways, though, that non-RRL stars can appear in the sample. The first is that their are other types of variable stars, the most important in a contamination context are binary stars. Eclipsing binaries, can have period aliases that look very much RRc stars, and as such are picked up by the a variability index search. They are also much more common than RRL stars are, and therefore represent a significant contamination source.

The other issue is that photometric errors tend to become under estimated at dimmer magnitudes. This leads to a greater increase of false positives just to random error in the photometry. This issue is exacerbated by the fact that some of the 2005 SN data was taken under non-photometric conditions. This can lead to deviations from the mean magnitude, which are significant enough to appear in a variability index. These two issues mean that the variability index alone is not good enough to pick out a significant number of RRL, without also finding many contaminating stars.

The other method of picking out RRL based on their unique colors due to their location on the HR Diagram also has some issues related to limitations in the LMCC data set. The most problematic issue is that, as discussed in subsection 5.1.3, the u filter is missing or inadequately sampled in the LMCC. Unfortunately, $u_0 - g_0$ is the most stringent of the color cuts. This is issue is made more difficult because not

Table 5.1. RRL Candidate Search Parameters.

Search	L	Type[a]	$\leq g_0$	# Epochs g, r, i	Color Cuts	# Stars
First	≥ 8	> 4	20.0	$\geq 5, \geq 5, \geq 5$	None	812
Second	≥ 5	> 4	20.0	$\geq 5, \geq 5, \geq 5$	Eq. (5.7)	1228
Third	≥ 2	> 4	21.5	$\geq 5, \geq 5, \geq 5$	Eq. (5.6)	438
Combined	...	...	...	...	...	1675

[a]This is the average of the star or galaxy designation that SDSS gives each measurement where a galaxy is 3 and a star is 6.

all of the RRL lightcurves are sampled fully. This can lead to average colors that lie somewhat outside of the expected ranges.

To compensate for these two competing issues, a three-tiered system for selecting RRL candidates was used. The first variability search is the most inclusive in color space. As shown in table 5.1, it depends only on the Welch-Stetson variability index L and some basic quality assurance parameters. One important but often overlooked parameter is the object type. In SDSS all objects are typed as stars or galaxies. Stars have a value of 6 and galaxies have a value of 3, and each epoch for a given object is typed independently. The parameter I call *Type* in table 5.1 is the average of the SDSS type over all the epochs. This is less than 6, because stars can be misidentified if they are crowded in bad seeing conditions.

The second tier search uses the relaxed color cuts described in equation (5.7). This allows for candidates with a lower L value while cutting back on contamination from non-variables and non-RRL stars. The minimum L for each cut was chosen based primarily on star counts. As can be seen in figure 5.3 the number of stars rapidly increases as one goes below $L = 8$ in the no color cut situation and $L = 5$ in the relaxed color cut search.

The third and final tier search using the color cuts specified in (5.6) provided a means to get down to a much lower L and also push to a much dimmer g_0 magnitude.

As can be seen in figure 5.3, the third search is very tight, and is resilient against significant contamination. This is at the cost of losing stars that may have poor u magnitudes or unusual colors due to incompleteness. These three searches were then combined to produce a total of 1675 candidates as shown in table 5.1.

5.2 Variable Identification

Once the RRL candidates have been identified it is necessary to use visual identification to separate out the true RRL stars from the other variable and non-variable stars. The first step in doing this is determing the period of each of the stars. As was discussed in section 3.3, there are a number of methods for finding the period of a periodic variable star. The period finding method that was ultimately decided upon was a program out of the MACHO project called supersmoother. The two most likely periods for each candidate from supersmoother are then used to phase the candidate's lightcurve (as discussed in section 3.3). The resulting phased lightcurves are then typed by eye. This is done by looking for the characteristic shapes and periods of RRL stars. The stars identified as RRL from this process have their lightcurves fit to known RRL templates. This process is done for two reasons, one it can help fill in gaps in the lightcurve, and two it provides another way of typing the RRL. Finally, the results are plotted on a period-amplitude diagram. Stars that deviate from their expected position on the diagram are then reanalyzed more closely to check for incorrect identifications or periods.

5.2.1 Finding the period: Supersmoother

The supersmoother algorithm for finding periods was developed by Reimann (1994) for the MACHO project. This project was interested in finding gravitational microlensing events caused by massive, compact, halo objects (MACHOs) to get an estimate on the amount of baryonic dark matter in the Galaxy. A gravitational microlensing event occurs when a MACHO passes in front of a distant star. Light from that star is lensed by the gravity of the MACHO causing two images of the distant star to appear. These two images have very small angular separation, so it appears that the star itself has simply become brighter (Cook et al., 1995). As a result of looking for these transient events, the MACHO project took data that was also appropriate for finding variables. The supersmoother program was developed to find periods for many different kinds of variables, and thus does not make assumptions about the shape of lightcurves. It belongs to a class of period finders known as smoothers. These period finders, attempt to fit linear smooths through the data, and then find the period that minimizes the dispersion

For this project, four different period searches were used to attempt to find the appropriate period for the candidate variables. Each of searches used the same supersmoother configuration file with only the period range changing for each one. The configuration file, phase.par, is shown in appendix A.1. The different searches were designed to account for the many different types of variable stars that might be in the sample. These searches are summarized in table 5.2.

Table 5.2: RRL Candidate Period Searches

Search	Period Range (in days)	Candidate Type	x-Axis
First	0.1 - 100	All	Phase
Second	None	Aliased	HJD
Third	0.01 - 3	Aliased & Short	Phase
Fourth	0.1 - 3	RRL	Phase

The first search was designed to pick up most types of known periodic variables including RRL and Cepheids. All of the candidate variables were included in this search. The two most probable periods for each candidate were plotted and the variables were typed using the metric shown in table 5.3. Based on the type given to each candidate, the next three searches were run in turn on the candidate type specified in table 5.2. After each search, the types were updated.

Table 5.3: Variable Typing Metric

Abbrev.	Type	Characteristics	# Found
a	Aliased	Period around 1 day	823
ab	RRab	Period approx. 0.4-1.0 days	305
c	RRc	Period approx. 0.2-0.4 days	116
ev	Eclipsing variable	Two eclipses	93
i	Interesting	Periodic w/ good lightcurve	13
lpv	Long period variable	Periods of hundreds of days	5
ms	Main sequence	Period 0.01-0.2 days	4
n	Not variable	One or two bad points	86
o	Other variables	Lightcurve is indeterminate	73
s	Short	Period < 0.2 days not clearly an ev or ms	133
u	Unclassifiable	Too few points to type the lightcurve	14
type+B	Blazhko effect	Star shows scatter near max or min.	35
type+?	Uncertain type	Low confidence of assigned type	24

In the second search, supersmoother was not used, rather the one day aliased candidates were plotted as a function of Heliocentric Julian Date (HJD). In many cases, it became obvious that they were in fact long period variables, which supersmoother was unable to fit due to the 100 day maximum period limit in the first search. The third search concentrated on the short period variables and remaining aliased variables. In this case, supersmoother was run with a period range including the low period end between 0.01 and 0.1, in general searches this is not done because it greatly increases the time it takes to find a correct period. This low period searching picked up many main-sequence pulsators such as δ Scuti and SX Phoenicis stars. It also did a better job of picking out periods for eclipsing variables. The fourth and final search was run on the stars that were marked as RRL of some type. By constraining the period search to the much smaller range of 0.1 to 3 days compared to the first search, the initial search grid used by supersmoother was much finer increasing the chance of finding good periods.

5.2.2 Finding the period: Template Fitting

Using the most common settings supersmoother produces up to 15 different possible periods. In most cases, the best period is listed first or second in the .per file. In those situations when this is not the case due to, for instance, a strong alias, another technique must be used to find the best period. One such technique is template fitting. In template fitting, a series of generalized lightcurve templates are fitted to the phased data. The best fitting template/period combination provides not only the best RRL period for a given variable, but also is useful for typing RRL that have incomplete lightcurves.

The RRL templates used in this project come from Layden (1998). For the RRab stars he used 3 to 4 well sampled RRL lightcurves from Nikolov et al. (1984) for each template. Each lightcurve was normalized from 0 to 1 in phase and 0 to 1 in magnitude. He also included an RRc template, a sine wave and two binary star templates. These are shown in Figure 5.4. These templates are fit to the lightcurves using a Levenberg-Marquardt method for minimizing χ^2 (examples found in Press et al. (1992)). The fitter was run over all 15 available periods and all 10 templates to find the lowest χ^2 value. In general the fit with the lowest χ^2 value was taken, although, in some cases there were bad points are underestimated errors that made the best fit not have the lowest χ^2. Ultimately all of the RRL candidates were examined by eye to ensure that the automatic template fitting routine worked correctly. By fitting the lightcurves to templates, not only was there an independent source of variable typing information, but also the epoch of maximum could be determined as well as the mean magnitude (both intensity and magnitude weighted) and amplitude.

5.2.3 PERIOD-AMPLITUDE DIAGRAM

Once all of the period finding and template fitting is complete, there is one more tool that can be used to determine how well the fits worked. This tool is the period-amplitude diagram. In this case the g filter was used for measuring the amplitude and is shown in Figure 5.5. The figure is divided into four distinct regions allowing for the selection of aberrant points. The RRab stars and RRc stars clearly cluster in their own respective parts of the diagram. Those points that were significantly deviant from their respective locus (i.e. appeared in an incorrect region) were reexamined in detail. The primary source of issue with most of the deviant points was that an alias had been selected for the period, or an incorrect type had been assigned due to poor template fitting. Once these concerns were corrected, the resulting period-amplitude diagram is found in Figure 5.6.

The final period-amplitude diagram has the lines appropriate to two different possible sequences for the Oosterhoff groups. The standard linear sequences from Clement & Shelton (1999); Clement & Rowe (2000) are based on least squared fits to the period-amplitude diagrams for "normal" RRab lightcurves in OoI and OoII clusters respectively. The derived equations for these lines can be found in equations (5.8). More recently, Cacciari et al. (2005) revisited M3 in particular, but also other globular clusters in the literature and found that a quadratic line actually fit the RRab in the period amplitude diagrams better. These lines are also described in equation (5.8). These equations are defined in the V filter system, so they needed to be transformed to g. To do this, we used the transformations based on the HK survey in Zhao & Newberg (2006). This lead to a ratio of amplitudes of $A_g/A_V = 1.17$.

$$\begin{aligned}
A_V &= -7.1314\log(P) - 0.85687 && \text{OoI} \quad \text{Clement} \\
A_V &= -4.93961\log(P) + 0.127973 && \text{OoII} \quad \text{Clement} \\
A_V &= -2.627 - 22.046\log(P) - 30.876(\log(P))^2 && \text{OoI} \quad \text{Cacciari} \\
A_V &= -1.415 - 18.341\log(P) - 30.876(\log(P))^2 && \text{OoII} \quad \text{Cacciari}
\end{aligned} \tag{5.8}$$

Looking at Figure 5.6, it is not clear which set of lines is necessarily the better fit to the data, but what is clear is that there is a very strong OoI component to the halo sample as has been seen in previous work (Lee & Carney, 1999). There also appears to be a far number of Oosterhoff intermediate RRab stars. The photometric results for the individual stars are in Table C.2 located in Appendix C. Example lightcurves are located in Appendix B. We will return to the period-amplitude diagram for a more thorough analysis in Chapter 8.

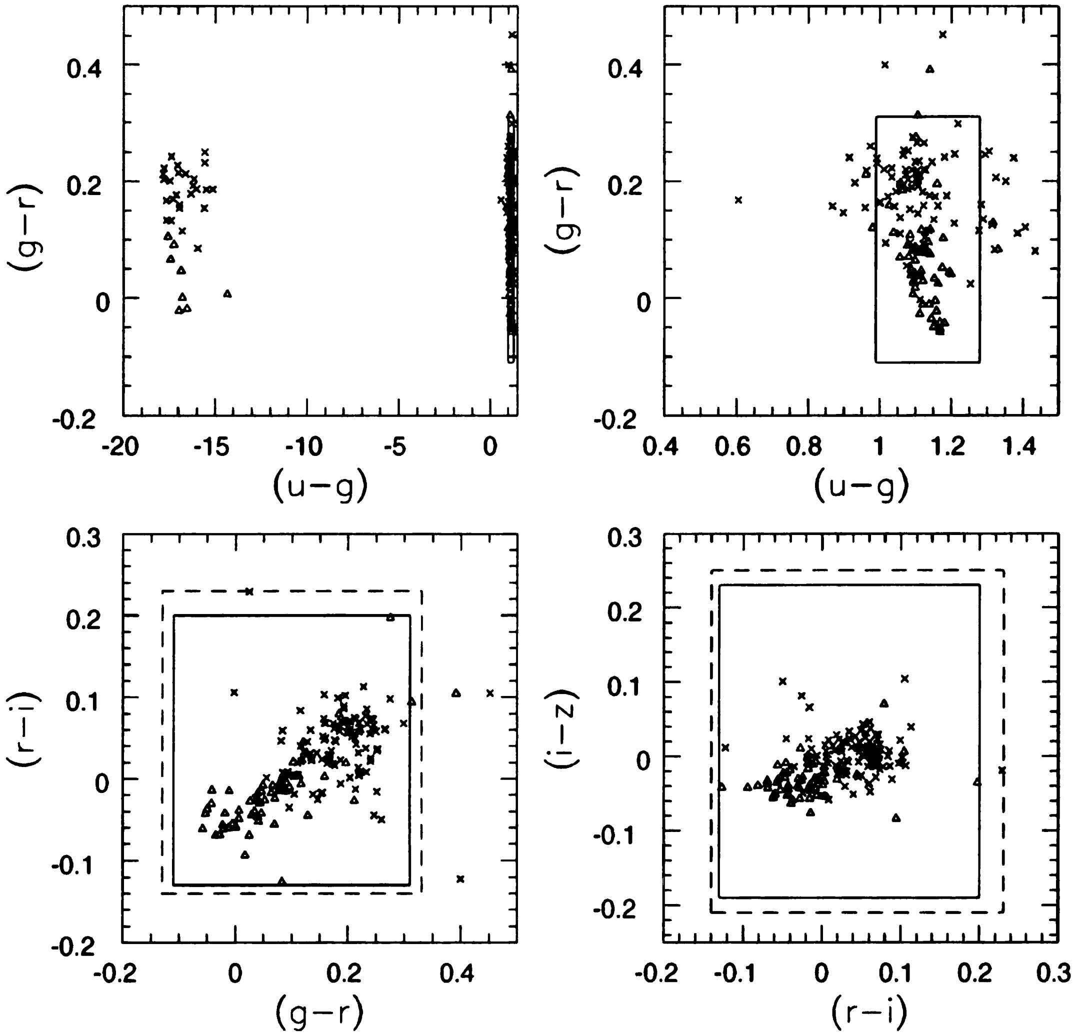

Figure 5.2 Plots in color space of RRL stars selected without color cuts with x for RRab and triangles for RRc. The solid lined boxes are color cuts from Ivezić et al. (2005). The dashed lined boxes are the expanded boxes designed to pick up more RRL.

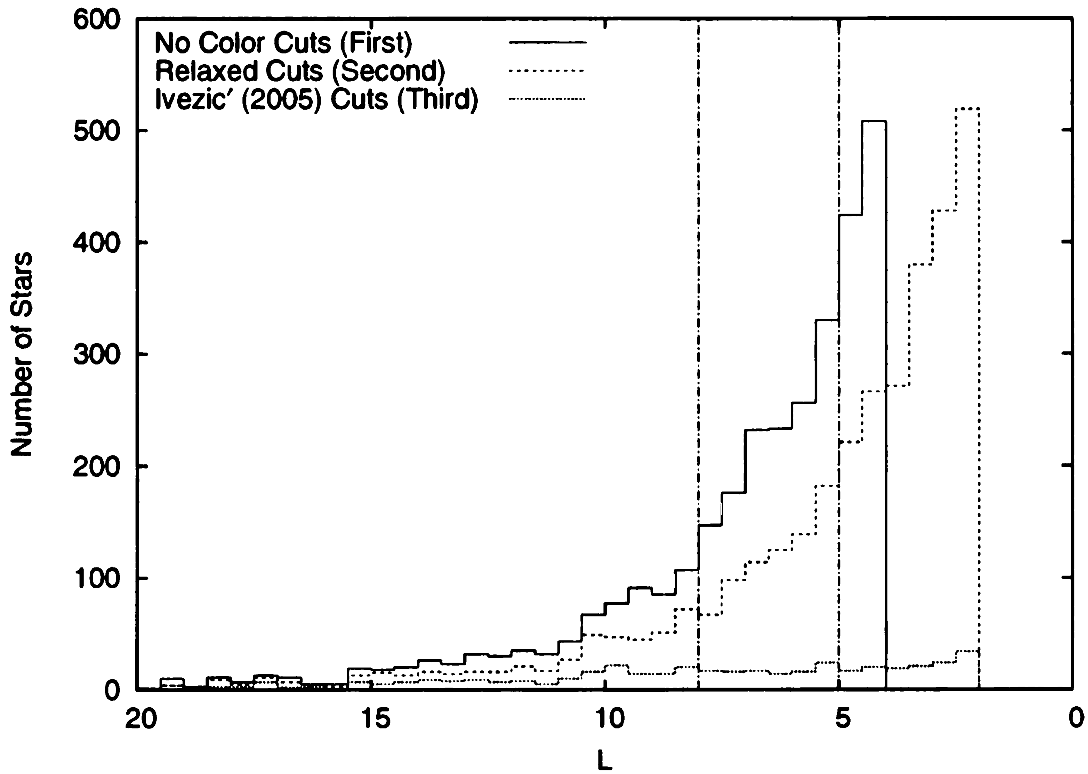

Figure 5.3 The three histograms are of the stars selected by the three variability searches described in table 5.1. The two vertical lines show the L cutoffs for the first and second searches at $L = 8$ and $L = 5$ respectively.

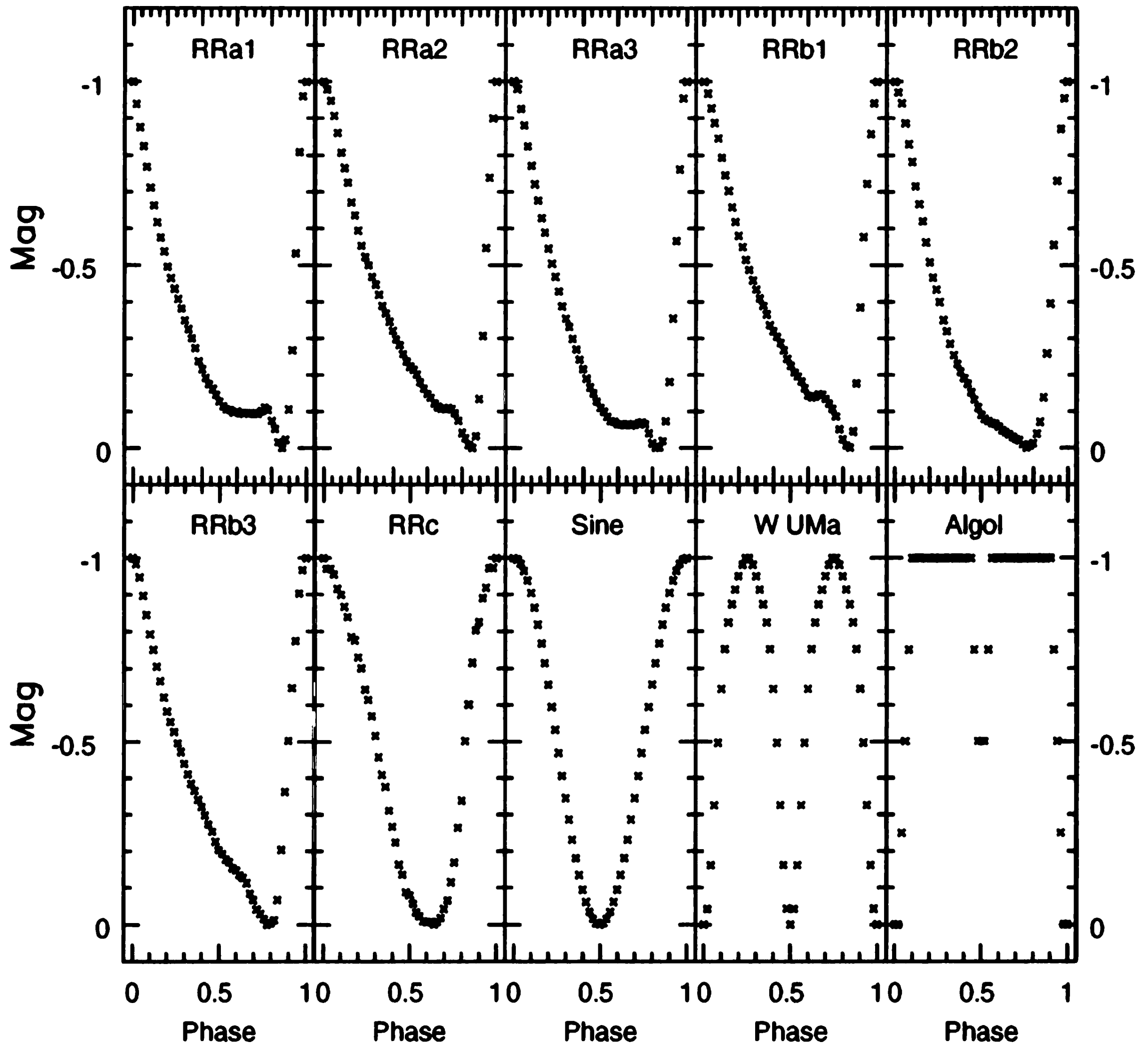

Figure 5.4 The ten templates used to fit the RRL lightcurves. These include six for RRab type and one for RRc type. Also a sine wave and templates for binary stars were also included. All of the templates were normalized to between 0 and -1.

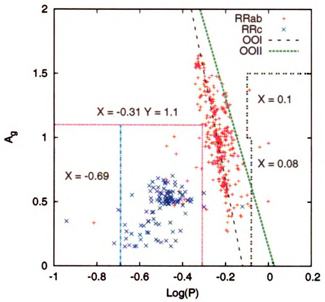

Figure 5.5 This period-amplitude diagram shows the RRL stars divided by type. The RRab and RRc clearly cluster together, although there are a few clearly not in the right part of the diagram. The diagram is divided into four blocks used to check for aberrant points. The mean RRab lines for OOI and OOII are plotted.

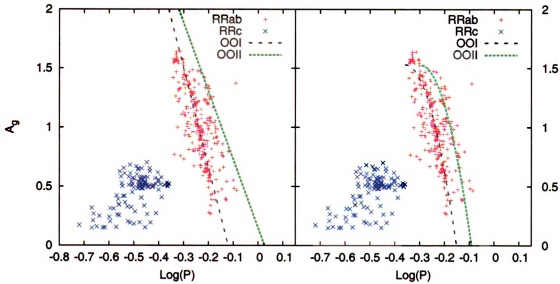

Figure 5.6 The final period-amplitude diagrams for the SDSS variables. The left panel shows the OoI and OoII lines from Clement & Rowe (2000). The right panel shows the OoI and OoII quadratic lines from Cacciari et al. (2005). Each of these lines were transformed into the g band by using $A_g/A_V = 1.17$

CHAPTER 6: SPECTROSCOPIC OBSERVATION AND DATA REDUCTION

In order to use the RRL stars as tracers of the Milky Way halo, it is necessary to have kinematic information about these stars. There is a certain amount of this information available from the HLC proper motion catalog, but this is by its very nature limited to relatively close stars. Ultimately, one needs radial velocities and metallicities to determine both the distances and kinematics of RRL stars. For this project, that information comes from two sources. The first is an observing run specifically designed to get radial velocities and metallicities from these stars at the Cerro Tololo Inter-American Observatory (CTIO) four meter Blanco telescope. These observations were synchronized with the lightcurves from the LMCC catalog to get observations at the best possible phase.

The second source of radial velocity and metallicity information is from the SDSS spectroscopic surveys. In this case, the RRL were not specifically targeted, but instead were happened upon serendipitously as part of other campaigns. These spectra have the benefit of being able to reach much deeper than the 18th magnitude limit in V of the Blanco data, but are limited in usefulness in some cases. This is because they were taken at random phase, and perhaps more problematically are actually composite spectra made from the summation of a few spectra, which again were not necessarily taken at the same phase. This, however, was a fixable situation because the individual spectra that go into making the composite spectra became available.

6.1 CTIO Blanco 4m Data

6.1.1 Observations

The spectroscopy done at the Blanco 4m telescope at CTIO was obtained on the medium-resolution R-C Spectrograph, RCSPEC. The RCSPEC is a single-slit spectrograph, which uses a grating to disperse the light from a target object onto a Loral 3K CCD, which is a 3000 x 1000 pixel camera. For this project, the optical setup was a slit width set to 1.5 arcsec, the decker set to 2, and the collimator set to blue. Since the primary spectral lines of interest for this survey were the CaII H and K lines as well as the Balmer lines, the KPGLF grating was used at a tilt of 49.928 which resulted in a wavelength range of 3505Å to 5118Å with a 0.51 Å/pixel plate scale. A $CuSO_4$ filter was used to limit light leakage on the red end of the spectrum. The final resolution of the spectra was $R \approx 2300$. The targets were observed over the course of five nights during Aug/Sep of 2007. This resulted in 120 spectra of RRL stars.

6.1.2 Image reduction and Spectral Extraction

The spectroscopic images were calibrated and reduced using one of the standard astronomical software suites called Image Reduction and Analysis Facility, IRAF[1] (Tody, 1986, 1993). The methods used were based on *A User's Guide to CCD Reductions with IRAF* by Massey (1997). The images were processed using the normal methods of bias subtraction, flat fielding and bad pixel removal employing primarily the CCDPROC task in the IMRED and CCDRED packages. Bias subtraction is done to remove electrical zero point from the digital image. Flat fielding is a process by which an image of a uniform object, usually the twilight sky or an illuminated white spot in the dome, is used to calibrate out sensitivity variations across the CCD, as

[1]IRAF is distributed by the National Optical Astronomy Observatories, which are operated by the Association of Universities for Research in Astronomy, Inc., under cooperative agreement with the National Science Foundation.

well as deal with some kinds of optics issues. The spectral shape of the flat lamp was removed using the RESPONSE task.

Once the images were calibrated they were then processed to transform the two dimensional images into 1-d spectra. The process we used to extract the spectra was based on the document *A User's Guide to Reducing Slit Spectra with IRAF* by Massey et al. (1992). The background was removed from the object spectra by using the task APALL, part of the KPNOSLIT package. During this process the light that is in the object aperture is summed to make a 1 dimensional spectrum. In order to use the 1-d spectra it is necessary to calibrate the wavelengths versus a known source. For this purpose a number of Helium-Neon-Argon comparison lamps were observed. The calibration lamps must be taken after any significant movement of the telescope because flexure in the spectrograph itself varies as one moves across the sky. The IDENTIFY task was used to assign wavelength values to the known lines of the comparison lamp spectra. Finally a wavelength solution was applied to each object spectrum using the associated comparison lamp spectrum. This was done by the task DISPCOR, which also linearizes the final object spectrum. The resulting spectra had cosmic rays removed by hand. An example spectrum sampled at various stages from beginning to end of this process is shown in Figure 6.1.

6.1.3 Radial Velocities

Now that the spectra were fully processed, it became possible to determine the quantities of interest: the radial velocities and the metallicities. The radial velocities are found by looking for Doppler shifts in the spectral lines. The Doppler shift is defined by the change in the central wavelength of an absorption line from the laboratory value, $\Delta\lambda$, due to the radial velocity, the velocity of the star along the line of sight, of a star through the equation:

$$\frac{\Delta\lambda}{\lambda_0} = \frac{v}{c}$$

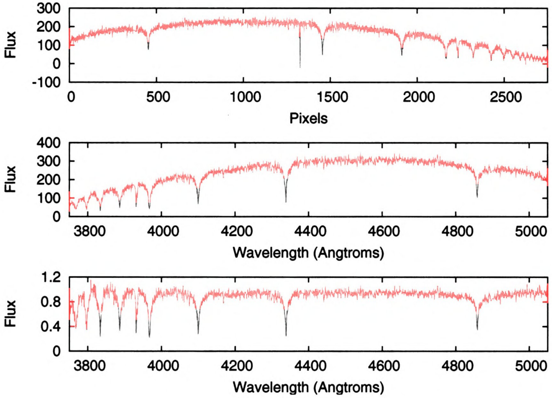

Figure 6.1 Examples of CTIO spectra at different stages of reduction. Top: Raw 1-d spectrum. Middle: Spectrum with wavelength solution and bad columns removed. Bottom: Final continuum flattened spectrum.

where v is the velocity of the star, c is the speed of light, and λ_0 is the laboratory rest wavelength of the line. To determine the radial velocities two different methods were employed. The first was to use a line by line measurement method and the second was to match up the whole spectrum to a template spectrum using a cross-correlation algorithm. For the metallicities a line index method based on measurements of the CaII K line were used.

The first method to determine the radial velocity of each star was based on the individual lines shown in Table 6.1. For each line a 10Å search radius around the lab frame value is used to try and find the line peak in the object spectrum. Then a Gaussian is fit to the line taking into account asymmetries. After this has been done for each line, the lines are taken together and a weighted mean and standard deviation is found. If a single line deviates significantly from the rest, then it is removed and the mean is recalculated. This is the same basic techniques as in Beers et al. (1990). This method benefits from being straightforward, but is subject to issues like line misidentifications. Also having one or two bad line measurements, can strongly influence the final value of the mean, although this is relatively easy to check and correct for. The heliocentric correction for these spectra was done using the RVCORRECT task in the ASTUTILS package.

Table 6.1: Spectral Lines used to Determine Radial Velocity

Name	Wavelength (Å)	Series	Element
H_8	3798.329	Balmer	H
H_6	3888.896	Balmer	H
K	3933.669	Fraunhofer	CaII
H_δ	4101.637	Balmer	H
H_γ	4340.319	Balmer	H
H_β	4861.255	Balmer	H

The second method for determining the radial velocity involves doing a cross-correlation fit against template spectra. The template spectra represent a grid of metallicity and temperature for horizontal-branch stars. The template spectra are synthetic and were created using the ATLAS9 model atmospheres from Kurucz and using the spectral synthesis program SPECTRUM (Gray & Corbally, 1994) and were provided to us by Wilhelm (private communication). The first step is to find the appropriate template for each star. This is done in a non-interactive mode of the FXCOR task. A lorentzian function was applied to the correlation peaks for each template. Once the best template was found, the FXCOR task was run interactively using a parabola to find the radial velocity with the best correlation peak. This method has the benefit that it uses the entire spectra to determine the radial velocity. The caveat to this is that low signal to nose and defects in the spectra can cause poor radial velocity measurements.

Once both velocities were determined for each star, a comparison was made between the two velocities. If the absolute difference between the two was less than 15 km/s, then they were weighted averaged together. If the absolute difference was larger than 15 km/s, then the fits for both methods were examined and if the line by line method returned consistent velocities for each line it was used, otherwise the template method's velocity was used.

6.1.4 Determining Metallicity

Determining the metallicity of RRL stars requires extra care compared to non-pulsating stars. This is because as the RRL star goes through it's pulsation cycle the temperature of the star changes. This is reflected in the strength of the hydrogen Balmer lines for these stars. As was mentioned in Section 3.1 the spectral type measured by these lines varies from A7 or A8 at maximum to F5 or F6 at minimum light for RRab and for RRc stars A7 or A8 at maximum to F1 or F2 at minimum. An example of how the spectrum of a star can change through its pulsation can be seen in Figure 6.2. The situation is even more complicated in RRab stars where significant shocks can form in the atmosphere causing line doubling near maximum brightness.

One common method for determining metallicity is to measure the strength of the CaII K line. There is relation between [Ca/H] and [Fe/H] and the CaII line is much easier to measure in low to medium resolution spectra than the more numerous, but weaker, iron lines. Using this basic principle Preston (1959) developed the ΔS system for measuring the metallicity of RRL stars. The ΔS is the difference between the spectral type as determined by the Balmer Hγ and Hδ lines and from the CaII line. In metal poor stars, ΔS is large and in metal rich stars it is small. The ΔS

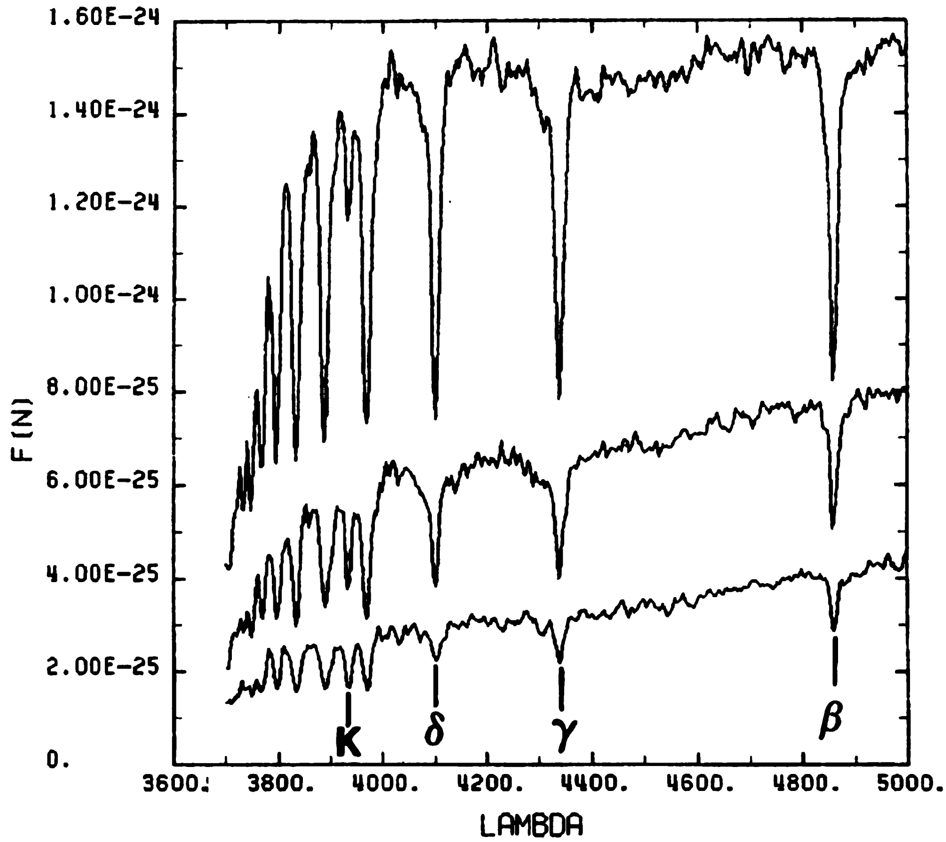

Figure 6.2 An example of how the spectrum of the RRab star changes as a function of phase. The above spectra are of the RRab star RW Dra. The top most spectra is the star near maximum and the bottom one is the star at minimum. The line strength of CaII K versus the Balmer lines clearly changes. Figure from Smith (1995).

system was defined for RRab stars at minimum light although it was extended to other phases, although still avoiding maximum, by Butler (1975) and Smith (1986). Kemper (1982) then extended the ΔS system to include RRc stars. There have been a number of papers dealing with alterations to the basic ΔS system, but there have also been parallel methods that are very similar. For instance, Freeman & Rodgers (1975) developed a method that is based on pseudoequivalent widths of the Balmer lines and CaII K. The method we followed, builds on that study and was developed by Layden (1994).

We measured the equivalent widths of Hγ and CaII K, using a Voigt profile fitting routine as in Wilhelm et al. (1999). The metallicities were then determined following Layden (1994) and were used as the first pass to determine a distance to each of our stars using the methods describe in 7.1.3. Then the equivalent widths were corrected for interstellar CaII contributions using Beers (1990). These corrected equivalent widths were then used to get a final metallicity measurement.

6.2 SDSS Data

SDSS has a wide variety of spectroscopic programs and has taken a large number of stellar spectra. As it happens, RRL stars have been accidentally measure from time to time as part of other programs. It soon became apparent that over 300 spectra had been taken of our stars! On the downside, these spectra were observed without any of the precautions usually taken when dealing with RRL stars. This issue is further complicated by the fact that SDSS spectra are not in themselves single observations, but rather are composites of several single observations, which in some cases are taken over multiple nights. This makes metallicity determinations difficult since in many cases it is impossible to determine what different phases the combined spectrum was created from, and this, as shown in Figure 6.2, would lead to highly inaccurate metallicity determination.

Relatively recently the single-epoch spectra data has become available, although only as two dimensional spectra. Processed one dimensional single-epoch spectra became available from West (2008). These spectra only contained flux and error as a function of wavelength, although they were processed using the same software as Adelman-McCarthy et al. (2008). To analyze these spectra further, the headers from the combined spectra were copied to each of single-epoch spectra to create a starting point for further analysis. It soon became apparent that the signal to noise ratio on many of the single-epoch spectra was too low to able to determine radial velocities and metallicities. As a result, we recombined the single-epoch data taking into account the phase of each spectra, and an example of this is shown in Figure 6.3. This recombination was done by taking the weighted mean of each of the spectra, removing the highest point at any given wavelength to help correct for cosmic-rays.

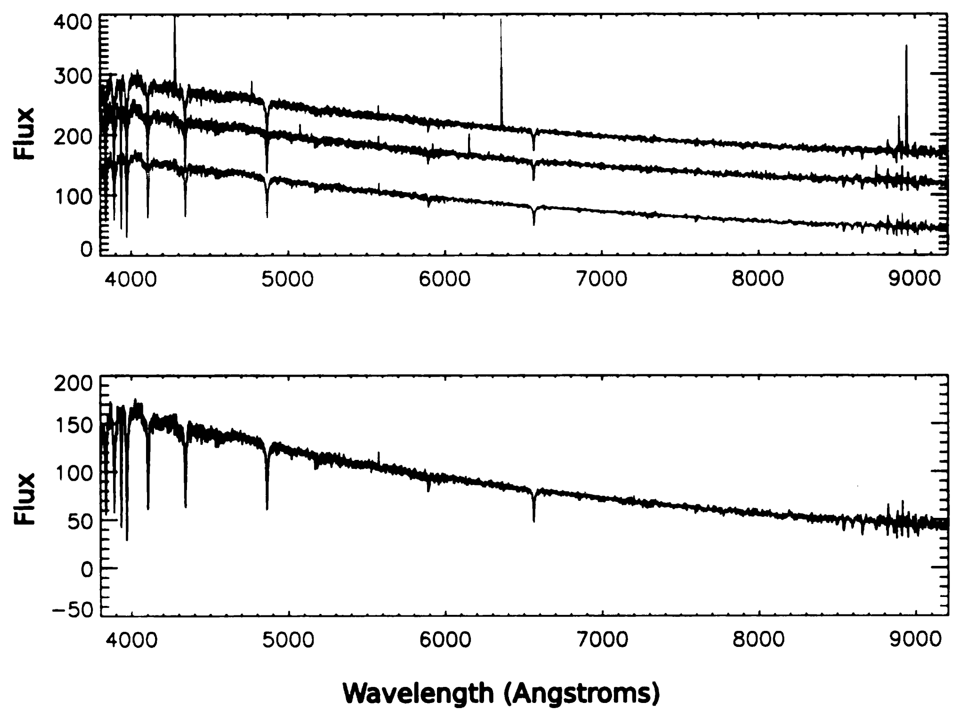

Figure 6.3 An example of the recombination of three single-epoch spectra (top graph) for a given star at roughly the same phase into a spectrum with much better signal to noise (bottom graph), and with most of the cosmic rays removed.

Once the recombination was done, the spectra were processed through the SEGUE Stellar parameter pipeline (SSPP) described in Lee et al. (2007). This pipeline created as part of SDSS II determines stellar parameters including temperature, effective gravity, metallicity and radial velocity through a number of different methods. The two quantities that we are interested in of course are metallicity and radial velocity. The radial velocities that would normally come out of the SDSS spectroscopic reduction pipeline (Stoughton et al., 2002) are not usually reliable because they are found using the normal combined spectra. The SSPP run on the recombined spectra redetermines the radial velocities using strong absorption lines (Lee et al., 2007). Since radial velocities need to be corrected for phase, we will discuss them further in Section 7.2.

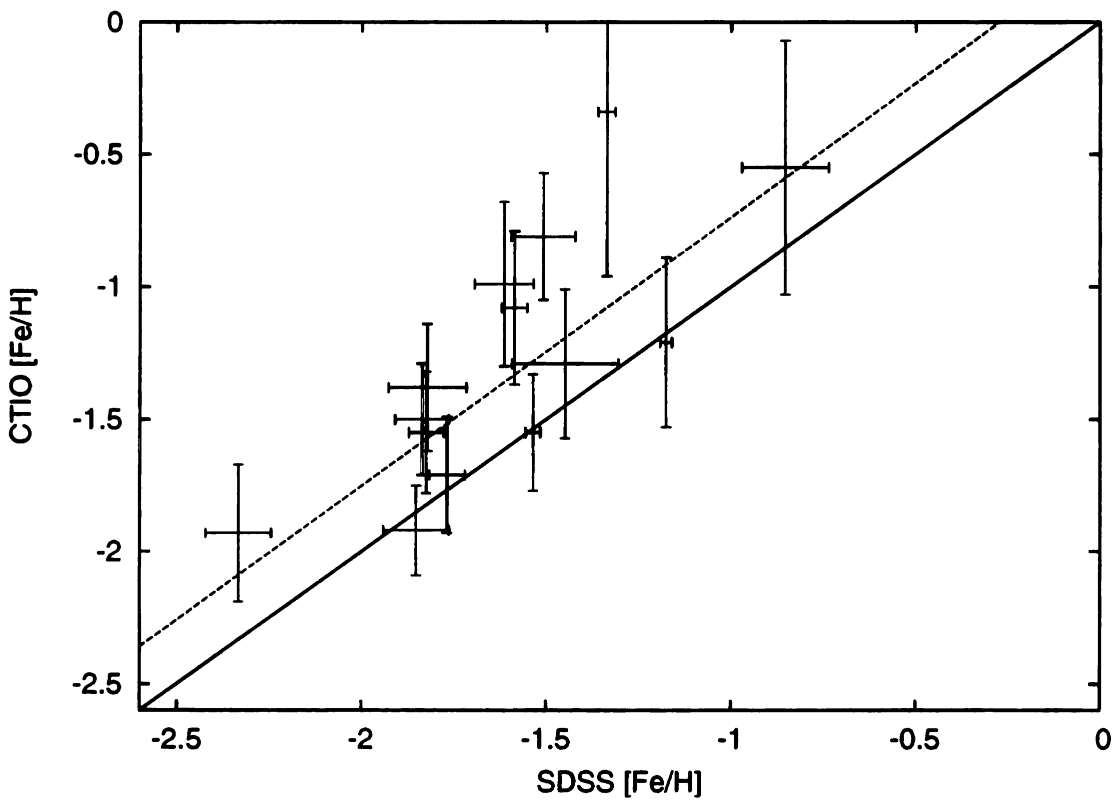

Figure 6.4 A comparison between the metallicities from the SDSS spectra processed using the SSPP and the CTIO spectra processed using the method of Layden (1994). The solid line is the unity line. The dashed line is the least squares fit.

The metallicity determinations in the SSPP use up to 77 separate measurements of line indices. These methods are fully described in Lee et al. (2007). For our purposes the primary issue is to ensure that the RRL stars are near minimum for these measurements. As described in the previous section, the metallicity of an RRL star is defined at minimum, since the SSPP has no corrections built into it to deal with different phases. For comparing the CTIO spectra and the SDSS spectra we restricted ourselves to the phase ranges of 0.4 to 0.8 for RRab and 0.3 and 0.7 for RRc. Also, we removed stars that showed signs of Blazhko effect since this could lead to poor phase determination. The result of this comparison is shown in Figure 6.4. The dotted line shows the least-squares fit to the data points. As one can see, the relationship is linear, and only removed from the line of unity by a small offset. The equation for this fit is shown in (6.1).

$$[\mathrm{Fe/H}]_{\mathrm{CTIO}} = 1.013(\pm 0.278) \times [\mathrm{Fe/H}]_{\mathrm{SDSS}} + 0.275 \pm 0.077 \tag{6.1}$$

The fit was done in this fashion because the error bars on the CTIO data are larger than on the SDSS data. However, the CTIO metallicity scale is based on a poorly defined zero-point, and so the metallicity system that we will use is the SDSS one. All of the CTIO metallicities will be transformed to the SDSS scale by using the inverse of Equation (6.1) shown in Equation (6.2) with errors calculated using Equation (6.3)

$$[\mathrm{Fe/H}]_{\mathrm{SDSS}} = 0.987 \times [\mathrm{Fe/H}]_{\mathrm{CTIO}} - 0.271 \tag{6.2}$$

$$\sigma^2_{[\mathrm{Fe/H}]} \cong \left(\frac{\sigma_{\mathrm{CTIO}}}{1.013}\right)^2 \tag{6.3}$$

All metallicities in the rest of this document will be on the SDSS system.

CHAPTER 7: PRODUCTION OF DERIVED PARAMETERS

In chapter 6 the observation and reduction of spectra from both the both the SDSS survey and the CTIO Blanco 4m was discussed, however, that was only the first step. The spectra taken represent only 241 of the total 421 RRL stars found in this survey. Using the information gleaned from the reduction of those stars, in this chapter we'll create relationships that will relate photometric observations to metallicity. Also, the radial velocities will be corrected and transformed into frames of reference, where they can be used to explore the kinematics of the halo.

7.1 DETERMINING METALLICITIES & DISTANCES

In general, it is much more difficult to get spectroscopic information about a star than it is to get photometric data. As such, a number of attempts have been made to relate photometric parameters to metallicity. There are two techniques that are of interest to us, and they are Fourier Coefficient fitting and Period-Amplitude-Metallicity relations. Both of these methods attempt to use information about the shape of the lightcurve to determine the metallicity of an RRL star. As a consequence of this, they are primarily used with type RRab stars, which have more variation in their lightcurve shape. Although progress has been made on the Fourier method with RRc stars in Morgan et al. (2006) there are theoretical reasons to believe that the Period-

Amplitude-Metallicity relation may not be useful for RRc stars (Bono et al., 2007). So for this work both of these methods will be restricted to RRab stars.

7.1.1 Fourier Metallicities

Throughout much of the history of the study of variable stars, lightcurve shape was often discussed in very qualitative terms. In an attempt to bring a more quantifiable method to describing the shape of a light curve, Simon & Lee (1981) decided to use Fourier cosine series to describe the shape of Cepheid variable lightcurves. Simon expanded this work to include RRL stars in Simon & Teays (1982). More recently, Jurcsik & Kovacs (1996) used Fourier sine series to develop a method for determining metallicities. They used a Fourier sine series as shown in (7.1). In this equation A_i is the amplitude of each order, φ_i is the frequency offset, t is the HJD, and ω_i is the frequency. They needed a set of parameters that could be used to relate the different orders of the sine series. The adopted convention was to create a parameter $R_{ij} = A_i/A_j$ to relate the amplitudes and $\phi_{ij} = j\phi_i - i\phi_j$ to relate the frequency offsets.

$$V = A_0 + \sum_{i=1}^{n} A_i \sin[2\pi\omega_i t + \varphi_i] \tag{7.1}$$

Since the various papers on this subject use both sine and cosine series to describe the lightcurves, it is worth noting that the R_{ij} remains the same regardless of whether a sine or cosine series is used. As for the ϕ_{ij}, it can be changed between sine and cosine by adding the factors as appropriate from Table 7.1. The table is cyclic, so to get conversions for higher ϕ_{ij} just start again from the top.

Table 7.1: ϕ_{31} Conversion Chart

Parameter	Factor	Parameter	Factor
Cosine to Sine		Sine to Cosine	

Table 7.1: ϕ_{31} Conversion Chart (continued)

Parameter	Factor	Parameter	Factor
ϕ_{21}	$-\frac{\pi}{2}$	ϕ_{21}	$+\frac{\pi}{2}$
ϕ_{31}	$+\pi$	ϕ_{31}	$-\pi$
ϕ_{41}	$-\frac{3\pi}{2}$	ϕ_{41}	$+\frac{3\pi}{2}$
ϕ_{51}	0	ϕ_{51}	0

Jurcsik & Kovacs (1996) produced a relationship relating the parameters ϕ_{31} and period to metallicity that is shown in equation (7.2).

$$J_{[Fe/H]} = -5.038 - 5.394P + 1.345\phi_{31} \tag{7.2}$$

This relationship is defined for the Johnson V filter, and as such is not of much use for this project, but it does provide a template for how to approach this relation. In this case, we are interested in creating a relation based on the g lightcurves. We used the metallicities from the SDSS spectra and an 8th order Fourier sine series fit to the lightcurve data to create a relationship between metallicity, ϕ_{31}, and period shown in Figure 7.1. In Jurcsik & Kovacs (1996) they used a 15th order sine series, but we reduced the order to prevent ringing in the fit. The relatively small number of stars (32), is because only the best fitting Fourier series were used.

Clearly the ϕ_{31} parameter is the less certain of the two as to be expected, because although our lightcurves are fairly complete, ϕ_{31} is very sensitive to gaps and scatter in the magnitudes. This fit resulted in the metallicity relationship showed in equation (7.3) with an error in the metallicity given by (7.4).

$$[\mathrm{Fe/H}]_{\mathrm{SDSS}} = -4.181(\pm 0.090) - 4.653(\pm 1.043)P + 1.043(\pm 0.270)\phi_{31} \tag{7.3}$$

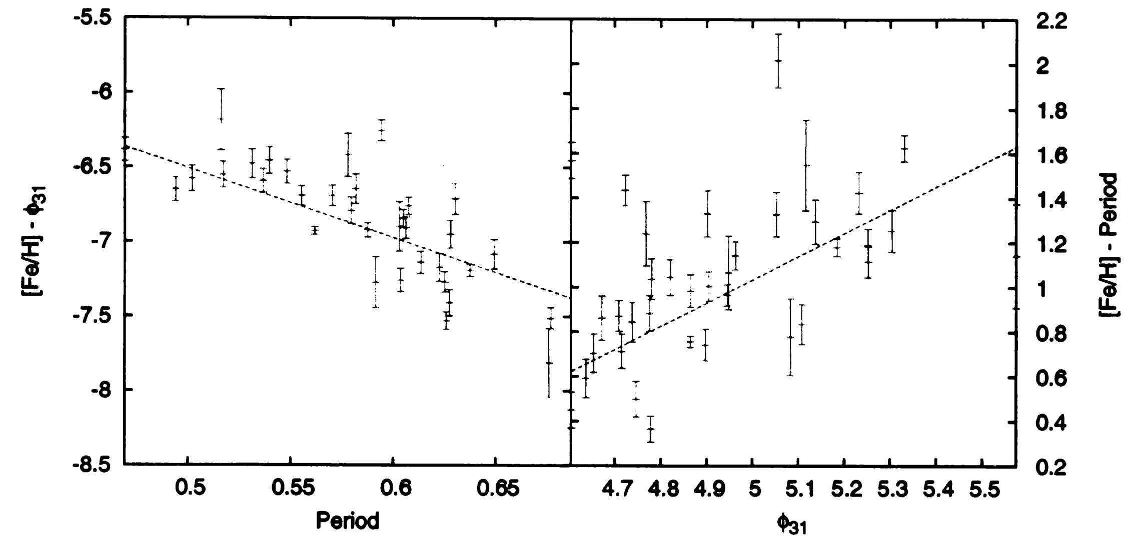

Figure 7.1 The dashed line shows the least squares fit. The plots show the dependence of the fit on the two independent variables, Period (in days) on the left and $\phi 31$ on the right.

$$\sigma^2_{[\mathrm{Fe/H}]} \cong \left(1.043\sigma_{\phi_{31}}\right)^2 \tag{7.4}$$

7.1.2 Period-Amplitude-Metallicity

The Fourier metallicity method is powerful tool for getting metallicites for stars without spectra; Unfortunately it is limited to RRL stars that have fairly complete lightcurves, so another method is necessary. Sandage (2004) found a relationship between the amplitude in the Johnson V filter, the period, and the metallicity of an RRab star. His relationship is shown in equation (7.5).

$$[\mathrm{Fe/H}] = -1.453(\pm 0.027)A_V - 7.990(\pm 0.091)\log P - 2.145 \pm 0.025 \tag{7.5}$$

In general the period-amplitude relation for determining metallicity is has much more scatter in it relative to the Fourier method. This only makes sense given that it uses amplitude, which is much less sensitive to lightcurve shape than ϕ_{31} (Bono et al., 2007). On the other hand, amplitude is a much easier quantity to measure and can be used on relatively incomplete lightcurves. Again we used our own metallicities and the g lightcurves to create a period-amplitude relation. The fit can be seen in Figure 7.2.

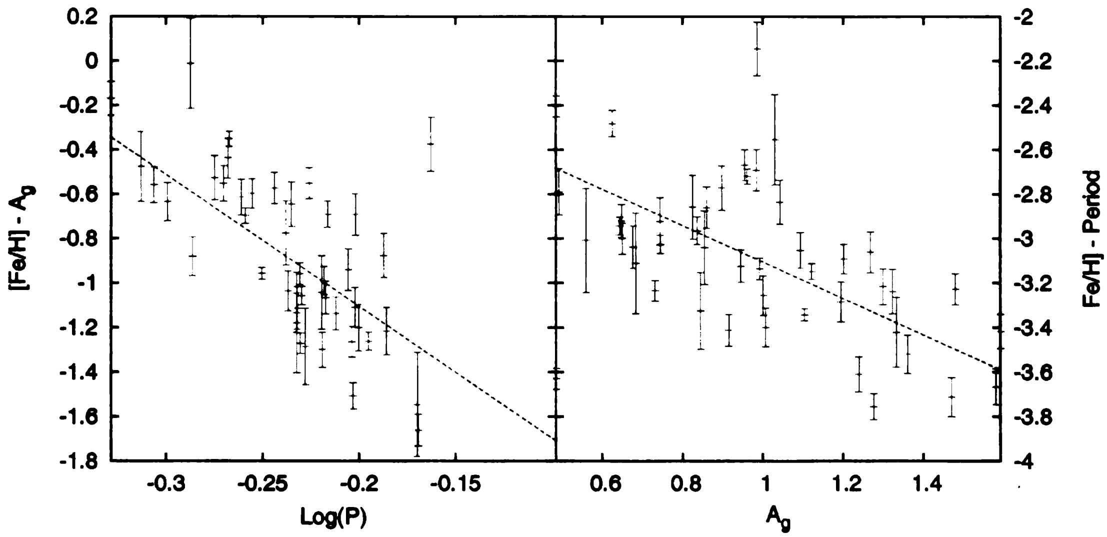

Figure 7.2 The dashed line shows the least squares fit. The plots show the dependence of the fit on the two independent variables, base ten logarithm of the period (in days) on the left and the amplitude in g on the right.

Clearly there is a lot of scatter in the relation, but this method does provide a rough estimate of the metallicity for those stars with poor lightcurves and no spectroscopy. The new period-amplitude relation can be found in equation (7.6) with the errors in the metallicity found in equation (7.7).

$$[\mathrm{Fe/H}]_{\mathrm{SDSS}} = -5.921(\pm 1.204)\log_{10} P - 0.816(\pm 0.191)A_g - 2.289 \pm 0.056 \quad (7.6)$$

$$\sigma^2_{[\mathrm{Fe/H}]} = (1.204 \log_{10} P)^2 + \left(0.191 A_g\right)^2 + 0.056^2 \quad (7.7)$$

7.1.3 Distance

One of the most important properties of RRL stars for the purpose of studying the structure of the halo is the fact that they are very good standard candles. As discussed in Section 3.6, we can use the fact that we know the intrinsic luminosity of the RRL star and the measured brightness to determine the distance to the star using the distance modulus formula:

$$m_g - M_g = 5\log_{10}(d) - 5$$

Where m_g is the apparent magnitude in the g filter, M_g is the absolute magnitude in the g filter, and d is the distance to the star in parsecs. There are two issues that need to be address before the distance modulus can be used. The first is that the absolute magnitude for RRL is normally described in the Johnson V band. The second is that there is some metallicity dependence to the intrinsic brightness of RRL.

There have been a number of papers on trying to determine the absolute magnitude of RRL stars. We followed the work of Wilhelm et al. (2007) to create our M_g vs. [Fe/H] relationship. To start with, we used the zero point of $M_V = 0.55$ for [Fe/H] = -1.6 from Demarque et al. (2000). This was then transformed to the SDSS g band by using a B-V color for RRL stars to be 0.293 and Fukugita et al. (1996) gives $M_g = 0.594$ at [Fe/H] = -1.6. Combining this with the slope of 0.214 from the M_V vs. [Fe/H] relation by Clementini et al. (2003) gives the final absolute magnitude equation shown in equation (7.8).

$$M_g = 0.214[\mathrm{Fe/H}] + 0.94 \tag{7.8}$$

In order to be able use equation (7.8), we had to have the metallicity for each of our RRL stars. A metallicity was assigned for each RRab and most of the RRc stars by combining the results from the CTIO and SDSS spectroscopy and the photometric methods. The results of this are shown in Table 7.2 with N being the number of stars that used that method, and type being the type of RRL star the method applies to. For the RRc stars that had no metallicity determination from spectroscopy, the mean and standard deviation metallicity from the RRc with spectroscopy was adopted for the metallicity and the error respectively. The methods are self-explanatory except for group (C). In that case, since there is no correction for phase, we used a weighted mean of the metallicity from spectroscopy and from the Fourier method when the lightcurve was good enough. The order of the groups from A-E for RRab and F-I for RRc is the order of quality of the metallicity determination with group (I) being used only for distance determination and not for any of the analysis in Chapter 8.

Table 7.2: Methods used for Determining Metallicity for RRL Stars

Group	Type	Method	N
(A)	RRab	SDSS Spectra from 0.5 to 0.8 in phase	52
(B)	RRab	CTIO Spectra	68
(C)	RRab	SDSS Spectra all other phases except maximum w/ Fourier method	46
(D)	RRab	Fourier method	86
(E)	RRab	Period-Amplitude method	53
(F)	RRc	SDSS Spectra from 0.3 to 0.6 in phase	29
(G)	RRc	CTIO Spectra	15
(H)	RRc	SDSS Spectra all other phases except maximum	15
(I)	RRc	Set to mean of other RRc, [Fe/H] $= -1.52 \pm 0.55$	57

7.2 Center of Mass Calculations

One issue unique to using variable stars as kinematic tracers is that they have a component of their radial velocity that is due to the mechanism that makes them variable. In the case of RRL stars, their pulsation is the source of this added radial velocity as discussed in Section 3.1. Before they can be used as tracers, their radial velocity must be corrected to the center of mass frame. For RRab stars, there is a method using a synthetic radial velocity curve developed by Liu (1991). The synthetic curve can be seen in Figure 7.3. The normalized function $S(\phi)$ is scaled by the amplitude in the V filter to get the radial velocity correction for any given phase. To transform our g amplitudes to V, we just used the relation from Section 5.2.3.

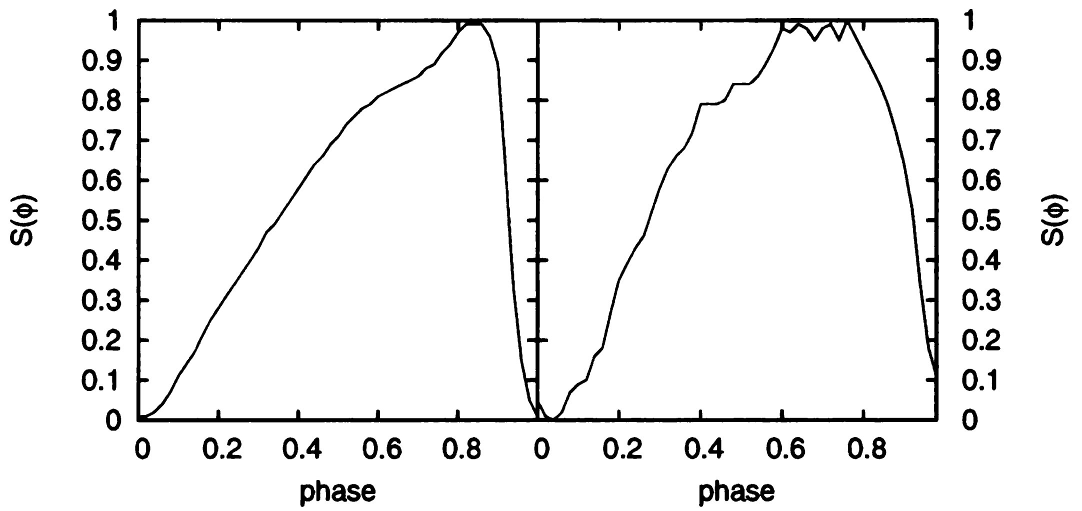

Figure 7.3 The two normalized radial velocity templates were used to correct our radial velocities to the center of mass. The one on the left is for RRab type, the one on the right for RRc type.

As for the RRc stars, the issue is a little less clear cut. There is no standard method for correcting RRc stars, so we followed the lead of Jeffery et al. (2007). We used the radial velocity data from Jones et al. (1988) for DH Peg to create a radial velocity template by fitting the curve with a smoothed spline. Then a simple scaling relation was used to relate V amplitude to radial velocity amplitude. The resulting radial velocity curve is shown in Figure 7.3.

Once the radial velocities have been corrected to the center of mass velocity, it is now possible to compare the radial velocities from the CTIO and the SDSS spectra.

Figure 7.4 shows the fit between the two systems. The transformation equation between the two systems is shown in equation (7.4) with errors in equation (7.10). It is clear from equation 7.4 that there is an insignificant offset and only a slight slope from unity. All the radial velocities were transformed onto the SDSS system.

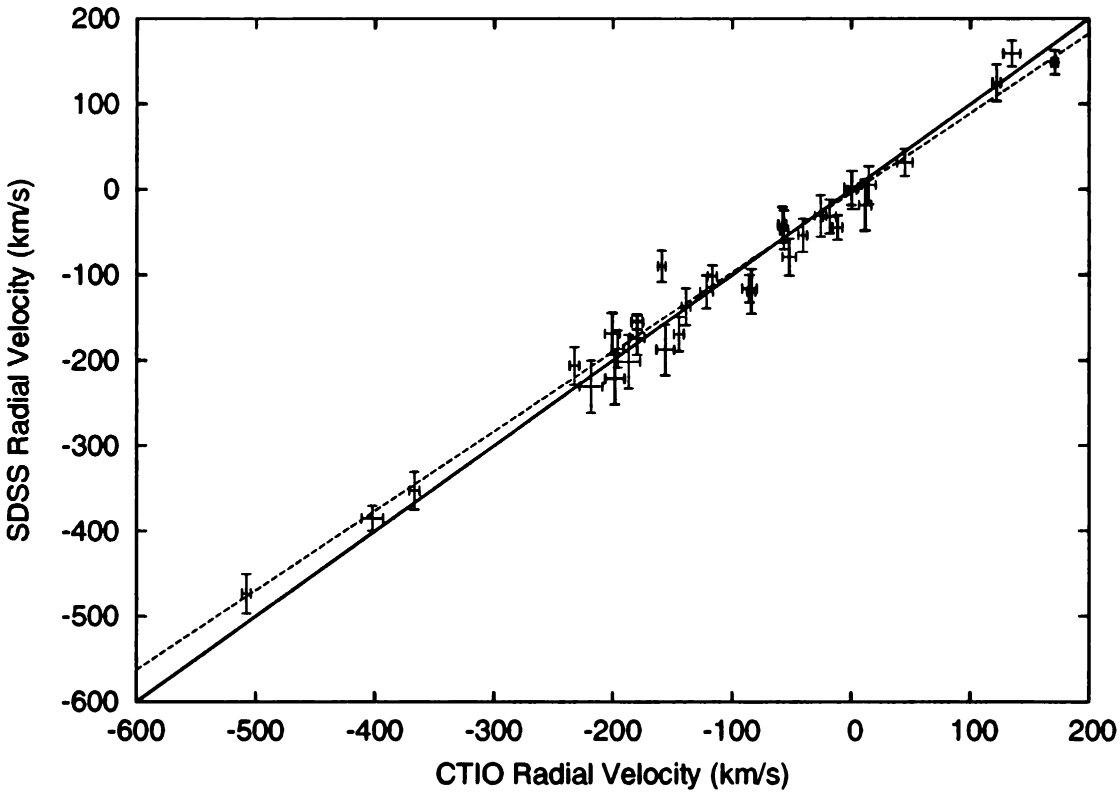

Figure 7.4 The dashed line shows the least squares fit between the SDSS and CTIO radial velocity systems, the solid black line is the line of unity.

$$V_{\mathrm{SDSS}} = 0.931(\pm 0.0258)V_{CTIO} - 3.765 \pm 3.792 \tag{7.9}$$

$$\sigma_V^2 = (0.931\sigma_{CTIO})^2 + (0.0258V_{CTIO})^2 + 3.792^2 \tag{7.10}$$

7.3 Frame of Reference

One of the fundamental issues in trying to understand the kinematics and structure of galaxy is that we observe from a moving platform. For the same reasons that we had correct the Julian date to the heliocentric frame in Section 3.2, so too do the radial velocities have to be corrected to the heliocentric system to remove the motion of Earth's orbit from the radial velocities. This is good enough for comparing different observations, but to look at the kinematics of the galaxy we had to go a few steps further.

First of all, one needs to understand the coordinate systems that are used in astronomy. One of the most common systems used for describing observations is the equatorial system. The equatorial system is effectively a grid system of the longitude and latitude for the sky where the longitudinal coordinate is called Right Ascension, RA, and the latitudinal coordinate is Declination, Dec. In general, unless the object has high proper motion, each star has its own unique RA and Dec. The equatorial system is aligned with the Earth with plus and minus 90° being directly overhead, the zenith, at the north and south poles. RA is often measured in hours going from 0 to 24, with 0 hours being defined at the moment of the vernal equinox, although degrees are also used running from 0 to 360. As one moves to the east on the sky, the RA increases, and at any given time at any given location only 12 hours of RA can be seen from the east to west horizon. For every hour that passes, the RA that passes through the zenith advances by one hour going through the full 24 in a day. Every night at local midnight, the RA is different from the previous night by roughly 4 minutes, completing a full rotation once a year due to the revolution of the Earth about the Sun.

Although the equatorial system is useful for observation, for our purposes, the galactic coordinate system is the most useful. This system where b is the galactic latitude and l is the galactic longitude is shown in Figure 7.5a. These coordinates are analogous to latitude and longitude on Earth. In the l coordinate, 0° points towards the center of the galaxy whereas 180° points towards the anti-center. In b, the North Galactic Pole (NGP) is at +90° and likewise the South Galactic Pole (SGP) is at −90°. One note of caution, l and b are defined at the position of the Earth not the center of the galaxy like some of the other coordinate systems. Another system that is often used is the Cartesian coordinate system (X, Y, Z). In this system X points from the galactic center to the Earth, Y points in the direction of galactic rotation, and Z points toward the NGP. This is a galactic center based coordinate system, although there are other definitions where this is not true.

When talking about velocity, often times a cylindrical system based at the center of the galaxy is used. Figure 7.5b shows the positional components (r, ϕ, z). The velocity components for this system would be (V_r, V_ϕ, and V_z). Another frame of reference that is often used is the space velocity taken with respect to the Local Standard of Rest (LSR). The LSR is defined as a circular orbit in the plane of the galaxy at the radius of the Sun. These velocities are (U, V, W) and their direction is shown in Figure 7.5b. For more information on coordinate systems consult Mihalas & Binney (1981).

With these coordinates in mind, we then proceeded to correct for the Sun's peculiar velocities with respect to the LSR. Since the Sun's orbit is slightly non-circular, we need to correct to this frame. Equation (7.11) transforms from heliocentric radial velocities to LSR radial velocities (Allende Prieto et al., 2006). The Sun's peculiar velocities ($U_\odot$, $V_\odot$, $W_\odot$) = (-9.0, 12.0, 7.0) km/s (Mihalas & Binney, 1981).

$$V_{LSR} = V_{helio} - U_\odot \cos b \cos l + V_\odot \cos b \sin l + W_\odot \sin b \tag{7.11}$$

Once we had the radial velocities in the LSR frame we went one more step, and that was to put the radial velocities into the galactic standard of rest (GSR). This way the LSR's orbit around the Galaxy is removed. This is a simple transformation; one merely subtracts off the LSR's rotational velocity $\Theta_{LSR} = 220$ km/s along the line of sight as shown in equation (7.12). Once the radial velocities are in the GSR frame, we were able to begin analyzing the kinematics of the RRL stars.

$$V_{GSR} = V_{LSR} + \Theta_{LSR} \cos b \sin l \tag{7.12}$$

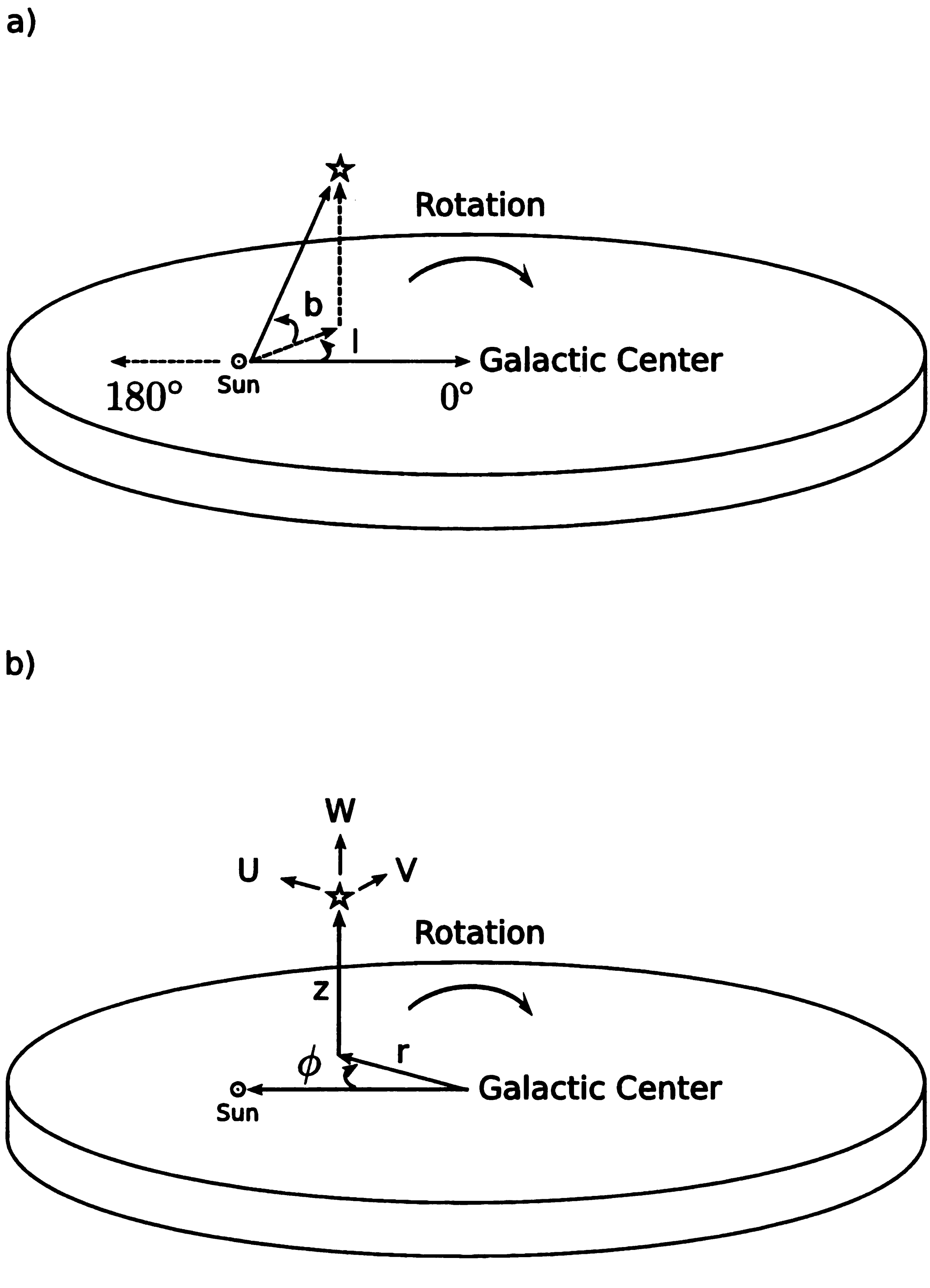

Figure 7.5 Frame a) shows the galactic coordinate system describing l and b. Frame b) shows the cylindrical coordinate system with the U, V, and W space vectors.

Chapter 8: Tracing the Halo

Having created a catalog of RRL stars with photometric and kinematic quantities we were then able to begin looking for signs of different populations in the Halo. There were three different methods used to separate out the populations: photometric properties, kinematic properties and metallicity groups. Each of these methods have their benefits and weaknesses, but together they should provide a clear picture of the halo. Each of these will be taken in turn in the following sections.

8.1 Photometric Properties

8.1.1 Spacial Distribution

One of the benefits of looking at the spacial distribution of the RRL stars was that we were able to use all 421 stars. This is especially useful when one has just an equatorial strip of sky because that allows us to only worry about the RA component of the location. One issue that can affect the interpretation of a spacial distribution map is the change in extinction as a function of RA. The extinction is plotted in Figure 8.1 and comes from the reddening maps of Schlegel et al. (1998). It is worth noting that there is as much as 0.5 magnitudes worth of extinction in the g band, which could cut down on the detection of low amplitude RRL in the most distant parts of the diagram at those RAs.

The map of all 421 RRL stars is shown in Figure 8.2. It is clear that the dis-

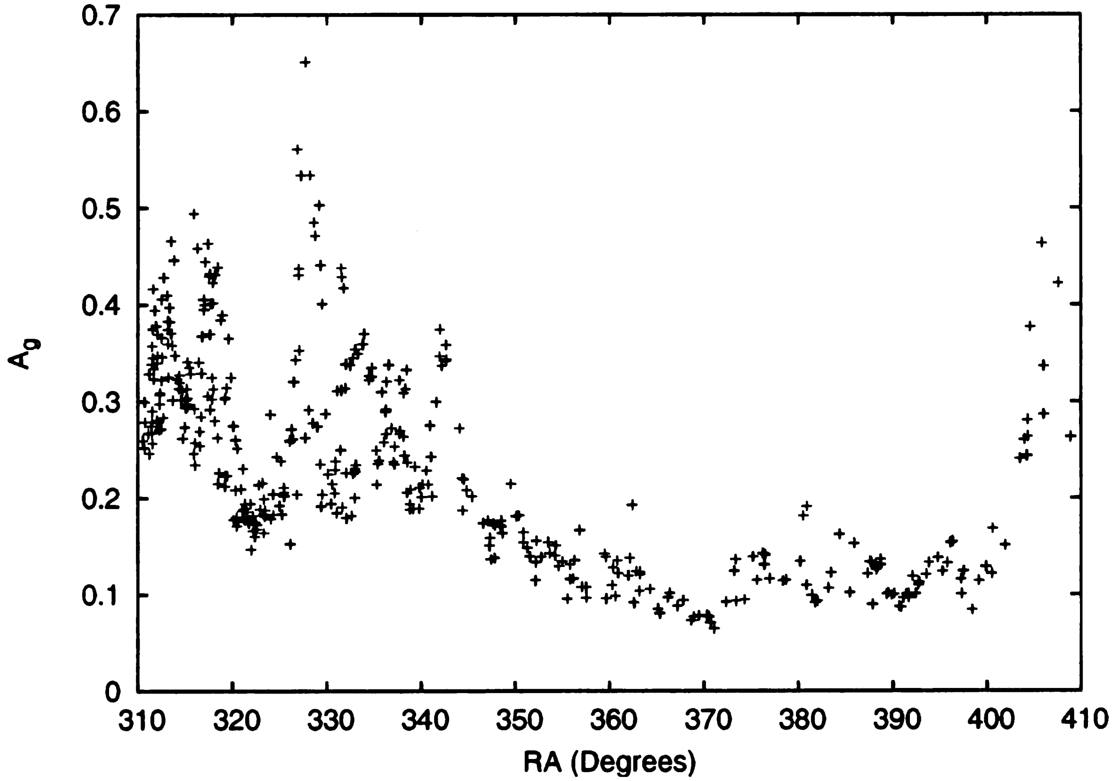

Figure 8.1 An extinction map of the SDSS-II SN stripe as a function of RA. The RAs between 0° and 60° have an additional 360° added to make a more continuous graph. It is clear that there is up to 0.5 magnitudes of extinction at the ends of the stripe 82.

tribution of stars is not uniform, but it is not immediately obvious whether that is due to stellar streams or just to the observational bias of the sample. What is clear is that there is a deficiency in the number of stars at large distances at the edges of the stripe, and this is to be expected given Figure 8.1. In order to be able to make a more precise statement about the existence or non-existence of stellar streams in this sample, we intend to use the methods outlined in Vivas & Zinn (2006). However, this is beyond the scope of this work and we will return to it in a later paper.

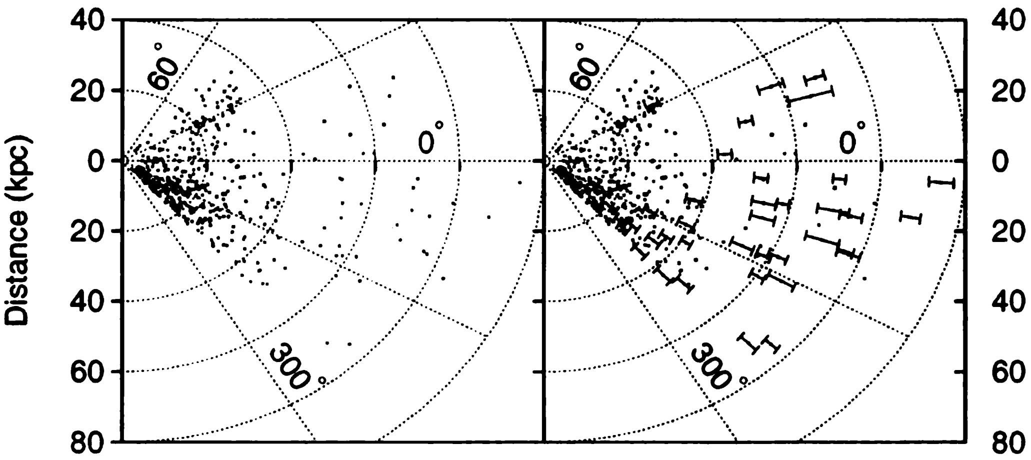

Figure 8.2 Shows the spacial location of the all 421 RRL stars in this survey as a function of RA. The both maps are identical except that the map on the right has the distance error bars included.

8.1.2 Oosterhoff Properties

One of the many benefits of having used RRL stars as tracers of halo populations was that we could take advantage of the Oosterhoff classification as a way of separating stellar components. As discussed in Section 3.6, Lee & Carney (1999) believed that OoII type clusters were associated with an inner halo and that OoI type clusters were associated with an outer accreted halo. In our case, we did not have globular clusters to work with, so we needed another way to distinguish between OoI and OoII RRL stars. One method uses a parameter called $\Delta \log P$ which applies only to RRab stars and is defined in equation (8.1).

$$\Delta \log P = \log P_{obs} - \log P(\text{OoI P-A relation}) \tag{8.1}$$

This equation uses the OoI period-amplitude line from Clement & Rowe (2000) shown in Figure 5.6 and described in equation 5.8. The amplitude of the RRab star is put into this relation and the resulting log period was subtracted from the observed log period. The result is shown in Figure 8.3. In Figure 8.3a, the OoI and OoII populations are clearly visible with the OoI peaking at 0 by definition and the OoII peaking at $\Delta \log P$ of 0.061. This is at a somewhat lower than the 0.075 that the LONEOS survey found (Miceli et al., 2008), but it is very possible that this difference can be explained through binning and the fact that we are using a different filter. Also, our OoII peak is not as well defined, which puts our plot as an intermediate one between the QUEST-I plot where only a tail is visible and LONEOS with it's well defined peak.

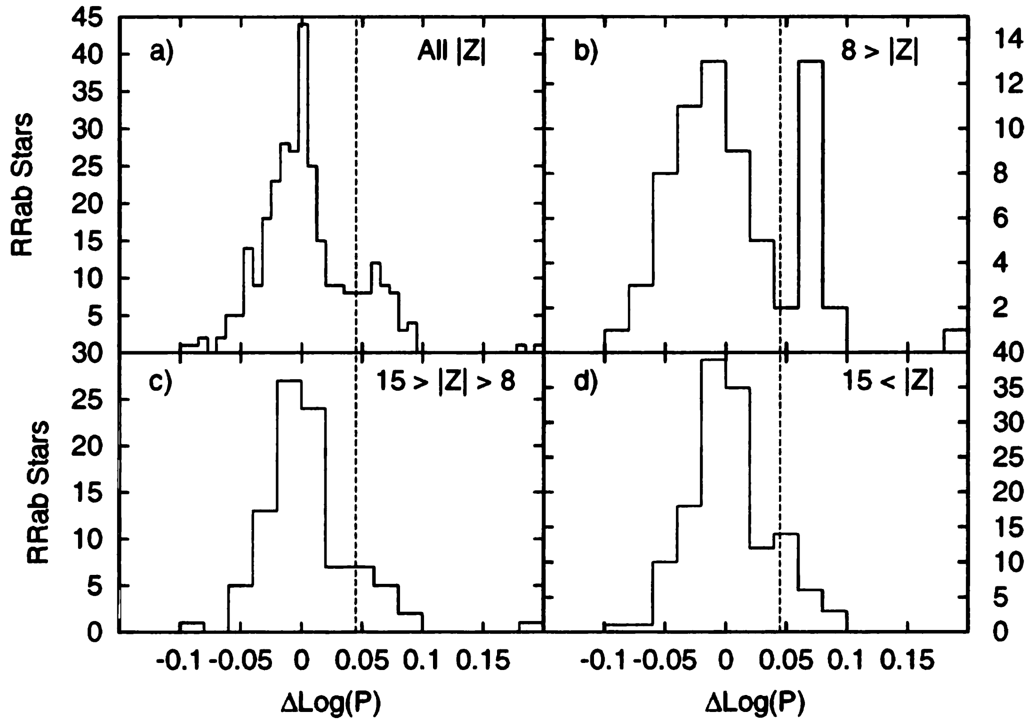

Figure 8.3 These four plots show $\Delta \log P$ as a function of $|Z|$ below the plane. The dashed line shows the cut between OoI and OoII types and is located at 0.045.

One way to look at the different components of the halo is to look at stellar properties as a function of distance away from the plane of the disk. In general, one would like to use $|Z_{max}|$ the maximum distance away from the plane that a star reaches in its orbit. This is a strong selection parameter because it separates out not just different components of the halo, but also removes mixing in the sample between the thick disk stars and halo stars. Thick disk stars stay confined to the thick disk and thus have a smaller $|Z_{max}|$ than halo stars. If there are two components to the stellar halo, then they would also separate out to some degree in Z_{max}. We do not have good proper motions for the RRL stars in this survey, so we cannot get full orbital solutions for them. This means that we cannot determine $|Z_{max}|$, but we can get a relatively good proxy for it $|Z|$. Stars spend most of their time near the maximum of their orbit, so the current distance $|Z|$ away from the plane is correlated with Z_{max}; although this will introduce some scatter into our samples because there will be halo stars away from their maximum with low $|Z|$.

Figures 8.3 b, c and d show how the distributions of $\Delta \log P$ change as a function of $|Z|$. Clearly the OoII population is strongest near the plane of the galaxy, and drops off significantly at higher $|Z|$. That being said, it is unclear whether the OoII component disappears completely, because it is not known whether the distribution of $\Delta \log P$ should be Gaussian. It may very well not be Gaussian.

When Suntzeff et al. (1991) plotted $\Delta \log P$ versus [Fe/H] they saw a gap between the OoI stars and the OoII stars. This would be the expectation at first pass because the Milky Way globulars show a separation in mean RRab period as discussed in Section 3.5. They determined their metallicities using the ΔS method. Later Kinemuchi et al. (2006) found that their version of the plot had no clear separation, although in their case they did not have spectroscopy and were instead using the Jurcsik & Kovacs (1996) method to obtain metal abundances. As can be seen in Figure 8.4a, we also see very little separation, but there are definitely two main groups in our sample of RRab. To check and make sure that this is not due to the Jurcsik & Kovacs (1996) method, Figure 8.4b uses only RRab with SDSS spectra, and still there appears to be only a thinning out of stars near where the gap should be, although it is possible that the gap is being lost due to our error bars.

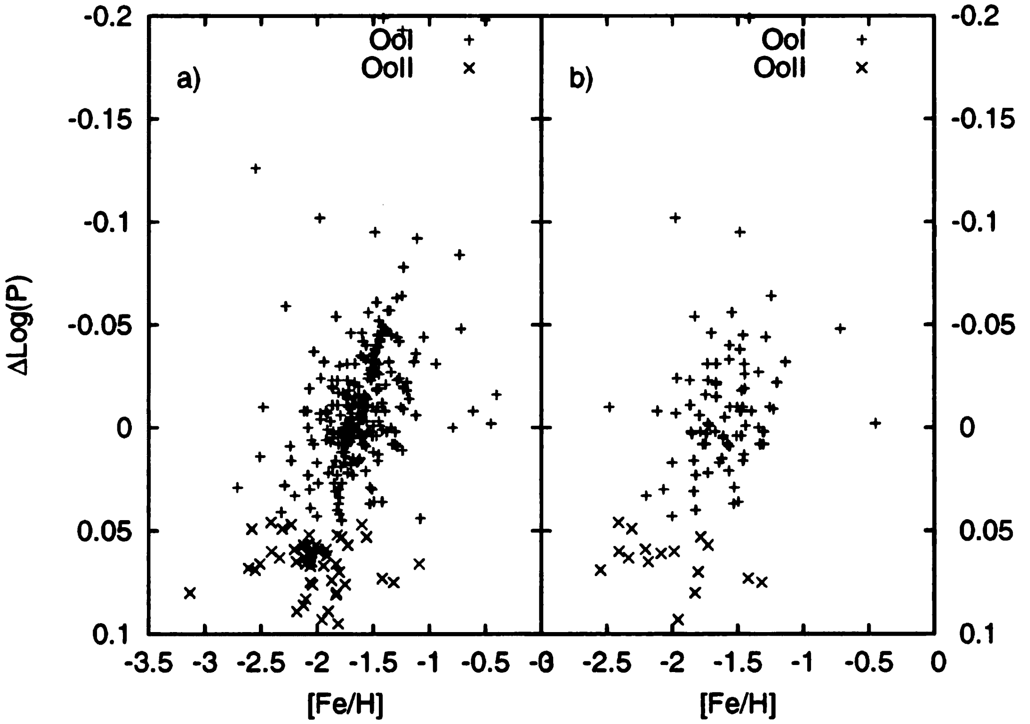

Figure 8.4 These two plots show the relationship between $\Delta \log P$ and [Fe/H] and are similar to plots in Suntzeff et al. (1991) and Kinemuchi et al. (2006). Plot a) shows all the RRab, and plot b) is limited to just RRab with SDSS spectra (Groups (A) and (C)).

8.2 Kinematic Properties

8.2.1 Radial Velocities

Clearly Figure 8.3 is suggestive that there are different populations of stars at different heights below the plane. One way of looking for those different populations is by looking at the radial velocities. As discussed in Section 2.3, in the dual halo model of the galaxy described by Carollo et al. (2007), the inner halo has a small prograde rotational velocity in the cylindrical coordinate, V_ϕ and the outer halo has a net retrograde motion. Unfortunately, we would need good proper motions for our RRL to derive V_ϕ, so we have to instead use a proxy parameter. Although it is not immediately obvious, the radial velocity in the galactic center of rest, V_{gsr} actually tracks V_{ϕ} relatively well. For more on this, see Section 8.2.2.

One of the other issues we must be aware of is that their is a mixing in our sample between the thick disk stars and halo stars. This means that for our lowest $|Z|$ bin there is a component to V_{gsr} that is coming from stars moving at the LSR velocity of 220 km/s. For the rest of the $|Z|$ cuts, it is not a significant issue.

In Figure 8.5, we see the distribution of radial velocities with progressive cuts in $|Z|$. Figure 8.5a shows a very broad distribution of velocities ranging from -300 to 300 km/s. As we progress through plots b and c in Figure 8.5, it is clear that the entire distribution shifts from more positive to more negative as one goes higher in $|Z|$. Ultimately in 8.5d, there appears to be two separate velocity populations. To help quantify this shift, the parameters of the Gaussian fits are shown in Table 8.1. This is what would be expected in a dual halo scenario, because as one progress outward in $|Z|$ the dominance of the inner halo over the velocity distribution should slowly be replaced by the outer halo.

Table 8.1: Parameters for Gaussian Fits to Radial Velocity Populations

$\lvert Z\rvert$	N Gauss	Type	Amp	Amp_{Err}	Mean	$Mean_{Err}$	σ	σ_{Err}
All	1	Data	15.5	1.0	-4.62	10.3	138	11
$\lvert Z\rvert < 8$	1	Data	10.5	1.2	61.5	16.8	131	17
$15 > \lvert Z\rvert > 8$	1	Data	8.82	0.57	16.0	9.4	126	10
$15 < \lvert Z\rvert$(Blue)	2	Data	14.1	0.9	-115	3	42.6	3.2
$15 < \lvert Z\rvert$(Black)	2	Data	8.55	0.98	41.9	4.6	33.6	4.7

Due to the dependence of the relationship between V_{gsr} and V_{phi}, we applied a distance, D < 30 kpc cut to Figure 8.6 and the corresponding Table 8.2. This

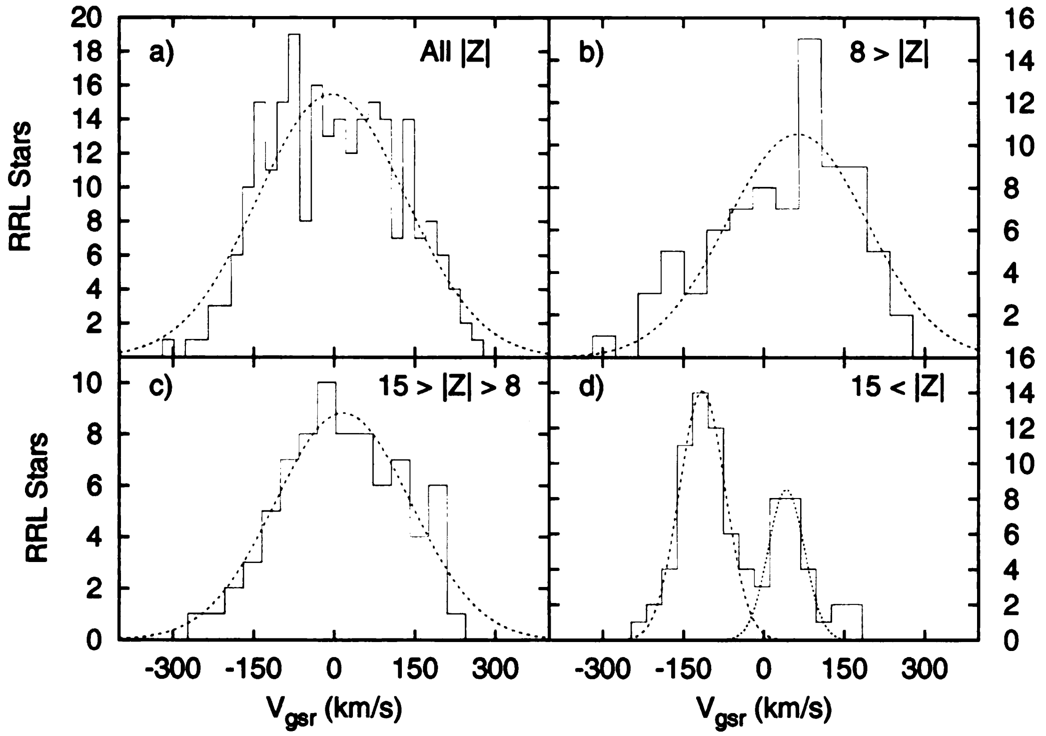

Figure 8.5 These four plots show the radial velocity in the gsr frame for the RRL stars as a function of $|Z|$ below the plane. Each plot has a Gaussian fit to it, with plot d) using a combination of two Gaussians.

significantly reduces the star counts, but the overall shape of the graphs remain the same, suggesting that the distance cut is not affecting our overall results. In particular, Figure 8.6d still maintains the dual populations although the star counts suffer the greatest loss in this $|Z|$ bin.

Table 8.2: Parameters for Gaussian Fits to Radial Velocity Populations with D < 30 kpc

$\|Z\|$	N Gauss	Type	Amp	Amp_{Err}	Mean	$Mean_{Err}$	σ	σ_{Err}
All	1	Data	13.8	1.0	10.2	11.8	139	12
All	1	Model	43.3	3.1	83.1	10.1	121	10.8
$\|Z\| < 8$	1	Data	10.5	1.2	61.5	16.7	131	17
$\|Z\| < 8$	1	Model	80.1	7.7	134	7.8	70.2	7.8

Table 8.2: Gaussian Parameters to V_{gsr} Fits with D < 30 kpc (continued)

$\|Z\|$	N Gauss	Type	Amp	Amp_{Err}	Mean	$Mean_{Err}$	σ	σ_{Err}
$15 > \|Z\| > 8$	1	Model	18.9	1.2	-0.6	7.7	103	8
$15 > \|Z\| > 8$	1	Data	8.72	0.57	18.6	9.5	126	10
$15 < \|Z\|$(Blue)	2	Data	9.47	1.58	-120	6.7	31.6	6.8
$15 < \|Z\|$(Black)	2	Data	4.13	1.0	33.1	24.9	70.7	28.9
$15 < \|Z\|$	2	Model	NA	NA	NA	NA	NA	NA
$15 < \|Z\|$	1	Model	10.9	1.1	11.7	11.9	106	13

8.2.2 A Question of Bias

One of the first questions that must be dealt with in the context of radial velocities is whether we are seeing a bias due to the sampling methods. In the case of this survey, there is even more doubt than usual in that regard because we are looking at a very narrow stripe that cuts through a wide range of galactic latitude. One way to examine this issue is to look at a model version of our galaxy. The Besçanon model galaxy from Robin et al. (2003) provides an excellent way to test our observations. The Besçanon model uses a single kinematically consistent halo, so any effects in velocity space seen in both our observed and the model histograms are likely to be due to observational bias. The corollary to that is that anything that is different may tell us something about the nature of the halo.

The Besçanon model is available at *http://bison.obs-besancon.fr/modele/* and the parameters used to generate the model that we used can be found in Appendix A.2. A few of the most pertinent constraints are that we only used giant stars between A0 and F9 with M_V between 0 and 1 to select out only horizontal branch stars. The model was submitted in two parts, the first going from RA of 300° to 360° and the

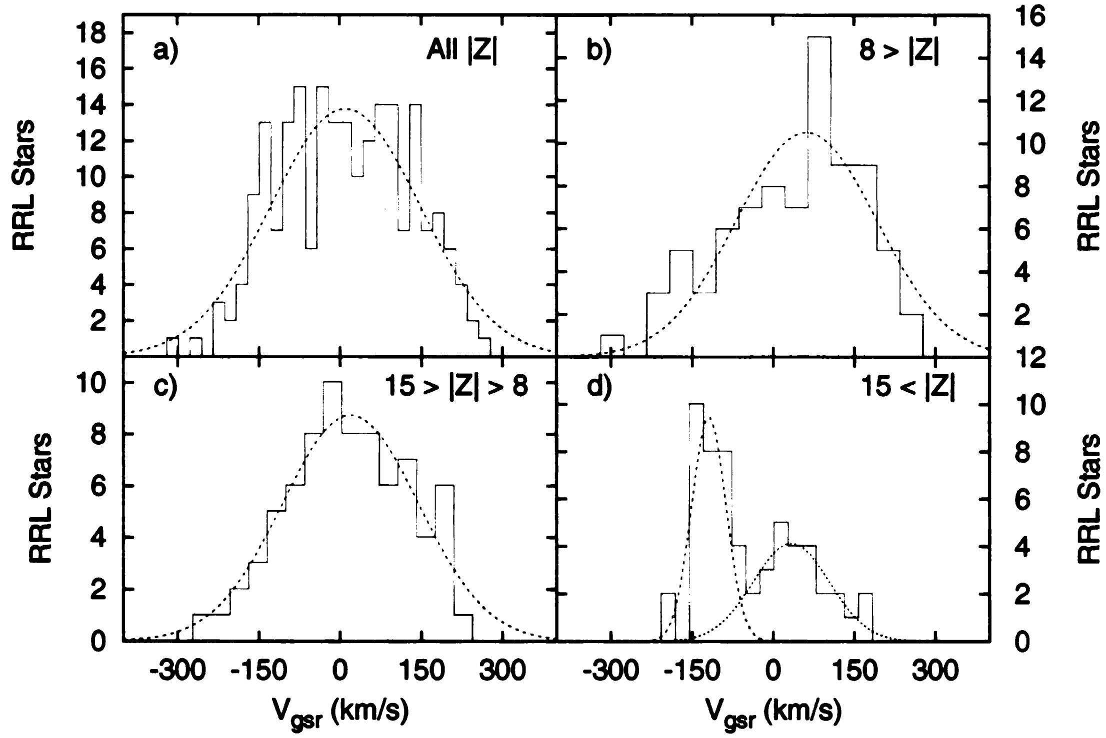

Figure 8.6 These four plots show the radial velocity in the gsr frame for the RRL stars as a function of $|Z|$ below the plane. Each plot has a Gaussian fit to it, with plot d) using a combination of two Gaussians. All of these velocities are for stars with a D < 30 kpc.

second from a RA of 0° to 60° in steps of 5°. The Dec for both parts ran from $-1.25°$ to 1.25° in steps of 1.25°. Once the model was created it was cut down so that only stars with a distance between 3.9 kpc and 52.4 kpc were used, keeping the models consistent with our observations.

The first test of our methods is to check the use of V_{gsr} as a velocity parameter. The Besçanon model gives us a perfect test bed for determining this because it provides us with the velocities U, V, and W, which allow us to generate V_ϕ. In Figure 8.7, the relationship between V_{gsr} and V_ϕ is explored. It is clear from Figure 8.7 that the relationship between V_ϕ and V_{gsr} is basically one to one, although there is significant scatter. The scatter increases with increasing distance, which makes sense because one has less of a lever arm on the projection of the transverse motion as one gets farther out. For the purposes of this analysis, 30 kpc appears to be the best compromise between scatter in the relation and star counts. The relation is centered near 0 in both V_ϕ and V_{gsr}, so it is unlikely to have much bearing on the mean of our velocity distributions, although the scatter in this relation will add to the standard deviation of our distributions.

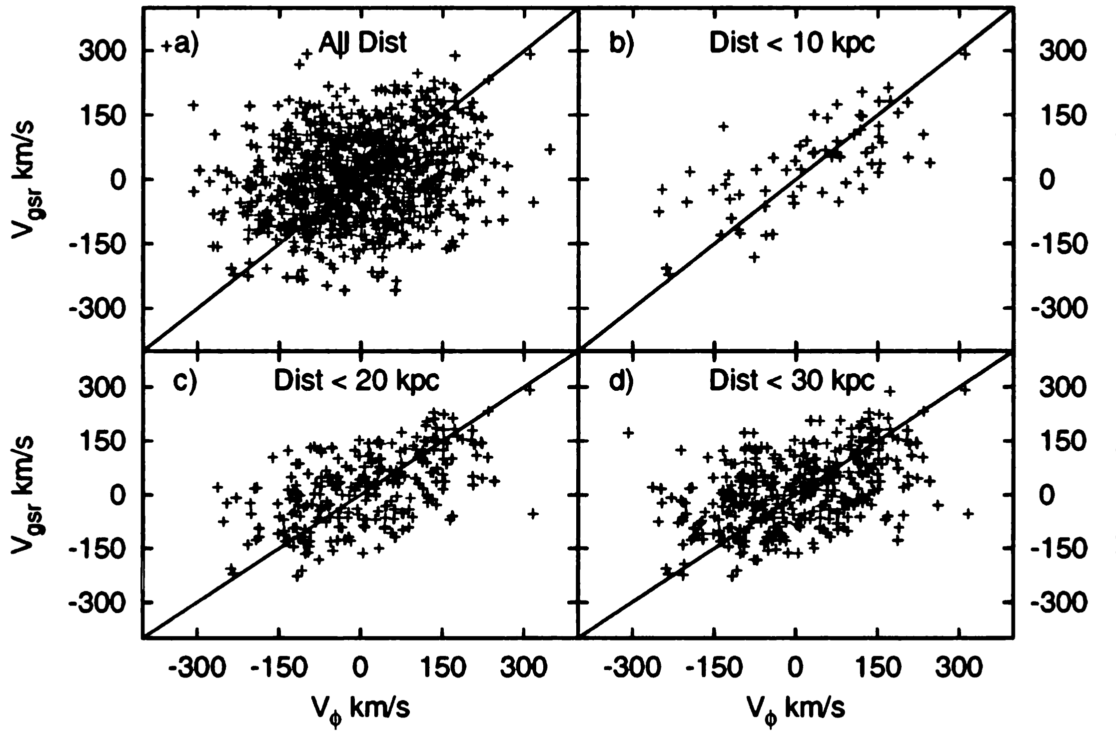

Figure 8.7 These four plots show the relationship between V_{gsr} and V_ϕ in the model galaxy. It is clear that the linear relationship becomes less clear as distance increases. The line is the unity line.

It is now possible to test our observed velocities versus the model of the single halo. The model data was processed in the exact same way as the observed data and the resulting histograms are shown in Figure 8.8. The Gaussian fits to the model data use the exact same starting values and the results are shown in Table 8.2. Qualitatively the Figures 8.6b,c and 8.8b,c appear to be very similar, which is to be expected, since they should be primarily representative of the inner halo. Figures 8.6d and 8.8d, on the other hand appear to be quite different, with 8.6d appearing to be two separate populations, where 8.8d is clearly one distribution, so much so that the second Gaussian would not converge. The Table 8.2 also contains the single Gaussian fit for 8.8d.

One way to test the likelihood that these are similar graphs is to use the Kolmogorov-Smirnov test (KS-test). This statistical test is nice because it is relatively insensitive to the underlying distribution that one is trying to look at, but it is not as sensitive to differences as tests that assume a Gaussian. The null hypothesis, that both the data and the model come from the same distribution, was the object of this test. To test this, the model and observational data were compared to each other using KS-test. The results of this are shown in Table 8.3. The D_{KS} is the maximum difference between the distributions in the cumulative distribution plot and P_{KS} is the probability that the hypothesis is true with 0 being 0% and 1 being 100%. The table strongly suggests that in the farthest $|Z|$ bin the observations are not compatible with the null hypothesis. It is also interesting that the nearest $|Z|$ bin is also incompatible, owing to the large positive V_{gsr} peak in the model. This will be explored more thoroughly in the next section. The central bin is reasonably compatible, as would be expected, since it is far from the plane of the galaxy and it should still sample the inner halo strongly in the dual halo model.

Table 8.3: The Results of the KS-Test of the Null Hypothesis

$\|Z\|$	D_{KS} D < 30 kpc	P_{KS} D < 30 kpc	D_{KS}	P_{KS}
All	0.2168	0.000	0.1808	0.000
$\|Z\| < 8$	0.2534	0.000	0.2534	0.000
$15 > \|Z\| > 8$	0.1215	0.435	0.1102	0.518
$15 < \|Z\|$	0.2175	0.026	0.3371	0.000

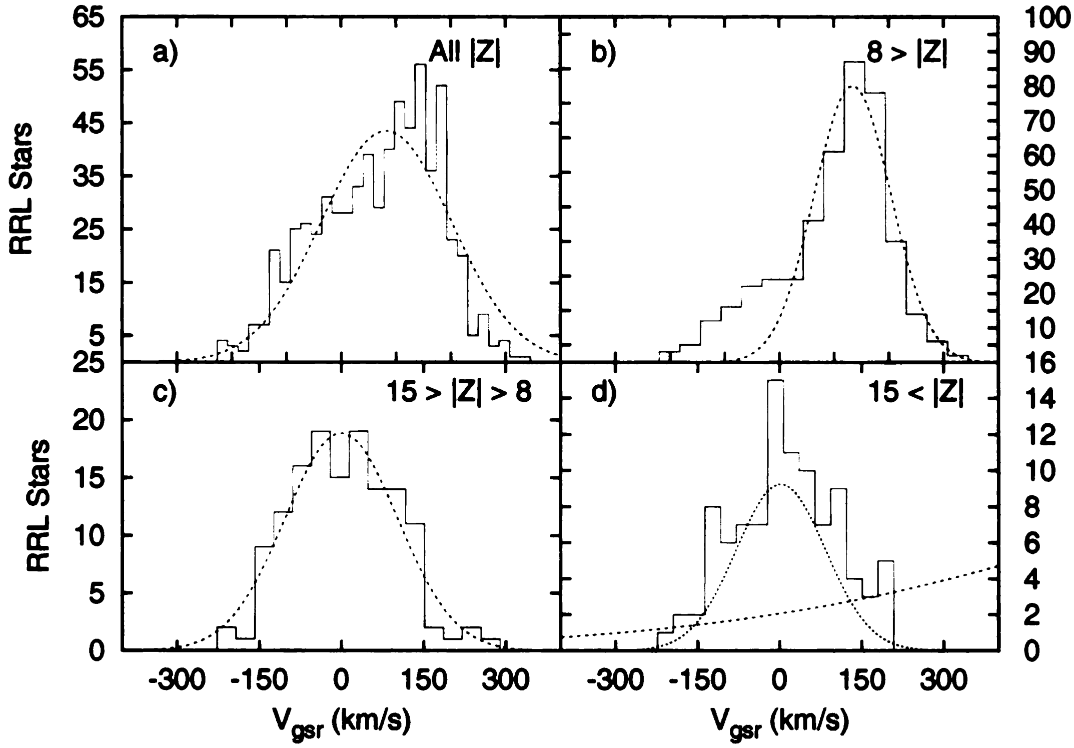

Figure 8.8 These four plots show the radial velocity in the gsr frame for the model horizontal branch stars as a function of $|Z|$ below the plane. Each plot has a Gaussian fit to it, with plod d) using a combination of two Gaussians, although the fit did not converge. The D < 30 kpc cut was applied.

8.2.3 The Thick Disk

Although the discrepancies between the model galaxy in Figure 8.8 and the data in Figure 8.6 are understandable in the context of the dual halo except for the $|Z|$ ¡ 8 bin shown in the b) panels. This bin should be dominated by the inner halo, and thus look like a single halo model, but there is a large asymmetry on the positive V$_{gsr}$ side in the model which is not reflected in the data. To understand this more difference, it is necessary to look at which populations the model stars are being derived from. In Figure 8.9a, panel b) from Figure 8.8 is redone, but this time the stellar populations that the stars belong to are shown. It is clear that the thick disk is the source of the asymmetry. To test this further, the populations as a function of Z are shown in Figure 8.9b. There is a exchange in the dominant population around Z of -4. Using this as another constraint on this $|Z|$ bin in order to remove the effect of thick disk stars as much as possible, Figures 8.9c,d show the model and the data. Running a KS-test on the two shows an increase of the probability of the null hypothesis to .20. This is still not as high of a P value as is seen in the $15 < |Z| < 8$ bin, but this may be attributed to low numbers of stars and residual thick disk contamination.

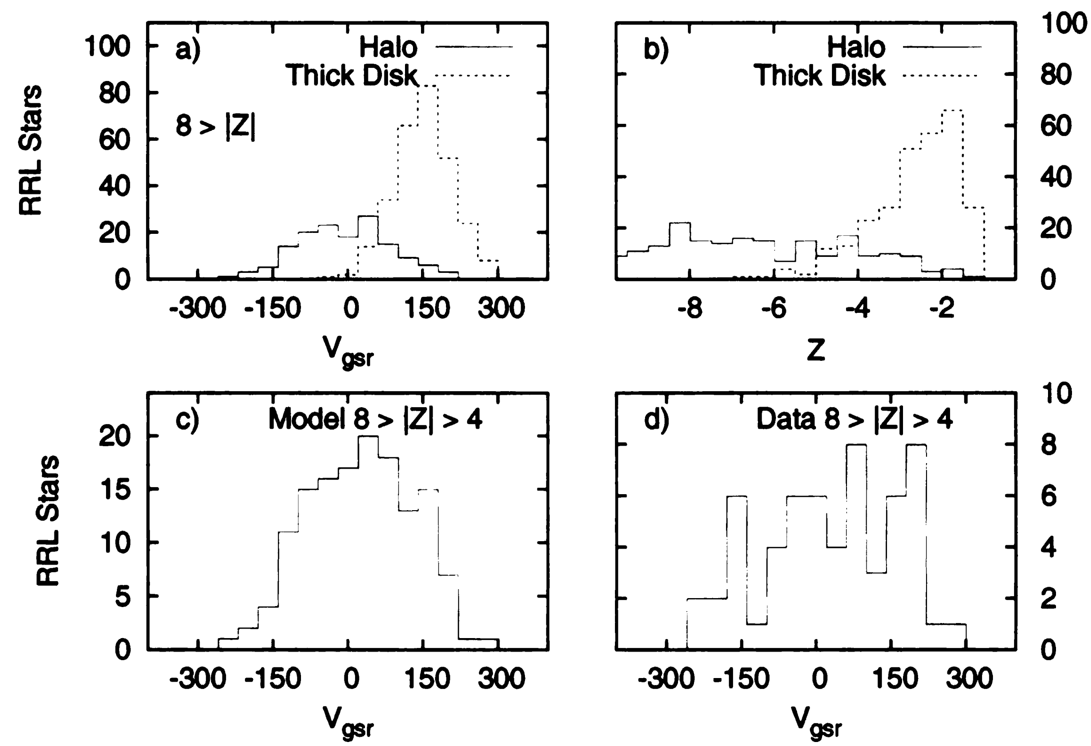

Figure 8.9 These four plots show the analysis of the $|Z| < 8$ bin from Figure 8.8b. Plot a) shows which model population the stars come from. Plot b) shows how the two populations change as a function of Z. Plot c) and d) use a much more narrow range in $|Z|$ than before to try and exclude thick disk stars.

The question that then presents itself is: Why does sampling the thick disk cause disagreement with the model? The model galaxy is supposed to be a model the thick disk as well as the halo, so there should be no disagreement. The most likely cause of the issue is that the model produces non-variable horizontal branch stars, and the data is composed of variable RRL stars. An underlying assumption of this analysis is that the ratio of variable to non-variable stars is fixed. Within a given population this should be roughly true, but there is no guarantee that the ratio will be the same in between populations. In fact, work by Layden (1995a,b) found that there is a difference in the ratios of RRL stars to horizontal branch stars in these two populations. This should not be an unexpected result, since the ratio in each population should be dependent on the horizontal branch morphology of that population, which itself is dependent on properties such as metallicity. Since metallicity clearly differs between the thick disk and the halo, it makes sense that their ratios should be different as well.

8.3 Composition Properties

The final way to analyze the data was by looking at the metallicity distributions. In the dual halo scenario described by Carollo et al. (2007), they saw a relationship between Z_{Max}, and the metallicity distribution of their sample. They saw their sample slowly become more metal poor as they went to higher Z_{max}. In their Figure 3, they used V_ϕ cuts to help exclude the prograde stars, and the stronger their cut in V_ϕ the more pronounced the shift. In our case, we do not have enough stars to make such cuts, but we still see the slow decline of metal rich stars with increasing $|Z|$ as shown in Figure 8.10. We applied a very modest cut of $V_{gsr} < 50$ km/s in Figure 8.11, and the result is a more stark version of Figure 8.10. This especially for the b and c panels, where the missing higher metallicity component is quite noticeable. In the case of panel d in both figures, we do not see the significant shifts to lower metallicities seen in Carollo et al. (2007). This may be due to the metallicity dependence of horizontal branch morphology. In Section 3.5, we discussed how metallicity can affect the shape of the horizontal branch, and it is possible that very metal-rich and metal-poor RRL are missing because the horizontal branches that would generate them do not pass through the instability strip.

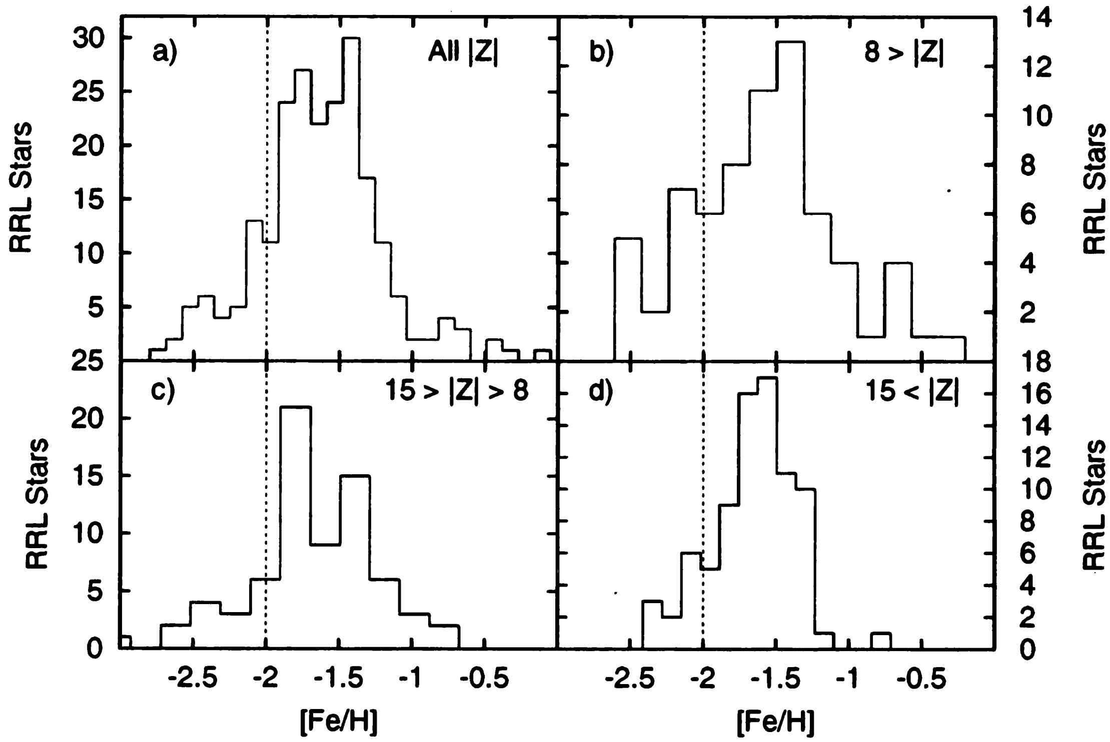

Figure 8.10 These four plots show the metallicity RRL stars as a function of $|Z|$ below the plane. A vertical line is drawn at [Fe/H] = -2.0.

One final way to look at the metallicity distribution of our sample is to cut on velocity. In Figure 2 of Carollo et al. (2007), they plotted the metallicity distribution as a function of the velocity V which is the orbital motion with respect to the lsr. Since we do not have access to the orbital velocities, we again use a proxy parameter, in this case it is a parameter we call V_{220} and is defined as:

$$V_{220} = V_{gsr} - 220$$

This effectively takes our gsr velocity and shifts it so that it is at rest with respect to

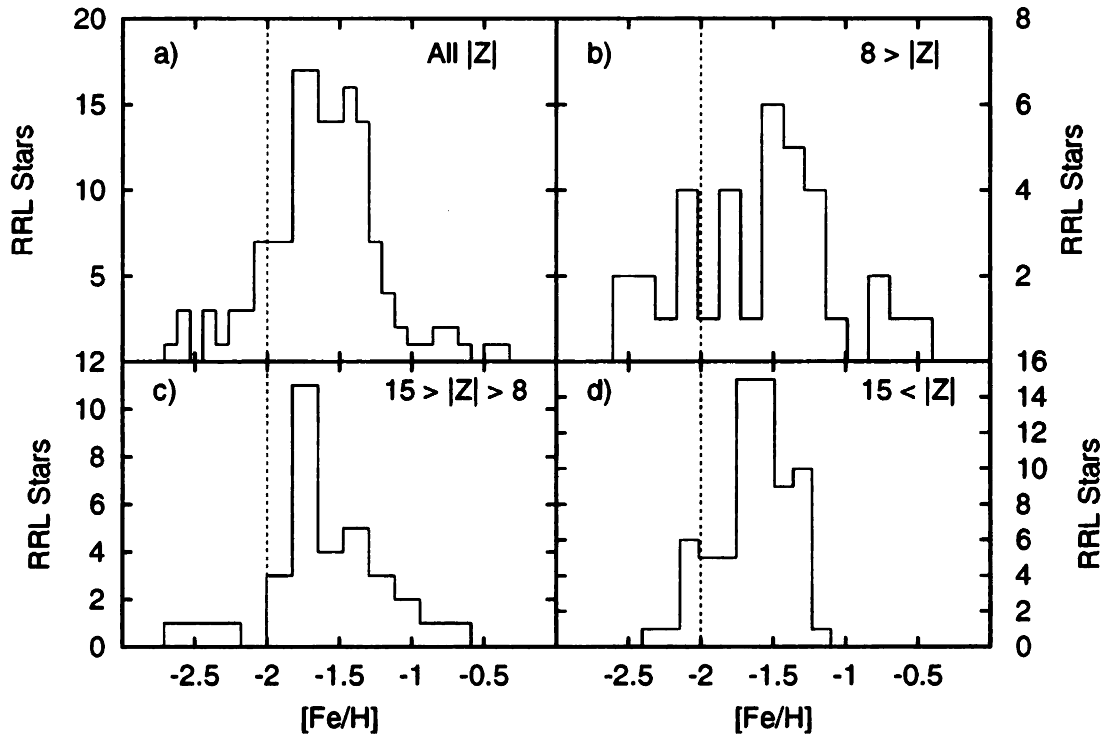

Figure 8.11 These four plots show the metallicity RRL stars as a function of $|Z|$ below the plane. This plot is the same as Figure 8.10 except there is a $V_{gsr} < 50$ km/s cut applied to weed out the prograde stars. A vertical line is drawn at [Fe/H] = -2.0.

the lsr. The resulting graph in shown in Figure 8.12. We see very broad distributions in [Fe/H] in panels a, b, and c, although by the time we get to panel d there is a definite loss of stars on the metal-rich end. Also, the distribution has a longer tail on the metal-poor end. We don't see the complete shifting to lower metallicities a function of V_{220}, but this again may be an issue of horizontal branch morphology.

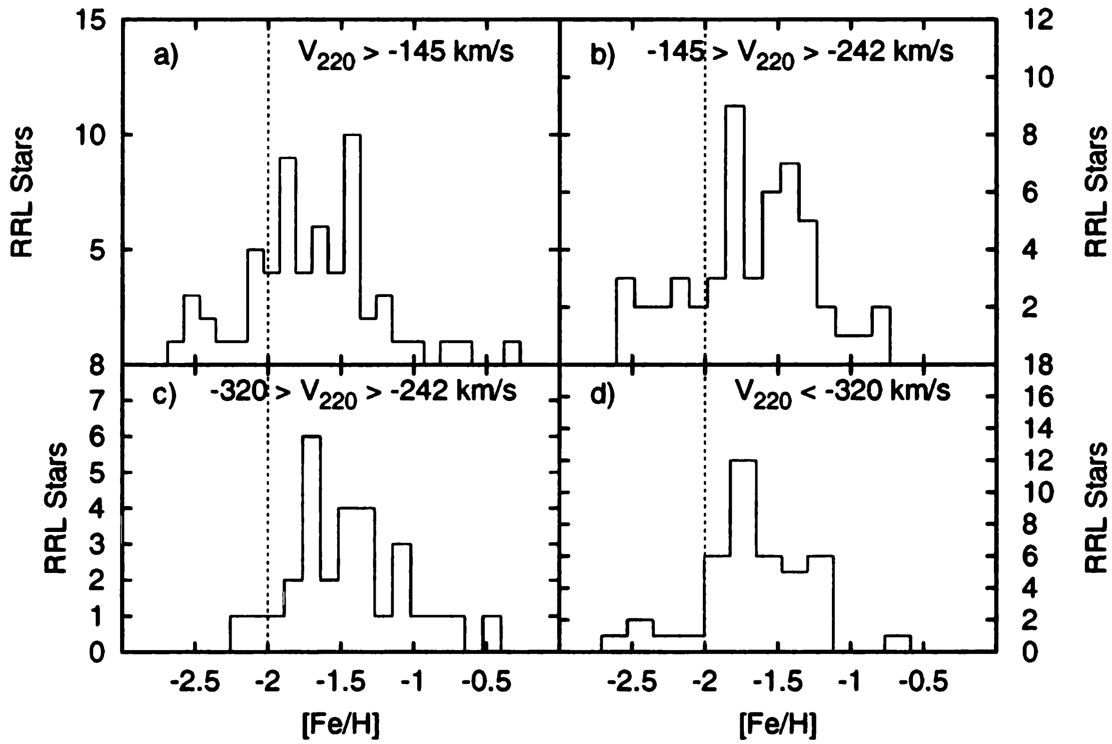

Figure 8.12 These four plots show the metallicity RRL stars as a function of $V_{220} = V_{gsr} - 220$. V_{220} is a proxy for the kinematic quantity V. The normal cut of dist < 30 kpc has been applied. This graph is similar to Carollo et al. (2007) Figure 2.

Chapter 9: Final Analysis and Conclusions

The final catalog produced in this work contains 421 RRL stars of which 305 are RRab and 116 are RRc. Of these, 241 stars have measured radial velocities, and 364 stars have metallicities either from spectroscopy or from the photometric relations defined in Chapter 7. The full catalog ranges in g_0 magnitude from 13 to 20 which covers a distance of 3 to 95 kpc from the sun. Beyond that, each of the 421 RRL stars has full lightcurves in the *ugriz* filters, although coverage varies from star to star and filter to filter, which is a significant step since very few lightcurves exist in this filter set. This is even more important because of the use of the *ugriz* filter system in future large surveys. Using these lightcurves and metallicities, photometric parameters including distance are shown in Table C.2. Using the radial velocities from the 241 RRL stars with spectra, kinematic parameters were derived and can be found in Table C.3. A description of the quantities in both these tables can be found in Table C.1. Finally some example lightcurves can be found in Appendix B.

The Oosterhoff dichotomy provided a powerful tool for looking at different populations. The main strength of using the Oosterhoff groups is that they do not rely on kinematic information to interpret and thus provide an independent method of searching for halo structure. Since the sample of RRL stars comes from the field, the $\Delta \log P$ method was used to determine Oosterhoff type. The RRL clearly separated into the two distinct Oosterhoff groups, and there was a clear dependence on $|Z|$ with OoII being similar in peak height to the OoI RRL in the $|Z|$ bin closest to the plane, with the OoI becoming dominant farther away. This clearly suggests different origins for the RRL at different $|Z|$ heights.

As part of the Oosterhoff study, we also checked to see if the gap in the $\Delta \log P$ versus metallicity plot existed for field RRL as it does for the Milky Way globulars. The plot revealed a definite thinning out near where the gap would be, but it is possible that our errors in metallicity are blurring over the gap itself.

The kinematic information also provided a very interesting look at the halo. That being said, there was also a danger of biases in the sample of RRL due to the way in which the survey cuts across the sky. Primarily the study was limited by the lack of full space velocities, which are difficult to get given that the very accurate proper motions given by the HLC were not sufficient for the RRL stars in this sample. Instead radial velocities had to be used, and although they were corrected to the gsr, they can ultimately only give one dimension of a three dimensional problem. That being said, we were really only interested in the V_{phi} component of the star's velocity and that actually tracks relatively well with V_{gsr} over the survey area. It does add a large amount of scatter to the observations, especially at large distances, but it did not appear to introduce offsets or other peculiarities into the analysis.

This was further compensated for by using the Besçanon model galaxy, which uses a single halo model. By comparing the observations with model data cut in the same way with the same parameters, the differences between the velocity distributions were probably due to the data's deviation from the single halo model. A large asymmetry appeared in the nearest $|Z|$ bin that was not attributable to difference in the halo, but was in fact related to contamination of the sample by thick disk RRL stars. After further analysis it appeared likely that the ratio of variable to non-variable horizontal branch stars varies between the thick disk and the halo. The strongest appearance of the dual halo signature was in the farthest $|Z|$ bin, where the data separated into two distinct velocity groups, while the model remained a single Gaussian. This strongly suggests the need for at least a two-component model for the halo.

The analysis of the metallicity, although not entirely separate from the Oosterhoff analysis, did provide some interesting results. Although the other two analyses found distinct groups, the metallicity analysis did not. The means of metallicity distributions did not change significantly as a function of $|Z|$ nor V_{220}, although there was definite change in the wings of the distribution, with more metal-rich stars vanishing at more distant $|Z|$. Since it was expected from previous work that there would be a relationship between metallicity and the different kinematic groups, this suggests the possibility that RRL stars do not make good tracers in that respect. This may be due to the way in which the horizontal branch is affected by metallicity. If the metallicity of the horizontal branch becomes too metal-rich or too metal-poor, then it will not pass through the instability strip and thus not be seen in this sample.

This work shows how RRL stars can be effectively used to understand the nature of the halo. Furthermore, there is now a catalog of RRL stars that can be used to investigate other areas of study from clumping due to stellar streams to understanding lightcurve morphology in the *ugriz* system. This provides a testbed for techniques that will become important as new surveys come on-line that use the *ugriz* filter system.

APPENDICES

Appendix A: Configuration files

A.1 Example phase.par

```
TYPE HARM BASS KNOT INPU NAME MAXN SUBN SUBP FULL MINP MAXP RATE NMIN FWID FNUM SHOW

2    1    0.0  20   0    1    800  -1   0.0  1    0.1  100  12.0 20   1.0  100  15

----------------------------------------------------------------------------

phase.par: Parameter settings for phase.run. Change values above

----------------------------------------------------------------------------

TYPE:  Type of curve: 1 = trigonometric polynomial

                      2 = supersmoother

                      3 = cubic spline

HARM:  If TYPE=1, The number of harmonics in the trigonometric model

                 Takes values 1,2,3,...

BASS:  If TYPE=2, Bass parameter in supersmoother - range is [0,10]

                 0 recommended.

KNOT:  If TYPE=3, Number of knots in cubic spline - need at least 8.

INPU:  Format of data file:

         0 = Data in three columns

         1 = Kem short data

         2 = MACHO data file

         3 = MACHO .fit file

NAME:  Naming convention for output files:

       1 = Append suffixes like ".per" and ".fit" after the first period

           in the name of the data file. e.g. lcb1.dat -> lcb1.per

       2 = Append suffixes after the end of the data file name.
```

```
        e.g.  var.101 -> var.101.per
MAXN:  Maximum number of observations in data input file
SUBN:  Number of observations in subset: 80-100 recommended
       Set this to be negative if you don't want subsetting
SUBP:  Periods greater than this are fit with the full data,
       periods less than this with the subset data.
FULL:  1 = Refine displayed estimates with full data.
       0 = Do not refine with full data before displaying
MINP:  Minimum period considered:
       Halving this quantity almost doubles run-time
MAXP:  Maximum period considered:
       If <=0, maximum period is length of the data
RATE:  Sampling rate in the initial estimation grid: (6 or more)
       Doubling this quantity almost doubles run-time
NMIN:  Number of intermediate estimates: 10-20 recommended
FWID:  Width of final grids in standard units(1/span): 1-1.5 recommended
         Change at your own risk!
FNUM:  Number of values in each final grid: 100-200 recommended
         Change at your own risk!
SHOW:  Number of period estimates displayed in output
```

A.2 Parameter Files for Besaçon Model

A.2.1 Parameters for Part A

```
Model of stellar population synthesis of the Galaxy
Catalogue simulation with kinematics, Johnson-Cousins photometric system
The resulting parameter file 1203092479.951603.par has been built;
a message will be sent to address when the simulation is complete
new access to the model form:


Summary of the parameters you supplied
A mail will be sent to address: when the simulation is completed
```

```
The name of the file containing the result of the simulation
will be: 1203092479.951603.resu
Field of view:
distance step mode: progressive
large field
coordinate system: equatorial coordinates; equinox: 2000.0
        minimum         maximum         step    number of bins
right ascension:        0       60.00   5.00    12
declination:    -1.25   1.25    1.25    2
solid angle: 149.988096623
Extinction:
diffuse absorption: 0.700 mag/kpc
no discrete clouds


parameter       min     max     step
Absolute V magnitude    0       1       0.50
Spectral type   3       4.9     0.1
Luminosity class        3       3       1.00
Population-age  1       10      1
[Fe/H]  -4.20   1.50    0.30
Distance        0.000000        100.000000      2.00
V app. magnitude        -99.00  99.00   1
B-V     -99.00  99.00   10.00
U-B     -99.00  99.00   10.00
V-I     -99.00  99.00   10.00
V-K     -99.00  99.00   10.00
alpha proper motion     -10.00  10.00   100
delta proper motion     -10.00  10.00   100
Radial velocity         -900.00         900.00  500
u velocity      -500.00         500.00  10.00
v velocity      -500.00         500.00  10.00
w velocity      -500.00         500.00  10.00
Total proper motion     0.00    1000.00         10.00
```

LogTeff 3.00 6.00 0.10

Errors:

error mode:parabolic error = A + B*m + C*m2

photometric errors:

photometric band	A	B	C
V	0.000000	0.000000	0.000000
B	0.000000	0.000000	0.000000
U	0.000000	0.000000	0.000000
R	0.000000	0.000000	0.000000
I	0.000000	0.000000	0.000000
J	0.000000	0.000000	0.000000
H	0.000000	0.000000	0.000000
K	0.000000	0.000000	0.000000
L	0.000000	0.000000	0.000000

proper motion errors:

A	B	C
0.000000	0.000000	0.000000

radial velocity errors:

A	B	C
0.000000	0.000000	0.000000

A.2.2 Parameters for Part B

Model of stellar population synthesis of the Galaxy

Catalogue simulation with kinematics, Johnson-Cousins photometric system

The resulting parameter file 1203094459.295218.par has been built;

a message will be sent to address when the simulation is complete

new access to the model form:

Summary of the parameters you supplied

A mail will be sent to address: when the simulation is completed

The name of the file containing the result of the simulation

will be: 1203094459.295218.resu

Field of view:

distance step mode: progressive

large field

coordinate system: equatorial coordinates; equinox: 2000.0

	minimum	maximum	step	number of bins
right ascension:	300	359.99	5.00	11
declination:	-1.25	1.25	1.25	2

solid angle: 149.963098606

Extinction:

diffuse absorption: 0.700 mag/kpc

no discrete clouds

parameter	min	max	step	
Absolute V magnitude	0	1	0.50	
Spectral type	3	4.9	0.1	
Luminosity class	3	3	1.00	
Population-age	1	10	1	
[Fe/H]	-4.20	1.50	0.30	
Distance	0.000000	100.000000	2.00	
V app. magnitude	-99.00	99.00	1	
B-V	-99.00	99.00	10.00	
U-B	-99.00	99.00	10.00	
V-I	-99.00	99.00	10.00	
V-K	-99.00	99.00	10.00	
alpha proper motion	-10.00	10.00	100	
delta proper motion	-10.00	10.00	100	
Radial velocity	-900.00	900.00	500	
u velocity	-500.00	500.00	10.00	
v velocity	-500.00	500.00	10.00	
w velocity	-500.00	500.00	10.00	
Total proper motion	0.00	1000.00	10.00	
LogTeff	3.00	6.00	0.10	

Errors:

error mode:parabolic error = A + B*m + C*m2

photometric errors:

photometric band	A	B	C
V	0.000000	0.000000	0.000000
B	0.000000	0.000000	0.000000
U	0.000000	0.000000	0.000000
R	0.000000	0.000000	0.000000
I	0.000000	0.000000	0.000000
J	0.000000	0.000000	0.000000
H	0.000000	0.000000	0.000000
K	0.000000	0.000000	0.000000
L	0.000000	0.000000	0.000000

proper motion errors:

A	B	C
0.000000	0.000000	0.000000

radial velocity errors:

A	B	C
0.000000	0.000000	0.000000

Appendix B: Example Lightcurves

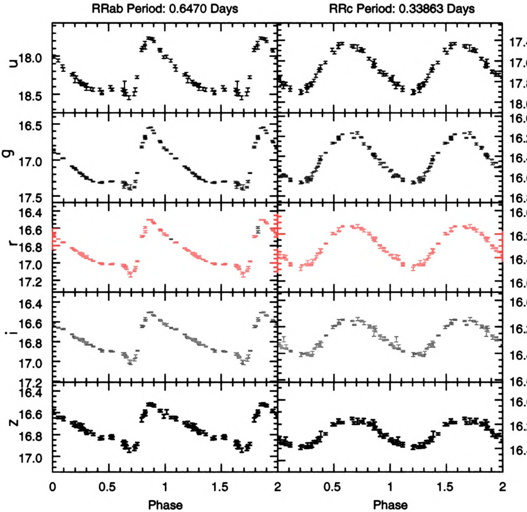

Figure B.1 These are two example lightcurves one RRab and one RRc showing how the lightcurves change with filter.

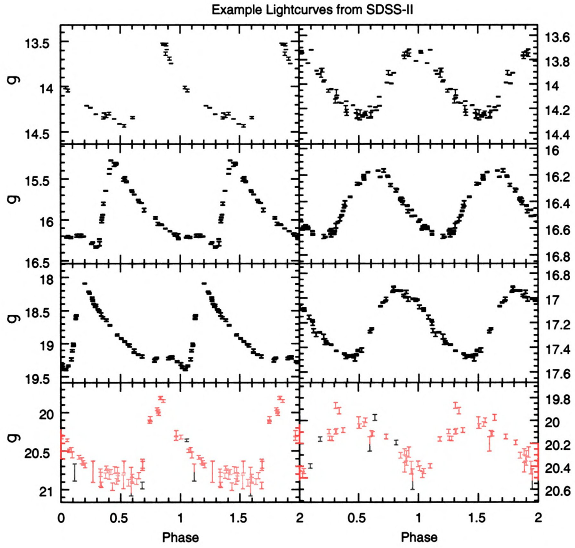

Figure B.2 These are example lightcurves displaying how the lightcurve quality is affected by apparent magnitude, with the brightest RRab and RRc in blue and the top and the dimmest RRab and RRc at the bottom in red.

Appendix C: Data Tables

Table C.1: Description of Parameters in Data Tables

Parameter	Description	Table
Variable	Name of the star in the catalog	C.2, C.3
Type	Bailey type	C.2
P	Period in days	C.2
Amp	g Amplitude in magnitudes	C.2
Max Epoch	The HJD - 2450000 of maximum light	C.2
$< M >$	The magnitude weighted mean magnitude in g	C.2
$< I >$	The intensity weighted mean magnitude in g	C.2
A	The extinction due to dust in g in magnitudes	C.2
$< g0 >$	The dereddened intensity weighted mean	C.2
M	The absolute magnitude in g	C.2
$\Delta \log P$	Described in equation (8.1)	C.2
Oo	Oosterhoff Group (defined only for RRab stars)	C.2
[Fe/H]	Metallicity of the star	C.2
Grp	Metallicity group defined in Table 7.2	C.2
RA	Right Ascension of the star in degrees	C.3
Dec	Declination of the star in degrees	C.3
l	Galactic latitude in degrees	C.3
b	Galactic longitude in degrees	C.3

Table C.1: Parameters in Data Tables (continued)

Parameter	Description	Table
X, Y, Z	Cartesian coordinates from the galactic center	C.3
R	Radius from the galactic center using X and Y only	C.3
helio	Heliocentric radial velocity in km/s	C.3
lsr	Radial velocity in the local standard of rest in km/s	C.3
gsr	Radial velocity in the galactic standard of rest km/s	C.3

Table C.2: Photometric Properties of SDSS RRL

Variable	Type	P	Amp	Max Epoch	$< M >$	$< I >$	A	$< g0 >$	M	$\Delta \log P$	Oo	[Fe/H]	err	Group
1020340	c	0.3397	0.65	3626.4483	18.11	18.09	0.14	17.95	0.482	NA	NA	-2.14	0.11	(F)
1035856	ab	0.6590	0.63	3676.7137	16.32	16.30	0.12	16.18	0.403	0.014	I	-2.51	0.71	(B)
1051362	ab	0.6301	0.49	3676.6294	18.05	18.04	0.13	17.91	0.584	-0.022	I	-1.67	0.06	(A)
1061424	ab	0.4763	1.31	3674.1843	18.30	18.22	0.15	18.07	0.627	-0.045	I	-1.46	0.03	(C)
1068459	abB	0.4931	1.34	3628.4843	18.09	18.01	0.16	17.86	0.630	-0.026	I	-1.45	0.10	(A)
1095893	ab	0.6151	0.89	3676.4907	18.38	18.34	0.12	18.23	0.628	0.016	I	-1.46	0.02	(C)
1097410	ab	0.4859	0.76	3626.2938	16.97	16.94	0.10	16.84	0.517	-0.102	I	-1.98	0.08	(C)
1103721	ab	0.6491	1.04	3676.5396	18.40	18.35	0.12	18.23	0.571	0.057	II	-1.73	0.10	(A)
11194	abB	0.5557	1.10	3685.5358	14.88	14.83	0.13	14.70	0.630	-0.003	I	-1.45	0.48	(B)
1132188	ab	0.5025	1.48	3671.6809	17.75	17.66	0.08	17.57	0.573	-0.001	I	-1.72	0.07	(C)
1152564	ab	0.5336	1.29	3676.3726	18.32	18.25	0.11	18.13	0.662	0.002	I	-1.30	0.05	(C)
1173512	cB	0.3084	0.56	3679.2531	18.34	18.32	0.13	18.20	0.595	NA	NA	-1.61	0.37	(H)
1191801	cB	0.3610	0.47	3626.3214	17.32	17.31	0.12	17.18	0.608	NA	NA	-1.55	0.04	(F)
1194915	cB?	0.4050	0.51	3626.3103	15.18	15.17	0.17	15.00	0.483	NA	NA	-2.14	0.03	(F)
1233272	c	0.2877	0.66	3679.5462	17.81	17.78	0.15	17.63	0.578	NA	NA	-1.69	0.13	(F)
1276299	c	0.3374	0.53	3670.7090	14.00	13.98	0.24	13.74	0.615	NA	NA	-1.52	0.55	(I)

Table C.2: Photometric Properties of SDSS RRL (continued)

Variable	Type	P	Amp	Max Epoch	$< M >$	$< I >$	A	$< g0 >$	M	$\Delta \log P$	Oo	[Fe/H]	err	Group
128618	ab	0.6259	1.20	3638.7808	15.20	15.14	0.11	15.04	0.499	0.061	II	-2.06	0.34	(E)
1289027	ab?	0.6164	0.68	3686.8011	14.37	14.35	0.26	14.09	0.598	-0.008	I	-1.60	0.29	(E)
1295886	ab	0.5194	1.36	3679.3152	18.00	17.92	0.24	17.68	0.576	-0.001	I	-1.70	0.10	(D)
1298010	abB	0.5545	0.82	3626.6969	18.72	18.69	0.28	18.41	0.622	-0.038	I	-1.48	0.05	(A)
1298437	c	0.3094	0.54	3679.5081	17.13	17.11	0.26	16.85	0.615	NA	NA	-1.52	0.55	(I)
1305932	c	0.3589	0.58	3628.2004	18.23	18.21	0.38	17.84	0.538	NA	NA	-1.88	0.18	(F)
1339969	c	0.2140	0.32	3673.4150	14.96	14.96	0.46	14.49	0.615	NA	NA	-1.52	0.55	(I)
1345269	ab	0.6163	0.65	3679.5374	18.47	18.45	0.34	18.12	0.636	-0.012	I	-1.42	0.14	(D)
1345335	c	0.3661	0.65	3679.3459	17.34	17.31	0.29	17.02	0.507	NA	NA	-2.02	0.01	(H)
1390757	abB	0.5704	0.58	3676.2506	15.99	15.97	0.42	15.55	0.548	-0.054	I	-1.83	0.10	(C)
1428224	ab	0.6237	1.21	3616.1355	17.98	17.91	0.26	17.65	0.515	0.060	II	-1.99	0.06	(C)
1448542	c	0.3579	0.27	3656.1352	15.71	15.70	0.26	15.44	0.809	NA	NA	-0.61	0.43	(G)
1465359	ab	0.5619	0.95	3705.1685	17.76	17.72	0.25	17.47	0.602	-0.016	I	-1.58	0.36	(E)
1469597	ab	0.5695	1.22	3664.8895	16.16	16.10	0.30	15.80	0.533	0.022	I	-1.90	0.57	(B)
1471053	ab	0.6062	1.22	3668.5299	16.71	16.65	0.28	16.37	0.388	0.049	II	-2.58	0.72	(B)
1507160	c	0.3564	0.70	3705.0563	19.09	19.06	0.27	18.79	0.615	NA	NA	-1.52	0.55	(I)

Table C.2: Photometric Properties of SDSS RRL (continued)

Variable	Type	P	Amp	Max Epoch	$< M >$	$< I >$	A	$< g0 >$	M	$\Delta \log P$	Oo	[Fe/H]	err	Group
1515202	c	0.3756	0.49	3705.1867	17.52	17.51	0.33	17.18	0.615	NA	NA	-1.52	0.55	(I)
1517082	ab	0.4803	1.32	3705.1842	16.46	16.39	0.25	16.14	0.625	-0.040	I	-1.47	0.45	(B)
153071	ab	0.4658	1.57	3628.4719	15.31	15.20	0.09	15.12	0.664	-0.023	I	-1.29	0.29	(D)
1537496	ab	0.6430	0.43	3665.2911	16.43	16.42	0.27	16.14	0.540	-0.020	I	-1.87	0.57	(B)
1541097	c?	0.2992	0.20	3697.2296	16.06	16.05	0.34	15.72	0.615	NA	NA	-1.52	0.55	(I)
1541709	ab	0.5772	1.22	3664.7304	19.10	19.04	0.28	18.76	0.450	0.028	I	-2.29	0.16	(D)
1544422	ab	0.6218	0.63	3665.4688	18.51	18.49	0.36	18.13	0.578	-0.011	I	-1.69	0.16	(D)
1544490	ab	0.4771	1.54	3668.1880	17.20	17.10	0.27	16.84	0.553	-0.017	I	-1.81	0.55	(B)
1546260	abB	0.5821	1.09	3665.4106	17.32	17.27	0.29	16.98	0.591	0.016	I	-1.63	0.52	(B)
1548226	c	0.4043	0.52	3700.1098	18.69	18.67	0.37	18.30	0.615	NA	NA	-1.52	0.55	(I)
1549042	c	0.2418	0.15	3697.0344	15.24	15.24	0.26	14.98	0.976	NA	NA	0.17	0.43	(G)
1551422	c	0.3250	0.60	3665.0089	17.77	17.74	0.35	17.40	0.615	NA	NA	-1.52	0.55	(I)
1552749	c	0.2758	0.26	3665.1889	16.66	16.66	0.42	16.24	0.615	NA	NA	-1.52	0.55	(I)
1560708	c	0.3334	0.20	3697.0550	16.60	16.60	0.33	16.26	0.615	NA	NA	-1.52	0.55	(I)
1561207	ab	0.6076	1.42	3665.0525	16.29	16.20	0.32	15.88	0.540	0.074	II	-1.87	0.14	(D)
1570547	ab	0.5086	1.09	3699.8413	15.59	15.53	0.39	15.14	0.668	-0.042	I	-1.27	1.30	(D)

Table C.2: Photometric Properties of SDSS RRL (continued)

Variable	Type	P	Amp	Max Epoch	$< M >$	$< I >$	A	$< g0 >$	M	$\Delta \log P$	Oo	[Fe/H]	err	Group
1582235	c	0.3195	0.29	3697.0139	15.44	15.43	0.38	15.05	0.615	NA	NA	-1.52	0.55	(I)
1593356	ab	0.5851	1.47	3697.0214	15.85	15.76	0.34	15.42	0.441	0.063	II	-2.33	0.09	(A)
1593719	c	0.3349	0.50	3665.1451	17.29	17.28	0.28	17.00	0.615	NA	NA	-1.52	0.55	(I)
1599072	ab	0.4700	1.58	3656.0521	16.58	16.48	0.37	16.11	0.677	-0.019	I	-1.23	0.44	(B)
1599155	c	0.4188	0.52	3697.3737	15.35	15.33	0.35	14.99	0.615	NA	NA	-1.52	0.55	(I)
1600177	ab	0.6367	1.08	3697.5004	17.41	17.37	0.28	17.09	0.606	0.053	II	-1.56	0.51	(B)
160083	c	0.3523	0.53	3685.2455	17.41	17.39	0.08	17.31	0.615	NA	NA	-1.52	0.55	(I)
1616233	ab	0.5511	1.30	3665.1330	18.04	17.97	0.27	17.70	0.563	0.017	I	-1.76	0.12	(D)
1617275	ab	0.6650	0.86	3699.9074	15.43	15.40	0.31	15.09	0.598	0.047	II	-1.60	0.52	(B)
1617477	abB	0.4762	1.04	3697.0796	17.20	17.15	0.30	16.86	0.677	-0.078	I	-1.23	0.44	(E)
1621547	c	0.3084	0.32	3700.2851	17.12	17.11	0.31	16.80	0.615	NA	NA	-1.52	0.55	(I)
1630498	abB	0.4871	1.31	3696.8476	16.47	16.40	0.27	16.13	0.617	-0.035	I	-1.51	0.46	(E)
1632111	ab	0.6278	0.98	3700.1622	18.49	18.45	0.32	18.13	0.620	0.036	I	-1.50	0.09	(A)
1632460	ab	0.4774	1.38	3665.1230	17.20	17.11	0.41	16.70	0.700	-0.036	I	-1.12	0.49	(B)
1634539	ab	0.5497	1.17	3699.8827	17.69	17.62	0.37	17.26	0.576	0.000	I	-1.70	0.39	(E)
1637388	c	0.3401	0.51	3665.0782	15.49	15.48	0.35	15.13	0.654	NA	NA	-1.34	0.02	(F)

Table C.2: Photometric Properties of SDSS RRL (continued)

Variable	Type	P	Amp	Max Epoch	$< M >$	$< I >$	A	$< g0 >$	M	$\Delta \log P$	Oo	[Fe/H]	err	Group
1650675	ab	0.5577	0.82	3697.5522	18.14	18.11	0.28	17.82	0.595	-0.035	I	-1.61	0.18	(D)
1653220	c	0.3313	0.52	3677.0992	15.47	15.45	0.43	15.02	0.615	NA	NA	-1.52	0.55	(I)
1682108	ab	0.5593	1.20	3696.9156	20.29	20.23	0.41	19.82	0.559	0.012	I	-1.78	0.38	(E)
1689293	ab	0.6333	0.71	3665.0447	18.95	18.93	0.37	18.56	0.576	0.007	I	-1.70	0.28	(E)
1689439	ab	0.5268	1.36	3697.2079	17.21	17.14	0.36	16.78	0.565	0.005	I	-1.75	0.43	(E)
1689618	ab	0.6434	1.08	3665.0609	18.41	18.36	0.38	17.98	0.529	0.059	II	-1.92	0.19	(D)
1693414	ab	0.5006	1.13	3996.3782	13.57	13.51	0.33	13.19	0.634	-0.045	I	-1.43	0.42	(E)
1703145	c	0.3766	0.50	3697.3022	17.82	17.80	0.40	17.40	0.615	NA	NA	-1.52	0.55	(I)
1708085	c	0.3050	0.19	3700.1540	14.72	14.72	0.38	14.34	0.662	NA	NA	-1.30	0.48	(G)
1716966	c	0.4199	0.51	3697.2210	17.99	17.97	0.47	17.51	0.615	NA	NA	-1.52	0.55	(I)
1720341	ab	0.6424	0.34	3664.9787	19.53	19.53	0.37	19.16	0.739	-0.031	I	-0.94	0.48	(D)
1727801	c	0.3430	0.48	4028.3263	13.88	13.87	0.36	13.51	0.615	NA	NA	-1.52	0.55	(I)
1731914	ab	0.5645	1.01	3670.0192	17.07	17.02	0.30	16.72	0.809	-0.008	I	-0.61	0.42	(B)
1743773	abB	0.6056	0.65	3697.2774	17.55	17.53	0.45	17.08	0.625	-0.019	I	-1.47	0.50	(B)
1753291	ab	0.4971	1.57	3668.2367	17.90	17.79	0.35	17.45	0.542	0.005	I	-1.86	0.15	(D)
1770598	ab	0.6633	1.04	3677.0130	15.50	15.45	0.32	15.13	0.403	0.066	II	-2.51	0.71	(B)

Table C.2: Photometric Properties of SDSS RRL (continued)

Variable	Type	P	Amp	Max Epoch	$< M >$	$< I >$	A	$< g0 >$	M	$\Delta \log P$	Oo	[Fe/H]	err	Group
1788251	ab	0.6278	0.63	3696.9545	19.38	19.36	0.31	19.05	0.595	-0.006	I	-1.61	0.28	(E)
1788975	c	0.2712	0.26	3699.9652	16.15	16.15	0.33	15.82	0.615	NA	NA	-1.52	0.55	(I)
1791896	c	0.3133	0.52	3700.2553	17.15	17.13	0.32	16.81	0.415	NA	NA	-2.45	0.02	(F)
1806631	ab	0.7234	0.66	3665.1668	17.17	17.15	0.30	16.85	0.514	0.059	II	-1.99	0.14	(D)
1814238	c	0.3295	0.54	3665.0816	18.09	18.07	0.31	17.76	0.615	NA	NA	-1.52	0.55	(I)
1817698	ab	0.5251	0.81	3694.2131	17.07	17.04	0.26	16.77	0.664	-0.063	I	-1.29	0.37	(E)
1834485	c	0.3103	0.51	3694.1669	15.67	15.66	0.27	15.38	0.615	NA	NA	-1.52	0.55	(I)
1838781	ab	0.4661	1.62	3694.0046	17.14	17.03	0.29	16.73	0.572	-0.018	I	-1.72	0.14	(D)
1839414	c	0.4093	0.41	3665.0917	14.05	14.05	0.30	13.74	0.615	NA	NA	-1.52	0.55	(I)
1843089	ab	0.5290	0.92	3665.1769	17.95	17.91	0.29	17.61	0.598	-0.046	I	-1.60	0.30	(D)
1845206	c	0.2242	0.16	3696.9360	15.51	15.51	0.30	15.21	0.615	NA	NA	-1.52	0.55	(I)
1849535	ab	0.6203	1.01	3656.5807	18.56	18.52	0.31	18.21	0.555	0.034	I	-1.80	0.35	(D)
1854030	ab	0.5894	1.10	3665.4290	18.89	18.84	0.30	18.54	0.495	0.023	I	-2.08	0.13	(D)
1854921	ab	0.5900	1.07	3664.8604	17.18	17.13	0.30	16.83	0.557	0.019	I	-1.79	0.54	(B)
1854976	ab	0.6910	0.88	3693.7751	16.40	16.37	0.34	16.03	0.501	0.065	II	-2.05	0.60	(B)
1856817	c	0.3666	0.63	3694.1769	15.70	15.67	0.30	15.38	0.658	NA	NA	-1.32	0.86	(G)

Table C.2: Photometric Properties of SDSS RRL (continued)

Variable	Type	P	Amp	Max Epoch	$< M >$	$< I >$	A	$< g0 >$	M	$\Delta \log P$	Oo	[Fe/H]	err	Group
1870663	c	0.3296	0.64	3996.2357	14.65	14.63	0.34	14.29	0.615	NA	NA	-1.52	0.55	(I)
187796	ab	0.6804	0.92	3626.3066	15.84	15.80	0.10	15.71	0.488	0.063	II	-2.11	0.16	(D)
1879867	ab	0.5817	0.89	3665.1895	15.76	15.73	0.33	15.40	0.677	-0.009	I	-1.23	0.47	(B)
1904451	ab	0.5895	0.98	3665.5239	19.40	19.36	0.49	18.86	0.598	0.008	I	-1.60	0.15	(D)
1904545	ab	0.6308	0.55	3664.9372	20.24	20.23	0.25	19.98	0.608	-0.014	I	-1.55	0.27	(E)
1908273	ab?	0.6329	0.28	3693.8713	18.65	18.64	0.29	18.35	0.653	-0.045	I	-1.34	0.25	(E)
1914679	ab	0.6579	1.26	3664.7887	17.80	17.73	0.26	17.48	0.473	0.089	II	-2.18	0.10	(D)
1915855	ab	0.5401	0.96	3675.1886	18.48	18.44	0.23	18.20	0.697	-0.032	I	-1.14	0.03	(A)
193232	ab	0.5558	1.04	3685.3426	17.06	17.01	0.10	16.91	0.606	-0.010	I	-1.56	0.04	(C)
1933665	ab	0.4557	1.54	3664.9660	19.45	19.35	0.46	18.89	0.621	-0.036	I	-1.49	0.14	(D)
1943904	c	0.3352	0.50	3665.0422	17.43	17.42	0.34	17.08	0.927	NA	NA	-0.06	0.51	(G)
1949959	ab	0.6106	0.85	3687.4562	16.37	16.34	0.27	16.07	0.563	0.008	I	-1.76	0.54	(B)
1950700	ab	0.5504	0.67	3668.3275	17.72	17.70	0.25	17.44	0.452	-0.059	I	-2.28	0.64	(B)
1960101	ab	0.5428	1.28	3694.1181	17.01	16.95	0.28	16.66	0.565	0.008	I	-1.75	0.54	(B)
19601	ab	0.7930	0.55	3681.4222	18.90	18.88	0.10	18.79	0.486	0.086	II	-2.12	0.19	(D)
1962720	ab	0.5281	1.38	3694.4171	16.86	16.77	0.33	16.44	0.559	0.008	I	-1.78	0.43	(E)

Table C.2: Photometric Properties of SDSS RRL (continued)

Variable	Type	P	Amp	Max Epoch	$< M >$	$< I >$	A	$< g0 >$	M	$\Delta \log P$	Oo	[Fe/H]	err	Group
1968253	c?	0.3881	0.27	3668.2445	14.89	14.89	0.37	14.52	0.790	NA	NA	-0.70	0.34	(G)
1978304	c?	0.4369	0.52	3705.0287	15.24	15.23	0.41	14.82	0.431	NA	NA	-2.38	0.69	(G)
1979749	c	0.2373	0.15	3665.1081	17.42	17.42	0.40	17.02	0.615	NA	NA	-1.52	0.55	(I)
1984658	c	0.3286	0.48	3694.0682	18.10	18.09	0.40	17.69	0.615	NA	NA	-1.52	0.55	(I)
1987864	ab	0.5122	1.15	3694.1128	15.64	15.57	0.44	15.13	0.617	-0.032	I	-1.51	0.42	(E)
2007031	abB?	0.9366	0.78	3693.7266	16.00	15.97	0.31	15.67	0.730	0.185	II	-0.98	0.42	(B)
2008263	ab	0.5713	1.02	3664.7109	15.86	15.81	0.46	15.35	0.580	-0.001	I	-1.68	0.53	(B)
2015807	c?	0.1907	0.17	3673.0737	14.52	14.52	0.43	14.09	0.615	NA	NA	-1.52	0.55	(I)
2021819	c	0.3689	0.20	3694.1120	14.63	14.63	0.43	14.20	0.615	NA	NA	-1.52	0.55	(I)
2021917	c	0.2806	0.58	3694.0793	16.53	16.52	0.37	16.15	0.615	NA	NA	-1.52	0.55	(I)
2022188	ab	0.5506	1.28	3687.3912	17.67	17.60	0.29	17.31	0.580	0.015	I	-1.68	0.12	(D)
2028388	ab	0.5276	0.99	3668.2254	17.10	17.05	0.40	16.65	0.630	-0.039	I	-1.45	0.39	(E)
2035884	c	0.3234	0.67	3694.2782	19.12	19.09	0.30	18.79	0.610	NA	NA	-1.54	0.10	(H)
2036397	ab	0.6475	0.95	3665.1193	17.93	17.89	0.32	17.57	0.559	0.045	II	-1.78	0.12	(D)
2041986	c	0.3603	0.49	3668.4564	16.31	16.30	0.42	15.88	0.604	NA	NA	-1.57	0.63	(G)
2042971	ab	0.6495	0.39	3668.4473	16.24	16.24	0.40	15.84	0.643	-0.021	I	-1.39	0.47	(B)

Table C.2: Photometric Properties of SDSS RRL (continued)

Variable	Type	P	Amp	Max Epoch	$< M >$	$< I >$	A	$< g0 >$	M	$\Delta \log P$	Oo	[Fe/H]	err	Group
2045615	abB	0.3462	1.23	3694.3381	16.28	16.22	0.31	15.91	0.675	-0.193	I	-1.24	0.45	(B)
2055722	ab	0.5930	0.96	3694.3460	16.81	16.77	0.28	16.49	0.506	0.008	I	-2.03	0.59	(B)
2056564	ab	0.6106	1.33	3694.0508	16.70	16.63	0.43	16.20	0.491	0.066	II	-2.10	0.61	(B)
2074459	ab	0.5743	0.99	3686.8426	17.86	17.81	0.26	17.55	0.591	-0.002	I	-1.63	0.13	(D)
2075021	ab	0.5986	0.59	3667.9454	16.40	16.38	0.44	15.94	0.649	-0.032	I	-1.36	0.48	(B)
2077610	ab	0.5156	1.17	3685.0148	17.59	17.52	0.22	17.31	0.653	-0.027	I	-1.34	0.04	(C)
2084910	c	0.3172	0.57	3668.0965	17.12	17.11	0.23	16.88	0.566	NA	NA	-1.75	0.04	(F)
2096118	c	0.3387	0.41	3694.0931	18.05	18.04	0.38	17.65	0.433	NA	NA	-2.37	0.66	(G)
2107186	c	0.2778	0.63	3665.3182	18.72	18.69	0.39	18.30	0.615	NA	NA	-1.52	0.55	(I)
2122667	cB	0.2983	0.36	3665.2033	17.67	17.66	0.30	17.36	0.615	NA	NA	-1.52	0.55	(I)
2125070	ab	0.5244	1.12	3687.0164	17.94	17.89	0.21	17.67	0.610	-0.026	I	-1.54	0.40	(E)
2126870	ab	0.6993	0.64	3694.4725	18.69	18.67	0.30	18.36	0.444	0.041	I	-2.32	0.16	(D)
2127489	c	0.3509	0.15	3665.0680	15.04	15.04	0.22	14.81	0.615	NA	NA	-1.52	0.55	(I)
2135439	ab	0.6048	1.04	3694.5000	16.12	16.06	0.31	15.75	0.544	0.027	I	-1.85	0.55	(B)
2140120	abB	0.6489	0.37	3693.8239	17.10	17.09	0.22	16.87	0.570	-0.023	I	-1.73	0.04	(C)
2148716	ab	0.5794	1.00	3694.0322	16.70	16.65	0.37	16.28	0.544	0.003	I	-1.85	0.09	(A)

Table C.2: Photometric Properties of SDSS RRL (continued)

Variable	Type	P	Amp	Max Epoch	$< M >$	$< I >$	A	$< g0 >$	M	$\Delta \log P$	Oo	[Fe/H]	err	Group
2163750	ab	0.5365	1.30	3687.2065	16.66	16.59	0.33	16.27	0.595	0.005	I	-1.61	0.08	(A)
217320	ab	0.6074	0.62	3693.9806	16.34	16.33	0.09	16.24	0.683	-0.022	I	-1.20	0.06	(A)
2179468	ab	0.5625	1.18	3665.3844	17.93	17.87	0.27	17.60	0.561	0.012	I	-1.77	0.38	(E)
2181657	ab	0.5215	1.04	3694.5745	15.83	15.78	0.18	15.60	0.506	-0.037	I	-2.03	0.59	(B)
2192592	ab	0.5877	0.90	3665.1140	18.00	17.96	0.21	17.75	0.606	-0.003	I	-1.56	0.13	(D)
2194097	c	0.2904	0.61	3665.1265	17.51	17.49	0.26	17.23	0.724	NA	NA	-1.01	0.01	(F)
2200232	ab	0.6303	1.35	3656.3896	14.81	14.73	0.18	14.55	0.548	0.081	II	-1.83	0.56	(B)
2202958	c	0.2167	0.21	3668.0308	17.51	17.51	0.17	17.34	0.745	NA	NA	-0.91	0.39	(G)
2205327	ab	0.6470	0.82	3665.6124	17.08	17.05	0.25	16.79	0.360	0.029	I	-2.71	0.75	(B)
2211741	ab	0.7430	0.39	3694.0234	17.39	17.39	0.18	17.21	0.553	0.037	I	-1.81	0.35	(D)
2229203	ab	0.5687	0.97	3692.9732	15.31	15.26	0.21	15.05	0.493	-0.008	I	-2.09	0.61	(B)
2240050	cB	0.2450	0.64	3694.1234	15.68	15.65	0.19	15.47	0.507	NA	NA	-2.02	0.01	(H)
2242178	ab	0.5802	0.99	3686.9643	17.21	17.17	0.23	16.94	0.553	0.002	I	-1.81	0.55	(B)
2248863	ab	0.6143	0.62	3664.8438	17.08	17.07	0.19	16.88	0.683	-0.018	I	-1.20	0.46	(B)
2250063	ab	0.6011	0.77	3697.4926	16.14	16.12	0.18	15.94	0.677	-0.009	I	-1.23	0.03	(C)
2253693	ab	0.4758	1.22	3665.1806	18.07	17.99	0.19	17.80	0.647	-0.057	I	-1.37	0.46	(E)

Table C.2: Photometric Properties of SDSS RRL (continued)

Variable	Type	P	Amp	Max Epoch	$< M >$	$< I >$	A	$< g0 >$	M	$\Delta \log P$	Oo	[Fe/H]	err	Group
2255955	c	0.2898	0.42	3694.1503	17.54	17.53	0.18	17.36	0.615	NA	NA	-1.52	0.55	(I)
2269900	ab	0.6224	0.94	3694.1740	19.20	19.16	0.19	18.98	0.514	0.027	I	-1.99	0.12	(D)
2275534	c	0.2754	0.35	3694.2544	17.92	17.91	0.17	17.74	0.625	NA	NA	-1.47	0.32	(H)
2279117	ab	0.6395	1.25	3694.5029	17.86	17.79	0.17	17.62	0.503	0.076	II	-2.04	0.11	(D)
2286970	c	0.4283	0.53	3656.1892	15.42	15.41	0.18	15.23	0.691	NA	NA	-1.16	0.04	(H)
2288071	ab	0.5616	1.10	3694.6033	16.98	16.92	0.19	16.73	0.543	0.002	I	-1.86	0.03	(A)
2291454	ab	0.5947	0.99	3655.8816	19.12	19.08	0.15	18.93	0.629	0.013	I	-1.45	0.03	(C)
2303228	ab	0.5454	0.81	3687.4182	18.66	18.63	0.18	18.45	0.643	-0.047	I	-1.39	0.36	(E)
2303487	ab	0.5171	1.00	3694.4939	18.39	18.34	0.17	18.17	0.576	-0.046	I	-1.70	0.09	(A)
2314353	c	0.3977	0.56	3687.1913	14.82	14.80	0.16	14.64	0.414	NA	NA	-2.46	0.69	(G)
2319786	ab	0.4807	1.24	3700.2550	14.12	14.04	0.18	13.86	0.636	-0.049	I	-1.42	0.45	(E)
2325897	c	0.3018	0.51	3687.2234	16.27	16.25	0.17	16.08	0.615	NA	NA	-1.52	0.55	(I)
2328485	abB	0.6618	0.50	3667.9605	14.33	14.31	0.17	14.14	0.589	0.001	I	-1.64	0.24	(E)
2338371	c	0.3942	0.62	3687.3051	16.39	16.37	0.21	16.16	0.484	NA	NA	-2.13	0.07	(H)
2346078	ab	0.4940	1.58	3664.7231	17.57	17.46	0.19	17.28	0.544	0.003	I	-1.85	0.08	(A)
2361466	c	0.3059	0.61	3694.2200	16.60	16.58	0.22	16.37	0.760	NA	NA	-0.84	0.52	(G)

Table C.2: Photometric Properties of SDSS RRL (continued)

Variable	Type	P	Amp	Max Epoch	$< M >$	$< I >$	A	$< g0 >$	M	$\Delta \log P$	Oo	[Fe/H]	err	Group
2367759	c	0.3620	0.50	3670.3046	15.94	15.92	0.18	15.74	0.593	NA	NA	-1.62	0.05	(F)
2371159	ab	0.5011	1.37	3687.2281	18.63	18.55	0.16	18.39	0.591	-0.016	I	-1.63	0.45	(E)
2371287	c	0.3360	0.53	3655.9861	15.66	15.64	0.20	15.44	0.627	NA	NA	-1.46	0.03	(F)
2376453	ab	0.7121	0.79	3697.4423	16.06	16.03	0.18	15.85	0.499	0.067	II	-2.06	0.24	(E)
237692	ab	0.6222	1.07	3685.3746	19.38	19.33	0.09	19.24	0.555	0.042	I	-1.80	0.12	(D)
2377638	c	0.2863	0.42	3697.2670	16.02	16.01	0.19	15.83	0.629	NA	NA	-1.46	0.09	(H)
2408962	ab	0.5743	0.85	3664.9770	16.80	16.77	0.29	16.49	0.497	-0.019	I	-2.07	0.60	(B)
2411556	c	0.3977	0.47	3694.1912	15.93	15.92	0.18	15.74	0.611	NA	NA	-1.54	0.02	(F)
2423189	ab	0.7188	0.86	3686.8728	16.38	16.35	0.20	16.14	0.270	0.080	II	-3.13	0.86	(B)
2425905	ab	0.5514	1.41	3667.8496	15.27	15.17	0.18	14.99	0.617	0.030	I	-1.51	0.49	(B)
2441045	c	0.3879	0.52	3665.1407	18.26	18.25	0.24	18.00	0.461	NA	NA	-2.24	0.15	(F)
2455878	ab	0.5499	1.24	3694.4613	18.06	17.99	0.19	17.80	0.553	0.008	I	-1.81	0.10	(D)
2464378	ab	0.5371	1.22	3665.0398	17.99	17.93	0.24	17.69	0.518	-0.004	I	-1.97	0.18	(D)
2469472	ab	0.6222	0.68	3664.9901	17.80	17.78	0.18	17.60	0.576	-0.005	I	-1.70	0.14	(D)
2478738	ab	0.5942	0.74	3694.3690	17.58	17.55	0.21	17.34	0.561	-0.017	I	-1.77	0.55	(B)
2478919	abB	0.5191	1.02	3664.7599	16.65	16.60	0.20	16.40	0.632	-0.042	I	-1.44	0.40	(E)

Table C.2: Photometric Properties of SDSS RRL (continued)

Variable	Type	P	Amp	Max Epoch	$< M >$	$< I >$	A	$< g0 >$	M	$\Delta \log P$	Oo	[Fe/H]	err	Group
2480640	ab	0.5808	0.91	3665.2925	18.89	18.86	0.21	18.65	0.591	-0.007	I	-1.63	0.34	(E)
2483003	ab	0.4712	1.56	3694.3285	17.83	17.73	0.20	17.52	0.677	-0.020	I	-1.23	0.28	(D)
2510603	ab	0.6164	0.78	3664.8840	14.64	14.62	0.26	14.36	0.606	0.003	I	-1.56	0.51	(B)
2510616	c	0.3481	0.34	3653.9897	16.83	16.82	0.26	16.56	0.540	NA	NA	-1.87	0.07	(H)
2512234	ab	0.6750	0.99	3687.4561	16.05	16.01	0.15	15.85	0.381	0.068	II	-2.61	0.73	(B)
2518975	c	0.3489	0.53	3687.4186	17.09	17.07	0.27	16.80	0.615	NA	NA	-1.52	0.55	(I)
2526240	ab	0.5526	1.20	3687.1980	16.85	16.79	0.26	16.53	0.572	0.006	I	-1.72	0.11	(D)
2530960	ab	0.5197	1.35	3687.3780	18.03	17.95	0.32	17.63	0.565	-0.002	I	-1.75	0.10	(D)
2539586	ab	0.5238	0.94	3687.3188	18.32	18.28	0.34	17.94	0.643	-0.048	I	-1.39	0.39	(E)
2545670	ab	0.5980	0.96	3664.8889	17.16	17.12	0.20	16.91	0.565	0.012	I	-1.75	0.33	(E)
2547187	ab	0.5762	1.36	3665.3854	17.18	17.10	0.56	16.54	0.709	0.044	I	-1.08	0.42	(B)
2553011	ab	0.5778	0.82	3664.8829	17.34	17.31	0.43	16.88	0.630	-0.019	I	-1.45	0.14	(A)
2554564	ab	0.6222	1.03	3664.6366	17.25	17.20	0.44	16.77	0.612	0.037	I	-1.53	0.15	(A)
2555926	ab	0.6217	0.83	3665.0777	19.85	19.82	0.35	19.47	0.565	0.014	I	-1.75	0.30	(E)
2563997	ab	0.8109	1.37	3687.0095	17.66	17.58	0.53	17.05	0.266	0.194	II	-3.15	0.17	(D)
2584203	ab	0.4754	1.56	3656.2870	15.75	15.64	0.26	15.38	0.854	-0.016	I	-0.40	0.44	(B)

Table C.2: Photometric Properties of SDSS RRL (continued)

Variable	Type	P	Amp	Max Epoch	$< M >$	$< I >$	A	$< g0 >$	M	$\Delta \log P$	Oo	[Fe/H]	err	Group
2585370	ab	0.6758	0.56	3687.5620	18.55	18.54	0.65	17.89	0.512	0.017	I	-2.00	0.23	(A)
2599429	ab	0.5702	1.21	3656.2505	18.04	17.98	0.29	17.68	0.604	0.021	I	-1.57	0.04	(C)
2604319	ab	0.5913	0.84	3656.1461	17.22	17.19	0.53	16.65	0.518	-0.007	I	-1.97	0.17	(A)
2617725	ab	0.6513	0.74	3687.3146	16.58	16.56	0.28	16.28	0.550	0.023	I	-1.82	0.11	(A)
2623071	ab	0.5752	0.93	3656.4885	18.17	18.13	0.49	17.64	0.487	-0.008	I	-2.12	0.08	(C)
2628577	c	0.2736	0.39	3676.0860	20.19	20.18	0.47	19.71	0.615	NA	NA	-1.52	0.55	(I)
26293	abB	0.6472	1.07	3627.8905	16.12	16.07	0.14	15.94	0.469	0.059	II	-2.20	0.04	(C)
263605	ab	0.8188	0.47	3697.0052	14.59	14.58	0.07	14.51	0.533	0.089	II	-1.90	0.57	(B)
2638641	ab	0.6020	0.63	3686.2344	14.36	14.34	0.27	14.07	0.619	-0.025	I	-1.50	0.30	(E)
2646637	ab	0.4913	1.11	3685.0170	18.14	18.07	0.50	17.57	0.609	-0.056	I	-1.54	0.18	(C)
2651617	abB	0.5099	1.04	3655.7498	19.25	19.19	0.24	18.96	0.786	-0.048	I	-0.72	0.19	(C)
2652576	c	0.2541	0.32	3656.1621	15.28	15.27	0.44	14.83	0.615	NA	NA	-1.52	0.55	(I)
2655720	c	0.3386	0.48	3656.2591	16.42	16.41	0.19	16.21	0.640	NA	NA	-1.40	0.46	(G)
2659778	ab	0.5642	1.06	3656.3738	15.94	15.90	0.40	15.50	0.574	-0.002	I	-1.71	0.54	(B)
2660264	ab	0.5478	1.23	3686.7161	17.08	17.02	0.20	16.81	0.501	0.006	I	-2.05	0.60	(B)
2676003	c	0.3448	0.50	3687.0813	17.51	17.50	0.29	17.21	0.615	NA	NA	-1.52	0.55	(I)

Table C.2: Photometric Properties of SDSS RRL (continued)

Variable	Type	P	Amp	Max Epoch	$< M >$	$< I >$	A	$< g0 >$	M	$\Delta \log P$	Oo	[Fe/H]	err	Group
2686883	ab	0.4739	1.00	3670.3310	14.05	14.00	0.22	13.78	0.784	-0.084	I	-0.73	0.40	(B)
2701634	c	0.2978	0.33	3656.0627	18.13	18.12	0.19	17.93	0.615	NA	NA	-1.52	0.55	(I)
2706750	abB	0.4958	1.54	3694.1512	15.78	15.68	0.21	15.46	0.568	0.000	I	-1.74	0.47	(E)
270817	ab	0.6098	1.03	3685.1758	17.47	17.43	0.08	17.35	0.613	0.029	I	-1.53	0.07	(C)
2716972	ab?	0.5757	0.80	3637.5298	14.72	14.69	0.21	14.48	0.668	-0.024	I	-1.27	0.48	(B)
2718789	ab	0.6071	0.81	3653.9796	18.37	18.34	0.23	18.11	0.531	0.001	I	-1.91	0.20	(D)
2720649	ab	0.5854	0.68	3656.2049	18.88	18.86	0.24	18.62	0.569	-0.031	I	-1.74	0.23	(A)
2726067	ab	0.5003	1.45	3687.0309	16.86	16.75	0.18	16.57	0.578	-0.007	I	-1.69	0.46	(E)
2728156	ab	0.5679	1.06	3687.5619	16.86	16.81	0.31	16.50	0.645	0.002	I	-1.38	0.49	(B)
2741575	ab	0.5662	1.06	3687.0968	16.59	16.54	0.25	16.29	0.771	0.000	I	-0.79	0.46	(B)
2743740	ab	0.5833	0.96	3993.1817	14.25	14.21	0.44	13.78	0.636	0.001	I	-1.42	0.49	(B)
2744412	ab	0.4959	1.42	3687.0213	19.40	19.31	0.31	19.00	0.570	-0.014	I	-1.73	0.14	(D)
2745760	ab	0.4675	1.47	3687.0113	18.83	18.73	0.43	18.30	0.600	-0.034	I	-1.59	0.11	(D)
2747989	ab	0.4593	0.77	3704.9766	14.42	14.39	0.19	14.20	0.394	-0.126	I	-2.55	0.71	(B)
2753811	c	0.3165	0.18	3685.3600	18.95	18.94	0.42	18.53	0.615	NA	NA	-1.52	0.55	(I)
2762264	ab	0.6314	0.99	3687.2670	15.99	15.94	0.31	15.63	0.499	0.039	I	-2.06	0.60	(B)

Table C.2: Photometric Properties of SDSS RRL (continued)

Variable	Type	P	Amp	Max Epoch	$< M >$	$< I >$	A	$< g0 >$	M	$\Delta \log P$	Oo	[Fe/H]	err	Group
2763274	ab	0.6161	0.66	3702.9109	18.43	18.41	0.34	18.07	0.568	-0.011	I	-1.74	0.16	(D)
2764164	ab	0.6040	0.89	3644.2893	19.60	19.56	0.23	19.33	0.538	0.007	I	-1.88	0.18	(D)
2766251	ab	0.5020	1.36	3656.4352	18.07	17.97	0.18	17.79	0.566	-0.016	I	-1.75	0.09	(A)
2781708	c	0.3017	0.58	3687.0851	16.61	16.59	0.34	16.25	0.617	NA	NA	-1.51	0.09	(F)
2788149	ab	0.6586	0.91	3644.0171	19.53	19.49	0.18	19.31	0.463	0.047	II	-2.23	0.32	(D)
2794135	ab	0.5808	0.77	3687.1285	17.64	17.61	0.34	17.26	0.615	-0.023	I	-1.52	0.32	(E)
2794423	c	0.3323	0.50	3302.4919	19.47	19.46	0.23	19.23	0.615	NA	NA	-1.52	0.55	(I)
2800504	abB	0.5053	1.21	3675.3559	17.16	17.08	0.20	16.88	0.629	-0.031	I	-1.45	0.03	(C)
2801516	c	0.3953	0.55	3693.9199	16.63	16.61	0.23	16.38	0.615	NA	NA	-1.52	0.55	(I)
2801989	ab	0.5031	1.40	3654.1440	18.12	18.04	0.23	17.81	0.627	-0.010	I	-1.46	0.07	(C)
2803055	ab	0.5714	1.06	3687.0454	17.29	17.23	0.35	16.88	0.563	0.004	I	-1.76	0.11	(D)
2805929	c	0.3505	0.51	3687.1299	16.25	16.23	0.23	16.00	0.561	NA	NA	-1.77	0.07	(H)
2814984	c	0.3366	0.54	3654.2196	17.20	17.19	0.35	16.84	0.636	NA	NA	-1.42	0.13	(H)
2835133	ab	0.5330	1.08	3644.3123	19.98	19.92	0.36	19.56	0.608	-0.024	I	-1.55	0.39	(E)
2839664	ab	0.6028	0.76	3694.1752	18.79	18.76	0.37	18.39	0.576	-0.009	I	-1.70	0.20	(D)
2858234	ab	0.6556	1.16	3636.5902	14.68	14.62	0.33	14.30	0.565	0.076	II	-1.75	0.54	(B)

Table C.2: Photometric Properties of SDSS RRL (continued)

Variable	Type	P	Amp	Max Epoch	$< M >$	$< I >$	A	$< g0 >$	M	$\Delta \log P$	Oo	[Fe/H]	err	Group
2858731	ab	0.6220	1.05	3687.2416	17.30	17.25	0.32	16.93	0.550	0.040	I	-1.82	0.11	(C)
286700	ab	0.6244	0.65	3628.5876	19.62	19.60	0.08	19.52	0.531	-0.007	I	-1.91	0.14	(D)
2869752	ab	0.6361	1.33	3654.3138	18.92	18.85	0.33	18.51	0.491	0.083	II	-2.10	0.12	(D)
2870122	ab	0.5613	1.25	3654.0494	19.70	19.64	0.33	19.31	0.542	0.019	I	-1.86	0.13	(D)
2888418	c	0.3492	0.57	3696.9832	14.58	14.56	0.25	14.31	0.615	NA	NA	-1.52	0.55	(I)
2890944	ab	0.5875	1.15	3654.2248	17.94	17.88	0.21	17.67	0.559	0.027	I	-1.78	0.15	(D)
2894713	ab	0.5084	1.33	3656.1414	16.42	16.35	0.24	16.11	0.687	-0.014	I	-1.18	0.46	(B)
28977	ab	0.6418	0.60	3628.1811	17.12	17.11	0.12	16.98	0.632	-0.001	I	-1.44	0.06	(C)
2900805	ab	0.5865	0.66	3687.0007	17.74	17.72	0.24	17.48	0.525	-0.032	I	-1.94	0.15	(D)
2912876	c?	0.2753	0.34	3654.0414	16.79	16.78	0.31	16.47	0.630	NA	NA	-1.45	0.12	(H)
2921362	ab	0.5768	0.89	3643.8482	17.36	17.32	0.26	17.06	0.598	-0.012	I	-1.60	0.34	(E)
2927712	c	0.3589	0.52	3694.3606	17.42	17.41	0.29	17.12	0.615	NA	NA	-1.52	0.55	(I)
2930308	ab	0.6152	1.23	3643.9951	20.44	20.38	0.29	20.08	0.486	0.057	II	-2.12	0.13	(D)
2930888	ab	0.6224	0.86	3644.2047	16.25	16.21	0.27	15.94	0.589	0.017	I	-1.64	0.09	(A)
2932935	c	0.3298	0.51	3687.1003	17.72	17.70	0.32	17.38	0.615	NA	NA	-1.52	0.55	(I)
2940701	ab	0.4840	1.64	3697.0182	14.26	14.15	0.34	13.81	0.563	0.001	I	-1.76	0.49	(E)

Table C.2: Photometric Properties of SDSS RRL (continued)

Variable	Type	P	Amp	Max Epoch	$< M >$	$< I >$	A	$< g0 >$	M	$\Delta \log P$	Oo	[Fe/H]	err	Group
2953315	c	0.3156	0.49	3675.1928	17.56	17.55	0.27	17.28	0.615	NA	NA	-1.52	0.55	(I)
2960182	ab	0.5427	0.87	3627.7585	14.36	14.32	0.24	14.09	0.600	-0.042	I	-1.59	0.51	(B)
2964169	ab	0.4652	1.26	3636.9446	15.14	15.06	0.24	14.82	0.625	-0.061	I	-1.47	0.48	(B)
2965347	c	0.2538	0.20	3694.1063	14.36	14.36	0.25	14.11	0.615	NA	NA	-1.52	0.55	(I)
2983558	cB	0.3668	0.15	3644.4613	16.68	16.68	0.32	16.36	0.615	NA	NA	-1.52	0.55	(I)
2984333	c	0.3123	0.57	3644.1941	16.67	16.65	0.27	16.39	0.550	NA	NA	-1.82	0.12	(F)
2985501	ab	0.6703	0.39	3687.1892	17.27	17.26	0.27	16.99	0.598	-0.007	I	-1.60	0.52	(B)
2998988	ab	0.6030	0.85	3686.6848	17.33	17.29	0.31	16.98	0.568	0.003	I	-1.74	0.17	(A)
2999145	c	0.2297	0.25	3616.3833	14.27	14.27	0.26	14.01	0.878	NA	NA	-0.29	0.43	(G)
3002611	ab?	0.7124	0.48	3687.2840	19.37	19.36	0.24	19.11	0.553	0.030	I	-1.81	0.21	(E)
3006489	ab	0.5300	1.37	3686.9105	18.00	17.92	0.31	17.61	0.566	0.008	I	-1.75	0.02	(C)
3010656	c?	0.2141	0.15	3644.2713	18.41	18.41	0.33	18.07	0.579	NA	NA	-1.69	0.12	(F)
3012156	abB	0.4461	1.13	3687.2327	17.48	17.42	0.21	17.22	0.622	-0.095	I	-1.49	0.16	(C)
3013503	ab	0.4591	1.55	3644.4175	17.49	17.39	0.24	17.15	0.621	-0.032	I	-1.49	0.13	(D)
3022511	c	0.2687	0.16	3687.2523	17.19	17.18	0.19	16.99	0.615	NA	NA	-1.52	0.55	(I)
3023484	ab	0.5858	0.93	3687.0618	18.67	18.63	0.19	18.44	0.619	-0.001	I	-1.50	0.10	(D)

Table C.2: Photometric Properties of SDSS RRL (continued)

Variable	Type	P	Amp	Max Epoch	$< M >$	$< I >$	A	$< g0 >$	M	$\Delta \log P$	Oo	[Fe/H]	err	Group
3025286	ab	0.5426	1.49	3687.0855	17.86	17.76	0.21	17.55	0.469	0.033	I	-2.20	0.01	(A)
3034077	ab	0.5327	1.16	3644.5680	16.45	16.39	0.19	16.20	0.608	-0.014	I	-1.55	0.50	(B)
3041792	ab	0.7584	0.80	3643.6386	16.92	16.89	0.23	16.66	0.553	0.095	II	-1.81	0.11	(D)
3057986	ab	0.5576	1.03	3687.2226	20.26	20.21	0.19	20.02	0.591	-0.010	I	-1.63	0.37	(E)
3058946	ab	0.5548	1.39	3644.2780	17.40	17.32	0.21	17.10	0.547	0.031	I	-1.84	0.03	(C)
3065604	ab	0.5861	0.92	3687.4501	18.74	18.70	0.20	18.50	0.570	-0.002	I	-1.73	0.08	(C)
3069481	ab	0.6821	0.86	3686.9619	20.16	20.13	0.21	19.91	0.510	0.057	II	-2.01	0.26	(E)
3082830	ab	0.5499	0.96	3687.0893	17.03	16.99	0.23	16.76	0.519	-0.024	I	-1.97	0.10	(C)
3089339	ab	0.6876	0.45	3687.3640	17.03	17.02	0.21	16.81	0.619	0.012	I	-1.50	0.19	(D)
3096217	ab	0.5078	1.28	3687.2976	18.75	18.68	0.28	18.40	0.591	-0.020	I	-1.63	0.14	(D)
3100068	ab	0.5709	1.03	3637.0739	17.99	17.94	0.24	17.69	0.578	0.001	I	-1.69	0.36	(E)
3104441	abB	0.3411	1.04	3694.2174	20.33	20.28	0.20	20.08	0.861	-0.223	I	-0.37	0.60	(E)
3120139	c	0.2623	0.31	3694.1277	17.60	17.59	0.30	17.29	0.640	NA	NA	-1.40	0.13	(F)
3132461	ab	0.4547	1.42	3687.2340	17.43	17.33	0.35	16.98	0.630	-0.052	I	-1.45	0.18	(D)
3134228	ab	0.6317	0.57	3636.7739	18.89	18.87	0.37	18.50	0.551	-0.011	I	-1.82	0.15	(D)
3140488	ab	0.5369	1.30	3636.9257	15.68	15.61	0.34	15.27	0.529	0.006	I	-1.92	0.26	(D)

Table C.2: Photometric Properties of SDSS RRL (continued)

Variable	Type	P	Amp	Max Epoch	$< M >$	$< I >$	A	$< g0 >$	M	$\Delta \log P$	Oo	[Fe/H]	err	Group
314320	c	0.3390	0.58	3628.2641	17.46	17.44	0.08	17.36	0.562	NA	NA	-1.77	0.08	(H)
3154303	c	0.3052	0.68	3637.4335	19.66	19.63	0.34	19.29	0.615	NA	NA	-1.52	0.55	(I)
3156028	c	0.4081	0.58	3637.3317	18.85	18.83	0.36	18.47	0.615	NA	NA	-1.52	0.55	(I)
3156554	ab	0.4693	1.64	3637.4836	16.89	16.78	0.34	16.44	0.591	-0.012	I	-1.63	0.14	(D)
3200435	c	0.3396	0.56	3637.3353	14.87	14.86	0.27	14.58	0.615	NA	NA	-1.52	0.55	(I)
320052	ab	0.6035	1.24	3685.0920	16.91	16.84	0.08	16.77	0.446	0.049	II	-2.31	0.08	(A)
3208965	abB	0.6506	0.36	3687.1666	16.89	16.89	0.22	16.67	0.551	-0.023	I	-1.82	0.56	(B)
3211444	ab	0.5040	1.44	3694.0145	20.01	19.92	0.19	19.73	0.578	-0.004	I	-1.69	0.15	(D)
3215255	c	0.2827	0.53	3694.2886	15.99	15.98	0.22	15.76	0.659	NA	NA	-1.31	0.03	(F)
3225128	abB	0.3625	1.02	3693.9771	18.19	18.15	0.21	17.94	0.638	-0.199	I	-1.41	0.03	(C)
3244819	ab	0.6268	0.89	3681.5093	16.89	16.86	0.20	16.66	0.580	0.023	I	-1.68	0.53	(B)
325148	cB	0.3382	0.59	3628.4519	16.83	16.81	0.07	16.74	0.595	NA	NA	-1.61	0.06	(F)
3285218	c	0.3509	0.54	3681.2449	16.08	16.06	0.17	15.88	0.644	NA	NA	-1.38	0.02	(F)
3301492	c	0.3468	0.58	3681.2000	19.45	19.43	0.18	19.26	0.615	NA	NA	-1.52	0.55	(I)
3308107	ab	0.4601	1.57	3623.1635	17.07	16.96	0.15	16.81	0.615	-0.029	I	-1.52	0.18	(D)
3309727	ab	0.7153	0.76	3623.2516	15.22	15.20	0.16	15.04	0.707	0.066	II	-1.09	0.45	(B)

Table C.2: Photometric Properties of SDSS RRL (continued)

Variable	Type	P	Amp	Max Epoch	$< M >$	$< I >$	A	$< g0 >$	M	$\Delta \log P$	Oo	[Fe/H]	err	Group
3312938	c	0.3287	0.65	3623.0204	17.89	17.86	0.14	17.72	0.590	NA	NA	-1.64	0.07	(F)
3321123	ab	0.5789	0.82	3685.3351	18.45	18.41	0.17	18.24	0.542	-0.019	I	-1.86	0.19	(D)
3324369	ab	0.5569	1.02	3616.2142	20.14	20.09	0.14	19.96	0.595	-0.012	I	-1.61	0.37	(E)
3326202	ab	0.6432	0.55	3616.3296	19.60	19.59	0.17	19.42	0.598	-0.006	I	-1.60	0.26	(E)
3326894	ab	0.4694	1.59	3681.3771	16.70	16.59	0.14	16.45	0.625	-0.018	I	-1.47	0.08	(A)
3344095	cB	0.3629	0.42	3681.2869	20.02	20.01	0.17	19.84	0.615	NA	NA	-1.52	0.55	(I)
3346605	ab	0.6868	0.98	3623.9188	18.54	18.50	0.17	18.33	0.658	0.075	II	-1.32	0.10	(A)
3348445	c	0.3351	0.57	3680.9567	16.72	16.70	0.18	16.52	0.605	NA	NA	-1.56	0.01	(H)
3349511	ab	0.6308	0.54	3626.4133	16.33	16.32	0.17	16.15	0.604	-0.015	I	-1.57	0.15	(D)
3352525	ab	0.4864	1.33	3681.2100	17.83	17.74	0.16	17.57	0.605	-0.033	I	-1.57	0.16	(A)
336651	ab	0.5922	0.93	3628.1649	17.71	17.67	0.06	17.60	0.617	0.004	I	-1.51	0.07	(C)
3381185	ab	0.6309	0.60	3678.8066	20.56	20.55	0.21	20.33	0.600	-0.008	I	-1.59	0.27	(E)
3398791	ab	0.6428	0.27	3680.9531	17.45	17.45	0.18	17.27	0.605	-0.040	I	-1.56	0.06	(C)
3407559	ab	0.6732	1.05	3679.4843	18.00	17.95	0.18	17.77	0.499	0.075	II	-2.06	0.11	(D)
3422033	ab	0.5160	1.40	3681.5039	16.50	16.42	0.16	16.26	0.653	-0.000	I	-1.34	0.03	(C)
3422195	ab	0.4560	1.58	3626.4474	18.21	18.11	0.15	17.95	0.623	-0.032	I	-1.48	0.10	(D)

Table C.2: Photometric Properties of SDSS RRL (continued)

Variable	Type	P	Amp	Max Epoch	$< M >$	$< I >$	A	$< g0 >$	M	$\Delta \log P$	Oo	[Fe/H]	err	Group
3434383	ab	0.5431	1.29	3623.0542	20.18	20.11	0.15	19.96	0.461	0.009	I	-2.24	0.13	(D)
3443067	c	0.2913	0.37	3681.2122	16.86	16.85	0.14	16.71	0.536	NA	NA	-1.89	0.06	(F)
3461129	c	0.4324	0.50	3679.0853	15.58	15.57	0.11	15.45	0.456	NA	NA	-2.26	0.68	(G)
3462783	ab	0.5364	1.02	3679.0806	18.29	18.24	0.13	18.11	0.615	-0.028	I	-1.52	0.38	(E)
3463795	ab	0.5875	0.99	3666.2434	15.84	15.80	0.16	15.65	0.562	0.008	I	-1.77	0.05	(A)
3479617	ab	0.4983	1.54	3628.3775	17.11	17.01	0.14	16.87	0.563	0.003	I	-1.76	0.47	(E)
3503214	ab	0.6262	0.71	3626.1476	18.42	18.40	0.15	18.25	0.660	0.002	I	-1.31	0.06	(C)
3507963	ab	0.6712	0.96	3628.2474	19.92	19.88	0.14	19.74	0.531	0.062	II	-1.91	0.13	(D)
3527029	ab	0.5894	0.90	3626.2164	19.62	19.58	0.14	19.44	0.844	-0.002	I	-0.45	0.15	(C)
3528959	abB	0.6132	1.02	3680.7610	18.61	18.57	0.15	18.42	0.498	0.030	I	-2.06	0.17	(A)
3539383	cB	0.2756	0.49	3679.1344	19.37	19.36	0.13	19.23	0.660	NA	NA	-1.31	0.33	(F)
3549941	ab	0.5056	1.11	3681.3749	14.56	14.51	0.13	14.38	0.632	-0.043	I	-1.44	0.47	(B)
3565861	abB	0.7168	0.75	3685.1441	14.92	14.90	0.10	14.80	0.473	0.065	II	-2.18	0.05	(A)
3574691	ab	0.6006	0.85	3628.2504	17.17	17.14	0.12	17.02	0.574	0.001	I	-1.71	0.54	(B)
3574739	ab	0.5666	0.80	3628.2133	19.95	19.92	0.13	19.79	0.555	-0.030	I	-1.80	0.22	(D)
3585054	ab	0.6551	0.44	3681.0845	17.83	17.82	0.12	17.70	0.541	-0.011	I	-1.86	0.08	(C)

Table C.2: Photometric Properties of SDSS RRL (continued)

Variable	Type	P	Amp	Max Epoch	$< M >$	$< I >$	A	$< g0 >$	M	$\Delta \log P$	Oo	[Fe/H]	err	Group
3588816	ab	0.5956	1.01	3681.2615	20.53	20.48	0.14	20.34	0.463	0.016	I	-2.23	0.32	(D)
3605512	ab	0.6251	0.65	3625.9402	17.93	17.91	0.17	17.75	0.556	-0.006	I	-1.79	0.07	(A)
3612526	ab	0.5702	1.48	3626.6274	15.70	15.61	0.11	15.50	0.559	0.053	II	-1.78	0.07	(A)
3626602	c	0.2178	0.27	3628.3077	17.00	16.99	0.11	16.88	0.784	NA	NA	-0.73	0.02	(F)
3626894	ab	0.6692	1.01	3679.2622	15.26	15.21	0.10	15.12	0.548	0.066	II	-1.83	0.13	(D)
3685041	ab	0.6133	0.65	3681.5910	17.80	17.78	0.14	17.64	0.584	-0.015	I	-1.66	0.07	(A)
3689799	ab	0.6258	1.27	3628.4295	16.26	16.20	0.14	16.06	0.395	0.069	II	-2.55	0.06	(A)
3690770	ab	0.5504	0.79	3694.6501	14.20	14.18	0.10	14.08	0.715	-0.044	I	-1.05	0.51	(B)
371848	ab	0.5159	1.03	3685.6148	17.50	17.45	0.09	17.36	0.665	-0.044	I	-1.29	0.09	(A)
395488	ab	0.5801	0.97	3694.1312	19.21	19.16	0.12	19.04	0.580	-0.000	I	-1.68	0.34	(E)
399535	ab	0.5506	1.12	3685.5915	17.62	17.57	0.14	17.43	0.598	-0.005	I	-1.60	0.04	(A)
400644	ab	0.5270	1.47	3637.1262	16.66	16.57	0.09	16.47	0.576	0.018	I	-1.70	0.10	(D)
426946	c	0.3849	0.57	3628.3910	18.15	18.13	0.09	18.03	0.500	NA	NA	-2.06	0.15	(H)
452040	ab	0.5015	0.73	3628.4217	16.62	16.60	0.14	16.46	0.702	-0.092	I	-1.11	0.39	(E)
464636	ab	0.6355	0.59	3626.5307	16.08	16.07	0.11	15.95	0.700	-0.006	I	-1.12	0.45	(B)
483608	ab	0.7450	0.54	3685.1414	19.75	19.73	0.14	19.59	0.495	0.057	II	-2.08	0.83	(D)

Table C.2: Photometric Properties of SDSS RRL (continued)

Variable	Type	P	Amp	Max Epoch	$< M >$	$< I >$	A	$< g0 >$	M	$\Delta \log P$	Oo	[Fe/H]	err	Group
487671	ab	0.6273	1.19	3685.4094	18.09	18.03	0.13	17.90	0.494	0.061	II	-2.08	0.09	(A)
491136	ab	0.5877	0.73	3694.0059	16.92	16.89	0.14	16.75	0.540	-0.023	I	-1.87	0.05	(A)
491216	ab	0.5890	0.74	3678.7750	14.33	14.31	0.14	14.17	0.584	-0.021	I	-1.67	0.04	(A)
505091	ab	0.5310	1.32	3694.0821	17.57	17.50	0.12	17.38	0.596	0.004	I	-1.61	0.10	(A)
544842	abB	0.6180	0.51	3674.5884	15.61	15.60	0.11	15.49	0.625	-0.027	I	-1.47	0.28	(E)
552961	c	0.3364	0.51	3628.0744	15.84	15.82	0.12	15.71	0.689	NA	NA	-1.18	0.02	(F)
592459	ab	0.5834	1.01	3694.4436	19.92	19.88	0.13	19.75	0.570	0.008	I	-1.73	0.35	(E)
600979	ab	0.6368	1.01	3681.3225	16.85	16.80	0.18	16.62	0.424	0.046	II	-2.41	0.08	(C)
610690	ab	0.6390	1.06	3616.7131	17.61	17.56	0.11	17.45	0.497	0.052	II	-2.07	0.10	(D)
611171	ab	0.5816	0.90	3616.3926	15.74	15.70	0.19	15.51	0.641	-0.008	I	-1.40	0.09	(A)
62306	ab	0.6400	0.59	3679.2935	19.55	19.54	0.12	19.42	0.538	-0.003	I	-1.88	0.21	(D)
625655	c	0.2519	0.24	3626.5571	19.53	19.53	0.10	19.43	0.615	NA	NA	-1.52	0.55	(I)
636430	c	0.3786	0.51	3616.3346	17.58	17.57	0.09	17.48	0.529	NA	NA	-1.92	0.25	(F)
643347	ab	0.5879	0.83	3626.6055	17.89	17.86	0.09	17.77	0.608	-0.011	I	-1.55	0.14	(D)
66170	ab	0.6125	1.33	3637.3320	19.52	19.45	0.14	19.31	0.525	0.067	II	-1.94	0.11	(D)
675735	abB	0.3801	0.85	3679.1170	17.38	17.35	0.11	17.24	0.833	-0.198	I	-0.50	0.53	(E)

Table C.2: Photometric Properties of SDSS RRL (continued)

Variable	Type	P	Amp	Max Epoch	$< M >$	$< I >$	A	$< g0 >$	M	$\Delta \log P$	Oo	[Fe/H]	err	Group
683538	ab	0.6061	0.94	3679.6036	17.38	17.34	0.12	17.21	0.547	0.016	I	-1.84	0.07	(A)
708449	ab	0.5395	1.27	3676.2827	17.81	17.74	0.16	17.58	0.625	0.004	I	-1.47	0.09	(A)
738258	c	0.2695	0.42	3616.5302	15.39	15.38	0.10	15.28	0.652	NA	NA	-1.35	0.07	(F)
74164	ab	0.5730	1.02	3636.8795	15.44	15.39	0.19	15.19	0.495	0.000	I	-2.08	0.60	(B)
750838	c	0.3402	0.48	3681.4097	17.15	17.14	0.15	16.99	0.658	NA	NA	-1.32	0.04	(F)
78440	ab	0.7383	0.40	3628.1689	15.52	15.51	0.09	15.42	0.636	0.036	I	-1.42	0.27	(D)
791469	ab	0.6048	0.83	3684.0044	17.31	17.28	0.12	17.16	0.582	0.002	I	-1.67	0.06	(A)
799366	ab	0.6011	0.97	3681.2741	18.11	18.07	0.13	17.94	0.593	0.015	I	-1.62	0.07	(C)
80016	ab?	0.5095	0.97	3694.4513	18.95	18.91	0.09	18.82	0.651	-0.057	I	-1.35	0.40	(E)
802624	ab	0.5060	0.93	3319.3887	18.23	18.18	0.13	18.05	0.674	-0.064	I	-1.25	0.05	(C)
807309	ab	0.4998	1.52	3319.3986	17.49	17.39	0.09	17.30	0.613	0.002	I	-1.53	0.11	(D)
814336	ab	0.7978	0.48	3679.9247	15.99	15.98	0.13	15.85	0.549	0.080	II	-1.82	0.05	(A)
819279	ab	0.5654	1.14	3681.3599	17.80	17.75	0.13	17.63	0.664	0.009	I	-1.29	0.47	(B)
823034	ab	0.6023	0.77	3616.0629	17.84	17.82	0.13	17.69	0.529	-0.008	I	-1.92	0.24	(D)
833155	ab	0.6370	1.24	3319.2186	15.31	15.24	0.14	15.11	0.636	0.073	II	-1.42	0.03	(C)
833759	ab	0.5858	0.68	3679.3944	17.61	17.59	0.13	17.46	0.584	-0.031	I	-1.66	0.10	(A)

Table C.2: Photometric Properties of SDSS RRL (continued)

Variable	Type	P	Amp	Max Epoch	$< M >$	$< I >$	A	$< g0 >$	M	$\Delta \log P$	Oo	[Fe/H]	err	Group
852716	ab	0.5553	1.20	3681.5341	18.11	18.05	0.10	17.95	0.602	0.008	I	-1.58	0.07	(A)
859397	ab	0.7086	1.02	3679.6477	18.04	18.00	0.10	17.90	0.522	0.093	II	-1.96	0.08	(C)
86104	ab	0.5626	1.02	3684.9914	16.81	16.76	0.12	16.64	0.623	-0.008	I	-1.48	0.05	(C)
8668	ab	0.5480	1.09	3628.0375	17.85	17.79	0.11	17.68	0.618	-0.010	I	-1.51	0.08	(A)
870585	c	0.2843	0.50	3616.4161	17.07	17.06	0.10	16.96	0.615	NA	NA	-1.52	0.55	(I)
878096	ab	0.6374	0.64	3679.9334	17.42	17.40	0.10	17.30	0.558	0.002	I	-1.79	0.04	(A)
895587	ab	0.5638	1.14	3665.1723	17.36	17.31	0.09	17.22	0.661	0.008	I	-1.30	0.03	(C)
902052	ab	0.5577	1.19	3679.3785	17.55	17.49	0.09	17.40	0.605	0.009	I	-1.56	0.01	(C)
908314	abB	0.6304	1.03	3616.4098	18.06	18.01	0.10	17.91	0.512	0.043	I	-2.00	0.06	(C)
918395	ab	0.5521	1.34	3679.2350	18.27	18.19	0.10	18.09	0.570	0.022	I	-1.73	0.05	(C)
924895	ab	0.5941	0.95	3679.4296	18.15	18.11	0.10	18.01	0.655	0.008	I	-1.33	0.07	(A)
925246	ab	0.6466	0.67	3626.3988	18.21	18.19	0.10	18.08	0.675	0.011	I	-1.24	0.56	(D)
937681	ab	0.5154	1.44	3626.7440	18.38	18.29	0.12	18.17	0.578	0.005	I	-1.69	0.13	(D)
946940	ab	0.6767	0.91	3625.8607	17.16	17.12	0.10	17.02	0.425	0.060	II	-2.41	0.07	(A)
956269	ab	0.5134	1.43	3665.4388	16.95	16.86	0.11	16.75	0.608	0.002	I	-1.55	0.10	(D)
95875	c	0.3115	0.45	3626.3102	16.87	16.86	0.10	16.76	0.580	NA	NA	-1.68	0.02	(F)

Table C.2: Photometric Properties of SDSS RRL (continued)

Variable	Type	P	Amp	Max Epoch	$< M >$	$< I >$	A	$< g0 >$	M	$\Delta \log P$	Oo	[Fe/H]	err	Group
959039	ab	0.6393	1.05	3676.1152	17.49	17.44	0.11	17.33	0.551	0.052	II	-1.82	0.10	(D)
98085	ab	0.6319	0.58	3626.2307	15.68	15.66	0.12	15.54	0.671	-0.010	I	-1.26	0.01	(C)
982175	ab	0.5952	0.79	3626.1646	16.40	16.37	0.12	16.25	0.409	-0.010	I	-2.48	0.06	(A)
98405	ab	0.6123	0.69	3626.3487	18.19	18.17	0.12	18.05	0.572	-0.010	I	-1.72	0.15	(D)
990804	ab	0.7230	0.75	3627.8122	17.89	17.86	0.13	17.73	0.555	0.070	II	-1.80	0.12	(C)

Table C.3: Kinematic Properties of SDSS RRL

Variable	RA	Dec	l	b	Dist	Err	X	Y	Z	R	helio	lsr	gsr
1020340	34.7815	-0.0592	164.425	-55.701	31.15	0.34	24.907	4.712	-25.730	25.348	-130.143	-172.282	-138.996
1035856	35.2742	-0.6479	165.753	-55.879	14.28	1.00	15.762	1.971	-11.818	15.884	184.911	145.508	175.879
1051362	35.7877	0.9595	164.788	-54.284	29.15	0.16	24.419	4.465	-23.665	24.824	-121.231	-163.845	-130.147
1061424	36.1242	0.1238	166.117	-54.749	30.78	0.09	25.243	4.262	-25.132	25.601	-67.884	-107.447	-76.981
1068459	36.3477	0.6605	165.861	-54.187	27.90	0.26	23.831	3.988	-22.625	24.162	-114.724	-155.238	-123.792
1095893	37.2413	0.9000	166.811	-53.451	33.08	0.06	27.181	4.495	-26.577	27.551	-118.648	-157.751	-127.859
1097410	37.2911	1.0719	166.699	-53.285	18.42	0.15	18.715	2.533	-14.763	18.885	54.579	15.123	45.382
1103721	37.5083	-1.1963	169.426	-54.909	33.96	0.33	27.193	3.583	-27.789	27.428	-107.492	-140.248	-117.039
11194	0.3614	-0.2290	96.826	-60.542	6.51	0.31	8.381	3.180	-5.671	8.964	195.886	87.699	195.124
1132188	38.4422	-0.3171	169.672	-53.634	25.11	0.18	22.646	2.669	-20.218	22.803	-127.343	-160.341	-136.954
1152564	39.1476	0.5014	169.683	-52.554	31.22	0.15	26.674	3.399	-24.784	26.890	-95.734	-129.324	-105.368
1173512	39.8847	0.4472	170.654	-52.113	33.13	1.20	28.074	3.304	-26.146	28.268	-125.580	-157.301	-135.361
1191801	40.5090	0.6650	171.178	-51.537	20.66	0.09	20.701	1.971	-16.180	20.794	52.027	21.172	42.159
1194915	40.6129	1.2255	170.71	-51.048	8.00	0.02	12.965	0.812	-6.223	12.990	329.017	296.880	319.207
1233272	41.9387	0.6020	172.929	-50.621	25.76	0.33	24.221	2.012	-19.914	24.305	-140.728	-168.050	-150.868
1276299	43.5117	-0.4201	175.82	-50.261	4.22	0.23	10.691	0.197	-3.245	10.692	NA	NA	NA

Table C.3: Kinematic Properties of SDSS RRL (continued)

Variable	RA	Dec	l	b	Dist	Err	X	Y	Z	R	helio	lsr	gsr
128618	4.3154	1.0546	105.295	-60.641	8.08	0.27	9.045	3.821	-7.042	9.819	NA	NA	NA
1289027	43.9861	0.0982	175.768	-49.559	5.00	0.14	11.234	0.239	-3.805	11.237	NA	NA	NA
1295886	44.2429	-1.1551	177.441	-50.248	26.34	0.26	24.827	0.752	-20.251	24.838	NA	NA	NA
1298010	44.3229	0.7852	175.388	-48.835	36.07	0.18	31.668	1.909	-27.158	31.726	-107.016	-129.199	-117.556
1298437	44.3382	-0.2208	176.499	-49.532	17.67	0.96	19.446	0.700	-13.442	19.458	-62.431	-81.830	-73.111
1305932	44.6206	-0.6097	177.233	-49.599	28.83	0.52	26.662	0.902	-21.953	26.677	-145.447	-163.112	-156.228
1339969	45.8627	-0.6265	178.552	-48.705	5.96	0.32	11.932	0.099	-4.478	11.932	NA	NA	NA
1345269	46.0556	0.9745	177.006	-47.466	31.35	0.43	29.165	1.107	-23.101	29.186	NA	NA	NA
1345335	46.0575	-1.2206	179.418	-48.962	20.09	0.03	21.190	0.134	-15.154	21.191	-178.963	-191.539	-190.071
1390757	47.6093	0.4615	179.115	-46.682	10.00	0.10	14.860	0.106	-7.276	14.860	197.031	183.561	185.892
1428224	48.9078	-0.8950	181.847	-46.603	26.73	0.16	26.355	-0.592	-19.422	26.362	-135.912	-142.572	-147.444
1448542	310.5301	0.2553	46.621	-24.284	8.45	0.36	2.711	5.598	-3.475	6.219	174.723	39.676	185.429
1465359	310.6992	0.0645	46.533	-24.526	23.59	0.84	-6.764	15.576	-9.792	16.981	NA	NA	NA
1469597	310.7416	1.1712	47.604	-24.004	11.32	0.64	1.025	7.640	-4.607	7.708	178.440	40.811	189.231
1471053	310.7562	0.3343	46.821	-24.44	15.73	1.12	-1.796	10.440	-6.506	10.593	208.293	72.917	218.970
1507160	311.1271	-0.6546	46.083	-25.257	43.19	2.34	-19.093	28.138	-18.428	34.004	NA	NA	NA

Table C.3: Kinematic Properties of SDSS RRL (continued)

Variable	RA	Dec	l	b	Dist	Err	X	Y	Z	R	helio	lsr	gsr
1515202	311.2121	0.1889	46.936	-24.907	20.53	1.11	-4.714	13.604	-8.646	14.398	NA	NA	NA
1517082	311.2318	-0.3023	46.478	-25.171	12.70	0.56	0.085	8.334	-5.402	8.335	-168.404	-302.273	-157.897
153071	5.1462	1.2420	107.032	-60.674	7.78	0.22	9.116	3.643	-6.783	9.817	NA	NA	NA
1537496	311.4516	-1.0291	45.902	-25.724	13.21	0.74	-0.280	8.545	-5.732	8.549	203.065	71.098	213.433
1541097	311.4907	0.1106	47.016	-25.187	10.48	0.57	1.534	6.938	-4.460	7.105	NA	NA	NA
1541709	311.4970	-1.0015	45.954	-25.75	45.94	0.72	-20.768	29.742	-19.958	36.275	NA	NA	NA
1544422	311.5264	0.2880	47.205	-25.128	32.43	0.51	-11.947	21.545	-13.771	24.635	NA	NA	NA
1544490	311.5272	-0.1339	46.803	-25.342	18.06	0.98	-3.170	11.896	-7.728	12.311	-240.543	-375.012	-230.065
1546260	311.5465	-0.0426	46.901	-25.313	18.95	0.97	-3.704	12.508	-8.102	13.045	52.755	-81.973	63.242
1548226	311.5686	-0.3842	46.587	-25.503	34.39	1.86	-13.332	22.547	-14.807	26.194	NA	NA	NA
1549042	311.5774	-1.1855	45.821	-25.911	6.33	0.27	4.032	4.083	-2.766	5.739	126.996	-4.596	137.320
1551422	311.6035	1.1986	48.113	-24.731	22.74	1.23	-5.790	15.377	-9.514	16.431	52.440	-85.676	63.084
1552749	311.6179	0.7519	47.698	-24.972	13.33	0.72	-0.132	8.937	-5.627	8.938	133.002	-3.919	143.584
1560708	311.7055	0.0233	47.053	-25.417	13.47	0.73	-0.289	8.905	-5.781	8.910	NA	NA	NA
1561207	311.7113	-0.8988	46.171	-25.885	11.68	0.16	0.723	7.581	-5.099	7.615	NA	NA	NA
1570547	311.8150	0.5587	47.625	-25.24	7.84	1.00	3.220	5.239	-3.343	6.150	NA	NA	NA

Table C.3: Kinematic Properties of SDSS RRL (continued)

Variable	RA	Dec	l	b	Dist	Err	X	Y	Z	R	helio	lsr	gsr
1582235	311.9430	0.9055	48.027	-25.173	7.72	0.42	3.325	5.197	-3.285	6.170	24.847	-112.636	35.392
1593356	312.0620	0.1180	47.343	-25.676	9.89	0.09	1.963	6.552	-4.283	6.840	12.507	-122.893	22.924
1593719	312.0662	-0.9838	46.287	-26.235	18.89	1.02	-3.708	12.246	-8.350	12.796	-124.222	-256.595	-113.958
1599072	312.1271	-0.0738	47.196	-25.829	12.20	0.53	0.538	8.057	-5.316	8.075	256.305	121.399	266.684
1599155	312.1280	0.4455	47.693	-25.567	7.48	0.41	3.458	4.990	-3.228	6.071	NA	NA	NA
1600177	312.1390	-1.0887	46.226	-26.35	19.79	0.99	-4.267	12.804	-8.783	13.496	222.741	90.627	232.978
160083	5.3570	1.0063	107.334	-60.953	21.87	1.19	11.164	10.136	-19.119	15.079	NA	NA	NA
1616233	312.3188	-0.9668	46.444	-26.445	26.77	0.32	-8.516	17.370	-11.922	19.346	NA	NA	NA
1617275	312.3313	-1.2011	46.225	-26.573	7.91	0.41	3.105	5.108	-3.539	5.978	68.263	-63.623	78.450
1617477	312.3337	-1.0787	46.344	-26.513	17.22	0.75	-2.637	11.148	-7.687	11.456	NA	NA	NA
1621547	312.3810	-0.2398	47.18	-26.132	17.28	0.94	-2.546	11.381	-7.612	11.662	68.644	-65.919	78.955
1630498	312.4846	-1.1837	46.327	-26.697	12.64	0.57	0.202	8.168	-5.679	8.170	NA	NA	NA
1632111	312.5039	-0.7066	46.799	-26.474	31.71	0.29	-11.431	20.691	-14.136	23.639	-79.966	-213.295	-69.742
1632460	312.5078	1.2139	48.64	-25.499	15.86	0.77	-1.457	10.742	-6.826	10.840	84.562	-53.996	95.045
1634539	312.5322	-0.2832	47.223	-26.285	21.67	0.83	-5.195	14.261	-9.596	15.178	NA	NA	NA
1637388	312.5653	-0.1477	47.372	-26.245	7.86	0.02	3.224	5.189	-3.477	6.109	-330.518	-465.410	-320.228

Table C.3: Kinematic Properties of SDSS RRL (continued)

Variable	RA	Dec	l	b	Dist	Err	X	Y	Z	R	helio	lsr	gsr
1650675	312.7176	-1.1531	46.487	-26.883	27.90	0.49	-9.134	18.047	-12.616	20.227	NA	NA	NA
1653220	312.7480	-0.2077	47.418	-26.433	7.61	0.41	3.389	5.018	-3.388	6.055	93.083	-41.721	103.332
1682108	313.0878	0.1337	47.94	-26.551	71.02	2.66	-34.559	47.167	-31.746	58.473	NA	NA	NA
1689293	313.1742	1.1758	48.986	-26.089	39.45	1.09	-15.251	26.734	-17.349	30.778	NA	NA	NA
1689439	313.1760	-1.1648	46.734	-27.285	17.48	0.74	-2.648	11.312	-8.013	11.618	NA	NA	NA
1689618	313.1780	0.7752	48.606	-26.299	30.90	0.58	-10.317	20.781	-13.690	23.201	NA	NA	NA
1693414	313.2237	-0.6334	47.277	-27.058	3.24	0.13	6.042	2.120	-1.474	6.403	NA	NA	NA
1703145	313.3389	-0.3471	47.62	-27.012	22.80	1.24	-5.692	15.005	-10.355	16.048	NA	NA	NA
1708085	313.3992	-1.0761	46.947	-27.433	5.44	0.26	4.704	3.528	-2.506	5.880	93.602	-39.069	103.612
1716966	313.5075	-1.2325	46.856	-27.606	23.91	1.30	-6.489	15.460	-11.080	16.766	NA	NA	NA
1720341	313.5486	-0.5411	47.552	-27.292	48.24	2.28	-20.934	31.633	-22.119	37.933	NA	NA	NA
1727801	313.6397	-0.3449	47.794	-27.27	3.79	0.21	5.737	2.495	-1.737	6.256	NA	NA	NA
1731914	313.6921	0.2988	48.445	-26.985	15.23	0.63	-1.005	10.158	-6.912	10.208	-157.644	-294.204	-147.498
1743773	313.8386	-1.1797	47.096	-27.865	19.55	0.96	-3.767	12.661	-9.139	13.210	38.404	-94.144	48.320
1753291	313.9551	-0.8793	47.456	-27.813	24.02	0.36	-6.365	15.652	-11.207	16.897	NA	NA	NA
1770598	314.1674	1.0456	49.439	-27.005	8.81	0.62	2.898	5.961	-3.999	6.628	114.134	-24.622	124.292

Table C.3: Kinematic Properties of SDSS RRL (continued)

Variable	RA	Dec	l	b	Dist	Err	X	Y	Z	R	helio	lsr	gsr
1788251	314.3871	0.1979	48.751	-27.633	49.02	1.35	-20.634	32.652	-22.736	38.625	NA	NA	NA
1788975	314.3964	0.1496	48.71	-27.666	11.00	0.60	1.571	7.320	-5.107	7.487	NA	NA	NA
1791896	314.4326	-0.7472	47.86	-28.157	19.02	0.04	-3.251	12.434	-8.975	12.852	102.246	-31.714	112.112
1806631	314.6199	0.3532	49.037	-27.752	18.47	0.25	-2.716	12.343	-8.600	12.638	NA	NA	NA
1814238	314.7178	-0.9267	47.85	-28.494	26.85	1.46	-7.836	17.495	-12.809	19.170	NA	NA	NA
1817698	314.7627	0.8777	49.627	-27.601	16.67	0.61	-1.569	11.255	-7.723	11.364	NA	NA	NA
1834485	314.9802	-0.7122	48.213	-28.61	8.99	0.49	2.743	5.883	-4.303	6.491	48.319	-85.922	58.087
1838781	315.0362	0.4506	49.376	-28.057	17.08	0.24	-1.814	11.440	-8.034	11.583	NA	NA	NA
1839414	315.0442	-0.0581	48.888	-28.328	4.23	0.23	5.552	2.805	-2.007	6.220	NA	NA	NA
1843089	315.0911	0.7498	49.698	-27.947	25.29	0.75	-6.450	17.038	-11.852	18.218	NA	NA	NA
1845206	315.1188	0.1850	49.168	-28.266	8.28	0.45	3.230	5.520	-3.923	6.396	107.140	-29.605	117.005
1849535	315.1763	-0.0233	48.999	-28.423	33.90	1.17	-11.560	22.500	-16.136	25.296	NA	NA	NA
1854030	315.2377	0.2855	49.336	-28.315	40.74	0.52	-15.371	27.206	-19.324	31.248	NA	NA	NA
1854921	315.2496	0.6652	49.71	-28.127	17.93	0.95	-2.226	12.062	-8.453	12.266	74.314	-63.775	84.219
1854976	315.2505	-1.0849	48.005	-29.033	12.74	0.75	0.547	8.279	-6.183	8.297	-75.591	-208.885	-65.926
1856817	315.2750	0.5586	49.622	-28.204	8.79	0.74	2.984	5.899	-4.152	6.610	56.535	-81.274	66.421

Table C.3: Kinematic Properties of SDSS RRL (continued)

Variable	RA	Dec	l	b	Dist	Err	X	Y	Z	R	helio	lsr	gsr
1870663	315.4618	0.1564	49.343	-28.573	5.44	0.29	4.887	3.624	-2.602	6.085	-26.379	-163.154	-16.583
187796	6.2076	1.2156	109.137	-60.941	11.06	0.17	9.761	5.075	-9.668	11.002	NA	NA	NA
1879867	315.5866	0.8225	50.063	-28.331	8.79	0.41	3.031	5.935	-4.173	6.664	-157.090	-295.708	-147.227
1904451	315.9207	1.1109	50.542	-28.463	45.02	0.67	-17.152	30.558	-21.456	35.043	NA	NA	NA
1904545	315.9221	-0.4816	48.993	-29.298	75.02	2.00	-34.928	49.371	-36.711	60.477	NA	NA	NA
1908273	315.9742	0.1479	49.64	-29.015	34.66	0.85	-11.628	23.096	-16.811	25.858	NA	NA	NA
1914679	316.0632	-0.8890	48.676	-29.63	25.17	0.25	-6.447	16.431	-12.444	17.650	NA	NA	NA
1915855	316.0795	-0.4866	49.082	-29.435	31.70	0.11	-10.080	20.859	-15.576	23.167	7.593	-127.599	17.184
193232	6.3873	0.0067	108.964	-62.161	18.25	0.07	10.769	8.059	-16.136	13.451	-142.209	-241.626	-144.465
1933665	316.3329	1.1249	50.804	-28.805	45.10	0.62	-16.975	30.627	-21.731	35.017	NA	NA	NA
1943904	316.4785	0.2588	50.051	-29.386	17.00	0.85	-1.510	11.354	-8.341	11.454	-112.805	-250.144	-103.188
1949959	316.5659	-1.2470	48.621	-30.245	12.62	0.67	0.794	8.179	-6.356	8.218	-196.173	-329.388	-186.781
1950700	316.5765	-1.0255	48.847	-30.14	25.03	1.58	-6.243	16.296	-12.566	17.451	59.884	-73.949	69.305
1960101	316.7139	-0.8094	49.143	-30.145	16.57	0.88	-1.371	10.835	-8.319	10.921	-117.598	-252.065	-108.173
19601	0.6357	0.5686	97.952	-59.91	45.69	0.86	11.169	22.687	-39.533	25.287	NA	NA	NA
1962720	316.7525	-0.6645	49.31	-30.103	14.98	0.63	-0.449	9.827	-7.513	9.837	NA	NA	NA

Table C.3: Kinematic Properties of SDSS RRL (continued)

Variable	RA	Dec	l	b	Dist	Err	X	Y	Z	R	helio	lsr	gsr
1968253	316.8355	-0.0703	49.945	-29.863	5.57	0.19	4.890	3.699	-2.774	6.132	-54.326	-190.857	-44.823
1978304	316.9856	0.0263	50.13	-29.94	7.55	0.51	3.805	5.022	-3.769	6.301	34.287	-102.543	43.774
1979749	317.0064	0.7013	50.803	-29.6	19.12	1.04	-2.507	12.884	-9.444	13.125	NA	NA	NA
1984658	317.0777	-0.3054	49.86	-30.192	25.95	1.41	-6.460	17.147	-13.050	18.323	NA	NA	NA
1987864	317.1256	-0.2315	49.962	-30.194	7.98	0.33	3.563	5.281	-4.013	6.370	NA	NA	NA
2007031	317.4116	-1.1050	49.271	-30.895	9.71	0.40	2.566	6.311	-4.983	6.813	108.461	-25.352	117.710
2008263	317.4298	0.4104	50.778	-30.114	8.99	0.47	3.080	6.028	-4.513	6.769	181.671	43.692	191.123
2015807	317.5428	1.1566	51.576	-29.81	4.95	0.27	5.331	3.365	-2.461	6.304	NA	NA	NA
2021819	317.6341	0.5880	51.078	-30.192	5.20	0.28	5.176	3.497	-2.615	6.247	NA	NA	NA
2021917	317.6356	0.9179	51.401	-30.017	12.76	0.69	1.105	8.638	-6.385	8.708	-120.434	-259.830	-110.953
2022188	317.6397	-1.2485	49.266	-31.164	22.20	0.26	-4.396	14.394	-11.488	15.051	NA	NA	NA
2028388	317.7285	-0.1582	50.403	-30.668	15.98	0.61	-0.761	10.591	-8.151	10.618	NA	NA	NA
2035884	317.8420	-0.6612	49.974	-31.03	43.29	0.42	-15.858	28.406	-22.316	32.533	-195.002	-330.134	-185.777
2036397	317.8504	-0.4374	50.201	-30.919	25.23	0.30	-5.855	16.629	-12.964	17.630	NA	NA	NA
2041986	317.9371	1.1712	51.835	-30.135	11.33	0.70	1.946	7.704	-5.688	7.945	-166.576	-306.715	-157.121
2042971	317.9530	0.6789	51.364	-30.413	10.92	0.51	2.118	7.359	-5.530	7.658	-39.048	-177.864	-29.662

Table C.3: Kinematic Properties of SDSS RRL (continued)

Variable	RA	Dec	l	b	Dist	Err	X	Y	Z	R	helio	lsr	gsr
2045615	317.9942	-0.2242	50.501	-30.929	11.12	0.49	1.934	7.359	-5.714	7.609	-164.649	-301.014	-155.393
2055722	318.1524	-1.2252	49.602	-31.589	15.75	0.92	-0.697	10.220	-8.252	10.244	198.538	64.906	207.625
2056564	318.1654	0.9163	51.729	-30.464	13.84	0.83	0.613	9.363	-7.015	9.383	158.295	18.796	167.672
2074459	318.4479	-0.2707	50.736	-31.338	24.65	0.32	-5.325	16.301	-12.820	17.148	NA	NA	NA
2075021	318.4571	0.2627	51.269	-31.061	11.44	0.54	1.869	7.644	-5.902	7.869	-42.907	-180.689	-33.676
2077610	318.4986	-0.7897	50.251	-31.656	21.43	0.09	-3.663	14.024	-11.246	14.495	193.131	58.228	202.209
2084910	318.6128	-0.5699	50.541	-31.636	18.31	0.07	-1.910	12.039	-9.606	12.190	-35.774	-171.304	-26.687
2096118	318.7893	0.5117	51.723	-31.208	27.80	1.81	-6.728	18.664	-14.403	19.839	-282.136	-420.652	-272.938
2107186	318.9583	0.3248	51.645	-31.451	34.50	1.87	-10.263	23.080	-18.001	25.259	NA	NA	NA
2122667	319.1954	1.2209	52.677	-31.165	22.32	1.21	-3.580	15.188	-11.551	15.604	NA	NA	NA
2125070	319.2335	-1.2420	50.254	-32.518	25.88	1.02	-5.953	16.779	-13.912	17.804	NA	NA	NA
2126870	319.2632	0.9343	52.439	-31.378	38.39	0.61	-11.980	25.981	-19.989	28.610	NA	NA	NA
2127489	319.2727	-0.9988	50.524	-32.423	6.91	0.37	4.292	4.502	-3.704	6.220	88.664	-45.785	97.559
2135439	319.4005	0.1955	51.797	-31.893	11.00	0.60	2.227	7.336	-5.809	7.666	-26.897	-164.646	-17.864
2140120	319.4763	-0.2822	51.37	-32.214	18.18	0.07	-1.603	12.016	-9.692	12.122	10.997	-125.457	19.950
2148716	319.6118	0.5087	52.242	-31.902	14.04	0.12	0.701	9.424	-7.420	9.450	144.331	5.703	153.364

Table C.3: Kinematic Properties of SDSS RRL (continued)

Variable	RA	Dec	l	b	Dist	Err	X	Y	Z	R	helio	lsr	gsr
2163750	319.8520	0.5377	52.425	-32.087	13.62	0.11	0.963	9.146	-7.235	9.197	90.867	-47.871	99.856
217320	7.1882	0.5394	110.862	-61.8	12.91	0.08	10.173	5.702	-11.380	11.662	131.116	31.585	128.731
2179468	320.1110	1.2033	53.249	-31.94	25.54	0.96	-4.968	17.366	-13.511	18.062	NA	NA	NA
2181657	320.1461	-0.7142	51.363	-33.011	10.43	0.61	2.538	6.834	-5.684	7.290	170.644	35.299	179.403
2192592	320.3265	-0.9709	51.219	-33.301	26.89	0.34	-6.077	17.520	-14.764	18.544	NA	NA	NA
2194097	320.3516	0.7883	52.995	-32.369	20.03	0.02	-2.181	13.508	-10.721	13.683	-80.291	-219.758	-71.369
2200232	320.4533	-0.6102	51.664	-33.214	6.32	0.35	4.723	4.144	-3.459	6.283	73.173	-62.489	81.884
2202958	320.4983	-1.0436	51.255	-33.485	20.81	0.80	-2.861	13.534	-11.479	13.833	-24.662	-159.128	-16.020
2205327	320.5370	0.2787	52.609	-32.803	19.36	1.43	-1.879	12.926	-10.486	13.062	-154.690	-292.795	-145.875
2211741	320.6393	-1.0838	51.305	-33.625	21.44	0.74	-3.161	13.934	-11.873	14.288	NA	NA	NA
2229203	320.9300	0.6325	53.218	-32.938	8.16	0.49	3.898	5.486	-4.438	6.730	244.219	105.123	253.002
2240050	321.1134	0.8744	53.579	-32.957	9.82	0.01	3.109	6.629	-5.341	7.322	91.141	-48.622	99.919
2242178	321.1491	0.5239	53.254	-33.18	18.90	1.02	-1.462	12.673	-10.342	12.758	-183.777	-322.597	-175.054
2248863	321.2613	-0.1945	52.608	-33.668	17.33	0.79	-0.759	11.459	-9.607	11.484	74.091	-62.777	82.694
2250063	321.2821	-0.7990	52.01	-34.014	11.28	0.03	2.244	7.370	-6.311	7.704	-234.780	-369.985	-226.265
2253693	321.3432	0.3250	53.183	-33.452	26.90	1.22	-5.450	17.968	-14.828	18.776	NA	NA	NA

Table C.3: Kinematic Properties of SDSS RRL (continued)

Variable	RA	Dec	l	b	Dist	Err	X	Y	Z	R	helio	lsr	gsr
2255955	321.3830	-1.1294	51.74	-34.277	22.29	1.21	-3.405	14.463	-12.554	14.858	NA	NA	NA
2269900	321.6190	0.0465	53.086	-33.835	49.27	0.58	-16.581	32.722	-27.434	36.683	NA	NA	NA
2275534	321.7144	0.0889	53.192	-33.892	26.42	0.83	-5.142	17.562	-14.735	18.299	185.484	47.818	194.032
2279117	321.7772	0.5171	53.663	-33.708	26.48	0.29	-5.052	17.745	-14.695	18.450	NA	NA	NA
2286970	321.9126	1.2015	54.436	-33.439	8.08	0.04	4.077	5.487	-4.454	6.836	31.229	-109.453	39.886
2288071	321.9325	-1.1974	52.03	-34.776	17.24	0.04	-0.714	11.165	-9.835	11.188	235.036	100.906	243.362
2291454	321.9920	-0.4402	52.841	-34.414	45.75	0.15	-14.798	30.080	-25.857	33.523	-84.816	-221.042	-76.397
2303228	322.2006	0.9570	54.386	-33.814	36.41	1.29	-9.616	24.593	-20.262	26.406	NA	NA	NA
2303487	322.2050	0.5319	53.964	-34.055	33.02	0.28	-8.095	22.123	-18.492	23.558	28.712	-110.174	37.219
2314353	322.3902	-0.7250	52.817	-34.903	7.00	0.48	4.530	4.575	-4.006	6.438	148.308	12.856	156.604
2319786	322.4794	1.0066	54.624	-34.017	4.42	0.20	5.879	2.987	-2.473	6.594	NA	NA	NA
2325897	322.5874	1.0044	54.695	-34.108	12.40	0.67	2.067	8.378	-6.953	8.629	-26.965	-167.130	-18.475
2328485	322.6328	-0.5125	53.196	-34.99	5.14	0.12	5.477	3.372	-2.947	6.432	NA	NA	NA
2338371	322.8062	0.9875	54.827	-34.298	13.63	0.09	1.515	9.202	-7.679	9.326	-3.758	-143.878	4.684
2346078	322.9465	0.2441	54.176	-34.831	22.19	0.18	-2.662	14.770	-12.675	15.008	9.722	-128.388	18.034
2361466	323.2179	0.9357	55.057	-34.667	13.22	0.68	1.773	8.912	-7.519	9.087	-48.796	-188.772	-40.448

Table C.3: Kinematic Properties of SDSS RRL (continued)

Variable	RA	Dec	l	b	Dist	Err	X	Y	Z	R	helio	lsr	gsr
2367759	323.3084	-1.0182	53.134	-35.832	10.69	0.05	2.800	6.934	-6.258	7.478	123.417	-11.217	131.480
2371159	323.3676	-0.2983	53.912	-35.483	36.22	1.61	-9.372	23.834	-21.024	25.611	NA	NA	NA
2371287	323.3699	1.2083	55.435	-34.637	9.19	0.02	3.711	6.225	-5.222	7.247	186.138	45.433	194.491
2376453	323.4540	-0.7626	53.495	-35.812	11.74	0.28	2.336	7.653	-6.869	8.001	NA	NA	NA
237692	7.8303	0.8488	112.309	-61.607	54.58	0.65	17.852	24.011	-48.014	29.920	NA	NA	NA
2377638	323.4712	-0.7991	53.47	-35.847	10.95	0.09	2.717	7.132	-6.412	7.632	149.265	14.029	157.324
2408962	324.0460	0.7254	55.42	-35.468	15.78	0.93	0.704	10.584	-9.158	10.607	132.642	-6.735	140.787
2411556	324.0966	-0.4021	54.307	-36.146	10.61	0.02	3.003	6.957	-6.257	7.577	-202.608	-338.909	-194.626
2423189	324.3254	0.9502	55.843	-35.569	14.94	1.27	1.176	10.057	-8.691	10.126	107.733	-32.234	115.848
2425905	324.3793	-0.5347	54.367	-36.454	7.49	0.36	4.489	4.898	-4.452	6.644	-43.278	-179.197	-35.375
2441045	324.6886	0.3923	55.534	-36.186	32.26	0.49	-6.733	21.463	-19.044	22.495	51.804	-86.627	59.767
2455878	324.9910	0.8956	56.259	-36.145	28.16	0.28	-4.631	18.910	-16.610	19.468	NA	NA	NA
2464378	325.1669	0.7695	56.257	-36.362	27.20	0.48	-4.167	18.214	-16.126	18.684	NA	NA	NA
2469472	325.2674	-0.8710	54.642	-37.378	25.37	0.35	-3.666	16.442	-15.401	16.846	NA	NA	NA
2478738	325.4574	1.0229	56.722	-36.452	22.67	1.23	-2.004	15.243	-13.468	15.374	-22.620	-162.677	-14.737
2478919	325.4608	1.1849	56.889	-36.361	14.24	0.56	1.736	9.605	-8.442	9.761	NA	NA	NA

Table C.3: Kinematic Properties of SDSS RRL (continued)

Variable	RA	Dec	l	b	Dist	Err	X	Y	Z	R	helio	lsr	gsr
2480640	325.4954	-0.1254	55.577	-37.144	40.91	1.37	-10.434	26.900	-24.702	28.853	NA	NA	NA
2483003	325.5452	-0.8009	54.913	-37.568	23.41	0.65	-2.666	15.184	-14.273	15.416	NA	NA	NA
2510603	326.1165	-0.0430	56.109	-37.606	5.63	0.28	5.515	3.700	-3.433	6.641	-79.112	-216.194	-71.516
2510616	326.1168	0.4003	56.566	-37.35	16.00	0.12	0.994	10.611	-9.704	10.658	-158.172	-296.464	-150.517
2512234	326.1506	-1.1040	55.029	-38.239	12.43	0.89	2.405	7.999	-7.692	8.353	35.456	-98.698	42.899
2518975	326.2858	-0.3557	55.908	-37.924	17.26	0.94	0.369	11.274	-10.607	11.280	157.927	21.726	165.443
2526240	326.4407	-0.3184	56.06	-38.029	15.55	0.17	1.160	10.163	-9.581	10.229	-40.272	-176.552	-32.784
2530960	326.5403	0.0988	56.565	-37.87	25.86	0.25	-3.248	17.036	-15.875	17.343	NA	NA	NA
2539586	326.7231	0.5106	57.124	-37.78	28.80	1.11	-4.356	19.117	-17.644	19.607	NA	NA	NA
2545670	326.8523	-0.8845	55.769	-38.691	18.60	0.60	-0.165	12.000	-11.624	12.001	-5.639	-140.290	1.681
2547187	326.8870	0.3518	57.082	-38.005	14.66	0.61	1.724	9.694	-9.024	9.846	-81.361	-219.399	-73.880
2553011	327.0176	1.1202	57.966	-37.66	17.78	0.25	0.533	11.934	-10.865	11.946	-4.056	-144.144	3.500
2554564	327.0522	1.0633	57.934	-37.721	17.01	0.25	0.857	11.402	-10.407	11.434	NA	NA	NA
2555926	327.0826	-0.6032	56.234	-38.718	60.31	1.78	-18.154	39.118	-37.723	43.125	NA	NA	NA
2563997	327.2670	0.4623	57.478	-38.249	22.73	0.38	-1.597	15.051	-14.072	15.136	NA	NA	NA
2584203	327.7317	1.2549	58.641	-38.154	8.04	0.35	4.709	5.401	-4.969	7.165	-31.073	-171.384	-23.657

Table C.3: Kinematic Properties of SDSS RRL (continued)

Variable	RA	Dec	l	b	Dist	Err	X	Y	Z	R	helio	lsr	gsr
2585370	327.7604	-0.3170	57.038	-39.105	29.85	0.69	-4.604	19.437	-18.830	19.975	-113.932	-249.972	-106.735
2599429	328.1038	0.7746	58.432	-38.739	26.06	0.10	-2.642	17.320	-16.309	17.520	81.197	-57.740	88.467
2604319	328.2203	-0.9122	56.758	-39.825	16.87	0.29	0.896	10.838	-10.806	10.875	-240.177	-374.476	-233.164
2617725	328.5364	1.0310	59.028	-38.932	14.00	0.15	2.395	9.339	-8.799	9.641	128.476	-11.052	135.683
2623071	328.6496	-0.9143	57.082	-40.175	27.01	0.21	-3.217	17.327	-17.428	17.624	-7.691	-141.882	-0.773
2628577	328.7730	-0.7031	57.4	-40.152	65.83	3.57	-19.109	42.389	-42.448	46.497	NA	NA	NA
26293	0.8468	-0.9942	97.133	-61.436	12.41	0.04	8.737	5.888	-10.900	10.536	148.077	42.711	147.088
263605	8.6869	0.9058	114.111	-61.68	6.23	0.35	9.208	2.700	-5.488	9.596	14.662	-83.310	11.951
2638641	329.0084	0.2934	58.63	-39.752	4.89	0.14	6.042	3.212	-3.129	6.842	35.806	-101.607	42.809
2646637	329.1994	-1.0824	57.325	-40.72	24.68	0.44	-2.100	15.747	-16.102	15.886	5.892	-127.688	12.664
2651617	329.3222	-0.0620	58.502	-40.216	43.11	0.81	-9.200	28.070	-27.836	29.540	59.703	-76.656	66.587
2652576	329.3454	-0.9797	57.548	-40.778	6.97	0.38	5.167	4.456	-4.554	6.823	130.589	-3.237	137.342
2655720	329.4174	0.2851	58.941	-40.084	13.02	0.59	2.861	8.533	-8.384	9.000	116.341	-20.940	123.251
2659778	329.5092	-0.9154	57.744	-40.872	9.64	0.51	4.108	6.166	-6.310	7.410	-45.726	-179.685	-39.000
2660264	329.5201	1.0298	59.795	-39.717	18.30	1.08	0.919	12.164	-11.692	12.199	154.381	15.117	161.368
2676003	329.8862	-0.7403	58.226	-41.073	20.84	1.13	-0.273	13.356	-13.692	13.359	NA	NA	NA

Table C.3: Kinematic Properties of SDSS RRL (continued)

Variable	RA	Dec	l	b	Dist	Err	X	Y	Z	R	helio	lsr	gsr
2686883	330.1378	1.1243	60.384	-40.148	3.96	0.16	6.502	2.635	-2.556	7.016	78.994	-60.339	85.855
2701634	330.4859	1.1987	60.742	-40.377	29.00	1.57	-2.797	19.274	-18.787	19.476	NA	NA	NA
2706750	330.6013	0.4457	60.051	-40.93	9.52	0.44	4.409	6.232	-6.237	7.634	NA	NA	NA
270817	8.9290	0.9316	114.624	-61.686	22.28	0.14	12.404	9.608	-19.618	15.690	171.388	73.763	168.621
2716972	330.8482	0.8296	60.653	-40.889	5.79	0.27	5.855	3.815	-3.790	6.988	NA	NA	NA
2718789	330.8925	-0.5268	59.257	-41.751	32.78	0.65	-4.501	21.019	-21.828	21.495	NA	NA	NA
2720649	330.9379	-0.5379	59.282	-41.794	40.79	0.91	-7.536	26.147	-27.188	27.211	-171.153	-305.706	-164.700
2726067	331.0703	0.9650	60.975	-40.981	15.78	0.72	2.220	10.417	-10.349	10.651	NA	NA	NA
2728156	331.1240	-0.6969	59.262	-42.038	14.82	0.72	2.375	9.459	-9.923	9.753	-193.180	-327.231	-186.791
2741575	331.4718	0.4668	60.784	-41.604	12.70	0.58	3.365	8.288	-8.432	8.945	-2.082	-139.192	4.386
2743740	331.5301	-0.7711	59.514	-42.407	4.25	0.20	6.409	2.702	-2.864	6.956	141.665	7.966	147.951
2744412	331.5474	0.0781	60.436	-41.903	48.51	0.67	-9.814	31.404	-32.398	32.902	NA	NA	NA
2745760	331.5814	-0.6518	59.684	-42.375	34.67	0.38	-4.928	22.110	-23.367	22.653	NA	NA	NA
2747989	331.6370	0.8606	61.334	-41.49	5.77	0.40	5.927	3.791	-3.821	7.036	-0.413	-138.526	6.071
2753811	331.7845	-0.3002	60.229	-42.322	38.23	2.07	-6.035	24.536	-25.740	25.267	NA	NA	NA
2762264	331.9933	-0.3227	60.378	-42.501	10.60	0.63	4.138	6.792	-7.160	7.953	-14.710	-149.469	-8.469

Table C.3: Kinematic Properties of SDSS RRL (continued)

Variable	RA	Dec	l	b	Dist	Err	X	Y	Z	R	helio	lsr	gsr
2763274	332.0190	-1.0551	59.609	-42.968	31.70	0.50	-3.735	20.009	-21.606	20.354	NA	NA	NA
2764164	332.0416	0.4099	61.197	-42.087	57.46	1.02	-12.545	37.367	-38.513	39.417	NA	NA	NA
2766251	332.0933	1.0836	61.948	-41.707	27.86	0.24	-1.782	18.356	-18.537	18.443	-69.983	-208.521	-63.574
2781708	332.4832	-0.6473	60.438	-43.087	13.37	0.11	3.184	8.491	-9.130	9.068	-48.326	-181.996	-42.242
2788149	332.6503	1.1487	62.487	-42.098	58.72	1.85	-12.127	38.643	-39.366	40.501	NA	NA	NA
2794135	332.8055	-0.3875	60.991	-43.181	21.35	0.67	0.450	13.615	-14.610	13.623	NA	NA	NA
2794423	332.8128	-0.0086	61.404	-42.951	52.87	2.87	-10.522	33.977	-36.024	35.569	NA	NA	NA
2800504	332.9693	0.6330	62.219	-42.671	17.79	0.04	1.903	11.573	-12.059	11.729	-50.788	-187.754	-44.642
2801516	332.9942	0.1922	61.773	-42.967	14.25	0.77	3.068	9.187	-9.712	9.686	NA	NA	NA
2801989	333.0055	-0.0573	61.516	-43.132	27.33	0.20	-1.511	17.529	-18.683	17.594	27.227	-107.846	33.271
2803055	333.0312	-1.1356	60.37	-43.819	18.34	0.20	1.458	11.502	-12.698	11.594	NA	NA	NA
2805929	333.0984	0.0825	61.745	-43.117	12.21	0.08	3.780	7.852	-8.347	8.715	-76.093	-211.509	-70.052
2814984	333.3202	-0.5376	61.268	-43.677	17.39	0.23	1.953	11.031	-12.012	11.203	32.123	-101.495	38.029
2835133	333.8331	-0.6168	61.626	-44.128	61.74	2.37	-13.060	38.992	-42.987	41.121	NA	NA	NA
2839664	333.9589	-0.6392	61.711	-44.24	36.58	0.72	-4.420	23.077	-25.521	23.496	NA	NA	NA
2858234	334.4708	-0.0931	62.754	-44.293	5.58	0.30	6.172	3.549	-3.895	7.120	-103.800	-238.103	-98.103

Table C.3: Kinematic Properties of SDSS RRL (continued)

Variable	RA	Dec	l	b	Dist	Err	X	Y	Z	R	helio	lsr	gsr
2858731	334.4830	-1.1186	61.646	-44.949	18.89	0.20	1.651	11.764	-13.344	11.880	-167.318	-298.786	-161.764
286700	9.4540	-0.0533	115.483	-62.728	62.83	0.87	20.387	25.989	-55.846	33.031	NA	NA	NA
2869752	334.7774	-0.0558	63.067	-44.506	40.23	0.48	-4.996	25.579	-28.201	26.062	NA	NA	NA
2870122	334.7871	-0.8929	62.164	-45.044	56.78	0.73	-10.733	35.476	-40.180	37.065	NA	NA	NA
2888418	335.2607	0.4426	64.039	-44.555	5.48	0.30	6.291	3.511	-3.845	7.204	NA	NA	NA
2890944	335.3224	1.0881	64.78	-44.182	26.40	0.39	-0.067	17.128	-18.399	17.128	NA	NA	NA
2894713	335.4151	0.8333	64.596	-44.418	12.15	0.55	4.277	7.839	-8.504	8.930	-136.019	-272.359	-130.418
28977	0.9357	1.1159	98.905	-59.513	18.65	0.12	9.464	9.346	-16.069	13.301	-33.320	-144.314	-34.044
2900805	335.5636	1.0138	64.923	-44.413	24.64	0.36	0.540	15.942	-17.244	15.951	NA	NA	NA
2912876	335.8599	0.3691	64.509	-45.058	14.72	0.17	3.524	9.388	-10.421	10.027	28.988	-105.857	34.420
2921362	336.0752	0.7833	65.151	-44.95	19.62	0.66	2.165	12.600	-13.861	12.785	NA	NA	NA
2927712	336.2300	0.0449	64.502	-45.55	19.96	1.08	1.983	12.616	-14.249	12.771	NA	NA	NA
2930308	336.2951	-0.9227	63.503	-46.226	83.10	1.06	-17.649	51.451	-60.004	54.394	NA	NA	NA
2930888	336.3096	-0.1050	64.414	-45.708	11.77	0.11	4.450	7.414	-8.425	8.647	-44.316	-177.618	-39.054
2932935	336.3634	-0.3015	64.25	-45.877	22.55	1.22	1.179	14.140	-16.187	14.189	NA	NA	NA
2940701	336.5680	-0.2279	64.522	-45.985	4.46	0.22	6.667	2.798	-3.207	7.230	NA	NA	NA

Table C.3: Kinematic Properties of SDSS RRL (continued)

Variable	RA	Dec	l	b	Dist	Err	X	Y	Z	R	helio	lsr	gsr
2953315	336.8941	-0.6325	64.385	-46.496	21.50	1.17	1.601	13.346	-15.595	13.442	NA	NA	NA
2960182	337.0724	-0.9885	64.159	-46.862	4.98	0.25	6.517	3.063	-3.632	7.201	59.765	-70.661	64.724
2964169	337.1797	-0.8542	64.411	-46.857	6.91	0.33	5.959	4.263	-5.043	7.326	79.625	-51.108	84.576
2965347	337.2122	-1.1536	64.108	-47.076	4.99	0.27	6.516	3.057	-3.654	7.198	NA	NA	NA
2983558	337.7183	1.2388	67.196	-45.869	14.07	0.76	4.202	9.033	-10.101	9.963	182.473	46.367	187.580
2984333	337.7392	-0.0564	65.826	-46.753	14.70	0.18	3.877	9.186	-10.705	9.970	82.794	-49.793	87.721
2985501	337.7718	0.0939	66.022	-46.678	19.01	0.97	2.699	11.918	-13.831	12.220	186.915	53.939	191.855
2998988	338.1424	0.6016	66.932	-46.612	19.19	0.31	2.836	12.126	-13.943	12.453	123.602	-10.521	128.521
2999145	338.1472	-1.0279	65.15	-47.702	4.22	0.18	6.806	2.579	-3.123	7.278	128.419	-1.234	133.115
3002611	338.2418	0.0774	66.463	-47.038	51.57	1.07	-6.035	32.222	-37.739	32.782	NA	NA	NA
3006489	338.3516	0.5581	67.091	-46.796	25.61	0.05	1.175	16.149	-18.667	16.192	119.752	-14.117	124.615
3010656	338.4692	0.7650	67.43	-46.742	31.54	0.38	-0.294	19.956	-22.967	19.958	-253.464	-387.817	-248.601
3012156	338.5111	-0.2904	66.326	-47.485	20.85	0.33	2.341	12.907	-15.372	13.118	126.761	-4.691	131.470
3013503	338.5484	-1.0230	65.55	-48	20.26	0.26	2.389	12.341	-15.056	12.570	NA	NA	NA
3022511	338.8118	-0.4070	66.497	-47.786	18.84	1.02	2.952	11.608	-13.954	11.978	NA	NA	NA
3023484	338.8389	-0.7978	66.09	-48.067	36.73	0.36	-1.948	22.439	-27.324	22.523	NA	NA	NA

Table C.3: Kinematic Properties of SDSS RRL (continued)

Variable	RA	Dec	l	b	Dist	Err	X	Y	Z	R	helio	lsr	gsr
3025286	338.8932	-1.2406	65.648	-48.402	26.13	0.03	0.846	15.806	-19.543	15.829	12.363	-116.213	16.850
3034077	339.1423	-0.6136	66.6	-48.17	13.11	0.65	4.528	8.024	-9.769	9.213	17.306	-112.837	21.818
3041792	339.3636	0.2199	67.74	-47.768	16.64	0.18	3.763	10.351	-12.321	11.014	NA	NA	NA
3057986	339.8270	-0.7474	67.147	-48.765	76.95	2.81	-11.699	46.740	-57.867	48.182	NA	NA	NA
3058946	339.8535	-0.0742	67.919	-48.326	20.48	0.06	2.880	12.620	-15.300	12.945	64.047	-67.086	68.462
3065604	340.0505	-0.2535	67.925	-48.593	38.55	0.29	-1.582	23.627	-28.912	23.680	-201.738	-332.238	-197.396
3069481	340.1679	-1.1189	67.082	-49.268	75.96	1.95	-11.301	45.653	-57.560	47.031	NA	NA	NA
3082830	340.5650	-0.6741	67.995	-49.256	17.70	0.18	3.671	10.712	-13.411	11.323	86.569	-42.401	90.728
3089339	340.7504	-1.2324	67.562	-49.773	17.27	0.32	3.743	10.309	-13.186	10.967	NA	NA	NA
3096217	340.9491	0.5003	69.691	-48.719	36.48	0.50	-0.354	22.572	-27.414	22.574	NA	NA	NA
3100068	341.0594	-0.1816	69.064	-49.274	26.48	0.94	1.827	16.136	-20.068	16.239	NA	NA	NA
3104441	341.1768	-1.1255	68.135	-50.011	69.73	4.12	-8.689	41.588	-53.425	42.486	NA	NA	NA
3120139	341.6137	-0.2740	69.557	-49.735	21.38	0.27	3.174	12.948	-16.314	13.331	85.016	-44.262	88.974
3132461	341.9639	-1.2485	68.846	-50.665	18.65	0.33	3.734	11.025	-14.425	11.640	NA	NA	NA
3134228	342.0143	-0.0314	70.261	-49.85	38.85	0.57	-0.460	23.578	-29.695	23.583	NA	NA	NA
3140488	342.2037	1.1118	71.703	-49.167	8.87	0.23	6.179	5.506	-6.711	8.277	NA	NA	NA

Table C.3: Kinematic Properties of SDSS RRL (continued)

Variable	RA	Dec	l	b	Dist	Err	X	Y	Z	R	helio	lsr	gsr
314320	10.3568	1.1498	117.662	-61.619	22.88	0.18	13.048	9.631	-20.127	16.218	-67.059	-162.773	-70.152
3154303	342.6094	-0.4601	70.445	-50.573	54.35	2.95	-3.553	32.526	-41.982	32.720	NA	NA	NA
3156028	342.6613	1.1222	72.221	-49.476	37.31	2.02	0.598	23.085	-28.361	23.093	NA	NA	NA
3156554	342.6780	-0.1289	70.888	-50.386	14.78	0.20	4.914	8.904	-11.386	10.171	NA	NA	NA
3200435	344.0880	-0.5741	72.005	-51.688	6.21	0.34	6.811	3.662	-4.873	7.733	NA	NA	NA
320052	10.5518	-0.7143	117.756	-63.493	18.37	0.14	11.819	7.257	-16.442	13.869	133.260	42.975	129.865
3208965	344.3475	-0.8127	72.041	-52.04	16.72	0.92	4.829	9.783	-13.182	10.910	-12.769	-138.290	-9.559
3211444	344.4255	0.4653	73.539	-51.16	67.73	1.00	-4.036	40.736	-52.755	40.935	NA	NA	NA
3215255	344.5388	0.8713	74.107	-50.936	10.46	0.03	6.195	6.341	-8.123	8.864	-6.088	-136.039	-2.697
3225128	344.8333	0.1370	73.666	-51.677	28.88	0.08	2.963	17.186	-22.657	17.439	40.875	-86.821	44.093
3244819	345.4276	-1.1278	72.978	-53.01	16.44	0.86	5.105	9.456	-13.128	10.746	-54.620	-178.292	-51.722
325148	10.7274	0.2993	118.311	-62.496	16.96	0.09	11.714	6.895	-15.042	13.593	15.226	-77.521	11.925
3285218	346.6152	-0.2443	75.431	-53.148	11.17	0.02	6.314	6.486	-8.941	9.052	-25.488	-150.468	-22.766
3301492	347.0965	0.1907	76.512	-53.13	53.51	2.90	0.512	31.221	-42.808	31.225	NA	NA	NA
3308107	347.2903	0.6365	77.234	-52.912	17.37	0.31	5.685	10.216	-13.856	11.691	NA	NA	NA
3309727	347.3370	1.0993	77.779	-52.584	7.36	0.33	7.054	4.368	-5.842	8.297	-71.158	-199.076	-68.434

Table C.3: Kinematic Properties of SDSS RRL (continued)

Variable	RA	Dec	l	b	Dist	Err	X	Y	Z	R	helio	lsr	gsr
3312938	347.4313	-0.4886	76.203	-53.865	26.71	0.20	4.244	15.294	-21.568	15.872	-211.141	-334.646	-208.657
3321123	347.6828	1.0409	78.162	-52.847	34.64	0.65	3.708	20.476	-27.609	20.809	NA	NA	NA
3324369	347.7812	-0.9702	76.125	-54.458	74.54	2.72	-2.391	42.066	-60.652	42.134	NA	NA	NA
3326202	347.8343	-0.0655	77.187	-53.8	58.02	1.49	0.401	33.414	-46.820	33.416	NA	NA	NA
3326894	347.8542	-1.1080	76.066	-54.611	14.65	0.11	5.957	8.234	-11.942	10.163	-134.032	-255.397	-131.738
3344095	348.3841	-1.1295	76.743	-54.969	70.05	3.80	-1.221	39.139	-57.360	39.158	NA	NA	NA
3346605	348.4620	0.8048	78.934	-53.517	34.18	0.32	4.099	19.946	-27.484	20.363	-181.114	-307.089	-178.712
3348445	348.5209	-0.3093	77.829	-54.424	15.25	0.02	6.129	8.675	-12.407	10.622	-24.775	-147.655	-22.540
3349511	348.5530	0.6968	78.942	-53.658	12.87	0.19	6.537	7.485	-10.367	9.938	NA	NA	NA
3352525	348.6432	-1.0947	77.13	-55.108	24.75	0.38	4.846	13.803	-20.302	14.629	21.615	-98.973	23.712
336651	11.1024	-0.4621	119.022	-63.28	24.97	0.16	13.447	9.817	-22.303	16.649	-74.252	-164.248	-77.750
3381185	349.5450	0.8570	80.442	-54.136	88.43	2.35	-0.602	51.089	-71.665	51.092	NA	NA	NA
3398791	350.1171	0.0919	80.437	-55.091	21.51	0.13	5.955	12.137	-17.638	13.520	-147.729	-269.993	-145.842
3407559	350.4060	0.8795	81.654	-54.629	28.50	0.31	5.605	16.323	-23.239	17.259	NA	NA	NA
3422033	350.8760	-1.2387	80.085	-56.61	13.21	0.03	6.749	7.160	-11.027	9.839	32.135	-85.616	33.649
3422195	350.8805	1.1350	82.578	-54.697	29.23	0.29	5.818	16.750	-23.855	17.732	NA	NA	NA

Table C.3: Kinematic Properties of SDSS RRL (continued)

Variable	RA	Dec	l	b	Dist	Err	X	Y	Z	R	helio	lsr	gsr
3434383	351.2743	-0.9705	80.957	-56.634	79.36	1.02	1.140	43.104	-66.279	43.119	NA	NA	NA
3443067	351.5637	0.0595	82.468	-55.97	17.19	0.10	6.739	9.535	-14.244	11.676	-88.004	-208.543	-86.488
3461129	352.1637	1.0286	84.321	-55.511	9.99	0.67	7.440	5.627	-8.231	9.329	-67.787	-190.254	-66.291
3462783	352.2179	0.4827	83.86	-55.994	31.51	1.18	6.115	17.522	-26.121	18.558	NA	NA	NA
3463795	352.2514	-1.0507	82.32	-57.273	10.40	0.05	7.248	5.574	-8.752	9.144	96.213	-20.469	97.404
3479617	352.7658	1.0608	85.244	-55.815	18.30	0.85	7.147	10.247	-15.138	12.493	NA	NA	NA
3503214	353.5126	-0.5664	84.761	-57.586	32.92	0.21	6.389	17.570	-27.787	18.696	26.455	-90.043	27.391
3507963	353.6576	1.1659	86.692	-56.204	69.44	0.89	5.771	38.561	-57.706	38.990	NA	NA	NA
3527029	354.2493	-0.9451	85.536	-58.305	52.38	0.80	5.858	27.439	-44.571	28.057	46.137	-68.402	46.834
3528959	354.3114	0.1660	86.747	-57.398	38.34	0.63	6.828	20.622	-32.295	21.723	-52.345	-169.857	-51.512
3539383	354.6355	0.8564	87.919	-56.975	51.76	1.66	6.976	28.191	-43.398	29.041	-112.698	-231.675	-111.853
3549941	354.9939	-0.8094	86.878	-58.587	5.61	0.26	7.841	2.921	-4.790	8.367	87.605	-26.363	88.131
3565861	355.5305	0.5480	89.064	-57.693	7.35	0.04	7.936	3.925	-6.208	8.854	-163.225	-280.215	-162.651
3574691	355.8220	1.1742	90.107	-57.289	19.51	1.04	8.020	10.542	-16.414	13.246	-107.362	-225.664	-106.776
3574739	355.8233	-0.4973	88.555	-58.744	70.27	1.52	7.081	36.449	-60.071	37.130	NA	NA	NA
3585054	356.1711	-1.2203	88.431	-59.544	27.06	0.21	7.624	13.713	-23.330	15.690	61.621	-49.679	61.792

Table C.3: Kinematic Properties of SDSS RRL (continued)

Variable	RA	Dec	l	b	Dist	Err	X	Y	Z	R	helio	lsr	gsr
3588816	356.2946	-0.8050	89.049	-59.246	94.49	2.98	7.198	48.311	-81.202	48.844	NA	NA	NA
3605512	356.8411	-0.4845	90.288	-59.233	27.44	0.19	8.071	14.037	-23.579	16.192	-2.541	-114.979	-2.440
3612526	357.0749	-0.0221	91.116	-58.937	9.73	0.07	8.098	5.018	-8.333	9.527	-57.206	-170.596	-57.102
3626602	357.5298	0.7752	92.598	-58.438	16.59	0.04	8.394	8.674	-14.134	12.070	-21.196	-136.133	-21.099
3626894	357.5396	1.0240	92.827	-58.22	8.20	0.11	8.213	4.313	-6.971	9.277	NA	NA	NA
3685041	359.4748	0.0831	95.443	-59.9	25.75	0.19	9.225	12.856	-22.279	15.824	-96.965	-207.293	-97.458
3689799	359.6323	-1.0021	94.82	-60.953	13.56	0.08	8.553	6.560	-11.853	10.779	17.738	-89.381	17.057
3690770	359.6666	0.9649	96.491	-59.171	4.71	0.24	8.273	2.397	-4.042	8.613	70.282	-42.162	69.860
371848	12.3487	-0.2999	121.8	-63.167	21.82	0.20	13.190	8.370	-19.468	15.621	-79.830	-168.013	-83.614
395488	13.2246	-0.3616	123.743	-63.231	49.18	1.65	20.304	18.419	-43.909	27.414	NA	NA	NA
399535	13.3693	-0.7226	124.078	-63.59	23.29	0.08	13.805	8.581	-20.861	16.254	-90.180	-175.322	-94.271
400644	13.4092	-0.0507	124.14	-62.917	15.13	0.15	11.866	5.701	-13.471	13.165	NA	NA	NA
426946	14.3012	-0.0994	126.102	-62.936	32.09	0.47	16.604	11.798	-28.578	20.368	-68.545	-153.655	-72.780
452040	15.1880	-1.0367	128.214	-63.813	14.16	0.54	11.866	4.910	-12.707	12.841	NA	NA	NA
464636	15.6211	-0.0593	128.983	-62.801	11.22	0.50	11.226	3.987	-9.980	11.913	-93.313	-176.030	-97.863
483608	16.2510	-0.3951	130.437	-63.069	65.92	5.39	27.365	22.724	-58.771	35.570	NA	NA	NA

Table C.3: Kinematic Properties of SDSS RRL (continued)

Variable	RA	Dec	l	b	Dist	Err	X	Y	Z	R	helio	lsr	gsr
487671	16.3907	-0.3957	130.743	-63.053	30.27	0.27	16.953	10.393	-26.983	19.885	-52.305	-132.622	-57.087
491136	16.4988	-0.3789	130.975	-63.023	17.49	0.08	13.203	5.990	-15.587	14.498	-34.972	-115.126	-39.778
491216	16.5014	-0.3094	130.962	-62.954	5.20	0.02	9.551	1.787	-4.636	9.717	221.381	141.043	216.584
505091	16.9536	-0.2247	131.921	-62.81	22.75	0.22	14.946	7.735	-20.237	16.829	-77.531	-157.224	-82.425
544842	18.3892	1.0443	134.516	-61.329	9.38	0.26	11.155	3.209	-8.230	11.608	NA	NA	NA
552961	18.6942	0.3458	135.42	-61.959	10.09	0.02	11.379	3.330	-8.908	11.857	69.523	-8.302	64.291
592459	20.2193	-1.0699	139.319	-63.001	68.42	2.36	31.555	20.247	-60.963	37.492	NA	NA	NA
600979	20.5278	-1.1733	140.034	-63.022	17.31	0.13	14.020	5.045	-15.430	14.900	60.627	-9.351	54.756
610690	20.8895	1.0724	139.546	-60.759	24.55	0.24	17.125	7.781	-21.422	18.810	NA	NA	NA
611171	20.9074	-0.8944	140.673	-62.652	9.42	0.08	11.347	2.742	-8.366	11.674	73.581	3.608	67.658
62306	2.0155	-1.0994	99.339	-61.968	59.68	1.24	12.551	27.676	-52.679	30.389	NA	NA	NA
625655	21.4316	1.1757	140.557	-60.517	57.89	3.14	30.003	18.101	-50.393	35.040	NA	NA	NA
636430	21.8099	0.7343	141.549	-60.837	24.51	0.61	17.355	7.428	-21.406	18.878	-102.505	-175.081	-108.416
643347	22.0565	1.2326	141.74	-60.289	27.04	0.37	18.523	8.299	-23.485	20.297	NA	NA	NA
66170	2.1503	0.6596	100.861	-60.363	57.15	0.62	13.325	27.755	-49.673	30.788	NA	NA	NA
675735	23.2017	1.0299	144.06	-60.134	19.15	1.00	15.721	5.597	-16.607	16.687	NA	NA	NA

Table C.3: Kinematic Properties of SDSS RRL (continued)

Variable	RA	Dec	l	b	Dist	Err	X	Y	Z	R	helio	lsr	gsr
683538	23.4703	-0.7507	145.803	-61.723	21.53	0.15	16.435	5.732	-18.959	17.406	189.307	124.234	182.811
708449	24.3785	0.0442	146.981	-60.658	24.60	0.22	18.109	6.570	-21.447	19.264	-85.755	-151.096	-92.351
738258	25.4679	-0.8909	149.785	-61.106	8.42	0.06	11.515	2.047	-7.370	11.695	-91.664	-152.129	-98.632
74164	2.4268	-0.5629	100.549	-61.608	8.71	0.52	8.758	4.071	-7.662	9.658	-8.498	-112.672	-9.830
750838	25.9202	0.5078	149.491	-59.643	18.43	0.07	16.026	4.729	-15.906	16.709	48.376	-14.950	41.496
78440	2.5753	1.1705	102.004	-60.019	9.04	0.24	8.940	4.419	-7.830	9.972	NA	NA	NA
791469	27.3397	-0.2224	152.651	-59.71	20.69	0.13	17.270	4.795	-17.867	17.923	-127.573	-185.846	-134.868
799366	27.5995	0.1770	152.762	-59.236	29.47	0.21	21.403	6.899	-25.324	22.488	-84.556	-143.359	-91.855
80016	2.6295	1.0257	102.015	-60.174	42.95	1.69	12.447	20.894	-37.261	24.320	NA	NA	NA
802624	27.7119	-0.1322	153.23	-59.463	29.83	0.15	21.530	6.826	-25.689	22.586	-99.373	-157.086	-106.738
807309	27.8688	1.2492	152.32	-58.155	21.74	0.24	18.158	5.328	-18.468	18.923	NA	NA	NA
814336	28.1051	-0.2868	154.057	-59.422	11.49	0.05	13.257	2.558	-9.894	13.501	6.371	-50.063	-1.102
819279	28.2632	-0.6407	154.657	-59.662	24.68	1.14	19.268	5.337	-21.303	19.993	-111.686	-166.805	-119.241
823034	28.3804	-0.5718	154.798	-59.546	27.04	0.64	20.401	5.836	-23.309	21.219	NA	NA	NA
833155	28.7091	0.2502	154.613	-58.666	7.83	0.02	11.681	1.747	-6.692	11.810	-64.781	-121.362	-72.313
833759	28.7279	0.0373	154.838	-58.846	23.71	0.22	19.104	5.216	-20.294	19.803	-146.698	-202.655	-154.263

Table C.3: Kinematic Properties of SDSS RRL (continued)

Variable	RA	Dec	l	b	Dist	Err	X	Y	Z	R	helio	lsr	gsr
852716	29.3496	0.5321	155.436	-58.115	29.43	0.19	22.139	6.463	-24.990	23.063	-63.181	-119.122	-70.814
859397	29.5573	1.0287	155.333	-57.579	29.85	0.23	22.545	6.680	-25.201	23.514	-18.194	-75.029	-25.803
86104	2.8377	0.1706	101.861	-61.051	15.97	0.08	9.589	7.567	-13.978	12.215	130.483	24.934	129.147
8668	0.2834	1.1785	97.762	-59.213	25.87	0.20	9.788	13.120	-22.224	16.369	-85.925	-198.050	-86.475
870585	29.9082	1.2229	155.731	-57.241	18.55	1.01	17.150	4.126	-15.600	17.640	NA	NA	NA
878096	30.1311	0.9943	156.297	-57.332	22.33	0.09	19.034	4.844	-18.794	19.641	-122.783	-178.257	-130.520
895587	30.6915	-0.0005	158.134	-57.912	20.54	0.05	18.126	4.064	-17.402	18.576	12.596	-38.924	4.603
902052	30.9132	0.9583	157.581	-56.974	22.90	0.03	19.537	4.760	-19.198	20.108	-119.961	-173.599	-127.870
908314	31.1291	0.3348	158.512	-57.399	30.20	0.18	23.140	5.960	-25.441	23.895	-15.781	-67.241	-23.821
918395	31.4518	0.0290	159.32	-57.491	31.92	0.15	24.047	6.057	-26.914	24.798	-78.275	-128.181	-86.426
924895	31.6758	0.9888	158.746	-56.557	29.61	0.20	23.207	5.915	-24.705	23.949	-75.029	-127.046	-83.095
925246	31.6875	1.1414	158.62	-56.42	30.34	1.67	23.626	6.118	-25.277	24.405	NA	NA	NA
937681	32.1047	-0.5790	160.957	-57.652	33.04	0.42	24.711	5.768	-27.913	25.375	NA	NA	NA
946940	32.4193	-0.0368	160.894	-57.026	20.85	0.15	18.725	3.715	-17.495	19.090	-130.408	-177.963	-138.771
956269	32.7173	0.6319	160.683	-56.304	16.95	0.17	16.874	3.111	-14.102	17.159	NA	NA	NA
95875	3.1739	-0.4607	102.107	-61.756	17.20	0.03	9.707	7.958	-15.152	12.553	NA	NA	NA

Table C.3: Kinematic Properties of SDSS RRL (continued)

Variable	RA	Dec	l	b	Dist	Err	X	Y	Z	R	helio	lsr	gsr
959039	32.8022	0.1534	161.287	-56.657	22.70	0.22	19.817	4.003	-18.963	20.218	NA	NA	NA
98085	3.2444	0.2189	102.691	-61.132	9.41	0.01	8.998	4.430	-8.237	10.029	-62.060	-167.113	-63.493
982175	33.5526	0.6605	161.902	-55.818	14.70	0.09	15.852	2.566	-12.163	16.058	108.376	61.477	99.873
98405	3.2547	-0.5841	102.187	-61.899	31.28	0.46	11.110	14.402	-27.593	18.189	NA	NA	NA
990804	33.8388	-0.8656	163.901	-56.907	27.24	0.32	22.290	4.124	-22.821	22.668	83.479	41.401	74.710

BIBLIOGRAPHY

REFERENCES

Adelman-McCarthy, J. K., et al. 2008, ApJS, 175, 297

Akerlof, C., et al. 1994, ApJ, 436, 787

Akerlof, C., et al. 2000, AJ, 119, 1901

Allende Prieto, C., Beers, T. C., Wilhelm, R., Newberg, H. J., Rockosi, C. M., Yanny, B., & Lee, Y. S. 2006, ApJ, 636, 804

Bailey, S. I., & Pickering, E. C. 1902, Annals of Harvard College Observatory, 38, 1

Beers, T. C. 1990, AJ, 99, 323

Beers, T. C., Kage, J. A., Preston, G. W., & Shectman, S. A. 1990, AJ, 100, 849

Beers, T. C., & Sommer-Larsen, J. 1995, ApJS, 96, 175

Bekki, K., & Chiba, M. 2001, ApJ, 558, 666

Belokurov, V., et al. 2006, ApJ, 642, L137

Belokurov, V., et al. 2007, ApJ, 654, 897

Bono, G., Caputo, F., & di Criscienzo, M. 2007, A&A, 476, 779

Bowell, E., Koehn, B. W., Howell, S. B., Hoffman, M., & Muinonen, K. 1995, Bulletin of the American Astronomical Society, 27, 1057

Bramich, D. M., et al. 2008, ArXiv e-prints, 801, arXiv:0801.4894

Bullock, J. S., & Johnston, K. V. 2005, ApJ, 635, 931

Butler, D. 1975, ApJ, 200, 68

Cacciari, C., Corwin, T. M., & Carney, B. W. 2005, AJ, 129, 267

Carollo, D., et al. 2007, Nature, 450, 1020

Catelan, M. 2005, ArXiv Astrophysics e-prints, arXiv:astro-ph/0507464

Chiba, M., & Beers, T. C. 2000, AJ, 119, 2843

Chiba, M., & Yoshii, Y. 1998, AJ, 115, 168

Clem, J. 2005, Ph.D. Thesis, Univ. of Victoria

Clement, C. M., & Shelton, I. 1999, ApJ, 515, L85

Clement, C. M., & Rowe, J. 2000, AJ, 120, 2579

Clementini, G., Gratton, R., Bragaglia, A., Carretta, E., Di Fabrizio, L., & Maio, M. 2003, AJ, 125, 1309

Cook, K. H., et al. 1995, IAU Colloq. 155: Astrophysical Applications of Stellar Pulsation, 83, 221

Cox, J. P., & Whitney, C. 1958, ApJ, 127, 561

Demarque, P., Zinn, R., Lee, Y.-W., & Yi, S. 2000, AJ, 119, 1398

Eddington, A. S. 1926, The Internal Constitution of the Stars, Cambridge: Cambridge University Press, 1926

Eggen, O. J., Lynden-Bell, D., & Sandage, A. R. 1962, ApJ, 136, 748

Freeman, K. C. 1996, Formation of the Galactic Halo...Inside and Out, 92, 3

Freeman, K. C., & Rodgers, A. W. 1975, ApJ, 201, L71

Frenk, C. S., & White, S. D. M. 1980, MNRAS, 193, 295

Frieman, J. A., et al. 2008, AJ, 135, 338

Fukugita, M., Ichikawa, T., Gunn, J. E., Doi, M., Shimasaku, K., & Schneider, D. P. 1996, AJ, 111, 1748

Gray, R. O., & Corbally, C. J. 1994, AJ, 107, 742

Gunn, J. E., et al. 1998, AJ, 116, 3040

Helmi, A. 2008, A&A Rev., 15, 145

Ibata, R. A., Gilmore, G., & Irwin, M. J. 1994, Nature, 370, 194

Ivezić, Ž., Vivas, A. K., Lupton, R. H., & Zinn, R. 2005, AJ, 129, 1096

Ivezić, Ž., et al. 2007, AJ, 134, 973

Jeffery, E. J., Barnes, T. G., III, Skillen, I., & Montemayor, T. J. 2007, ApJS, 171, 512

Jones, R. V., Carney, B. W., & Latham, D. W. 1988, ApJ, 332, 206

Jurcsik, J., & Kovacs, G. 1996, A&A, 312, 111

Kemper, E. 1982, AJ, 87, 1395

Kholopov, P. N., et al. 1998, Combined General Catalogue of Variable Stars, 4.1 Ed (II/214A). (1998), 0

Kinemuchi, K., Smith, H. A., Woźniak, P. R., & McKay, T. A. 2006, AJ, 132, 1202

King, D. S., & Cox, J. P. 1968, PASP, 80, 365

Kinman, T. D., Cacciari, C., Bragaglia, A., Buzzoni, A., & Spagna, A. 2007, MNRAS, 375, 1381

Klypin, A., Kravtsov, A. V., Valenzuela, O., & Prada, F. 1999, ApJ, 522, 82

Layden, A. C. 1994, AJ, 108, 1016

Layden, A. C. 1995a, AJ, 110, 2288

Layden, A. C. 1995b, AJ, 110, 2312

Layden, A. C. 1998, AJ, 115, 193

Lee, J.-W., & Carney, B. W. 1999, AJ, 118, 1373

Lee, Y. S., et al. 2007, ArXiv e-prints, 710, arXiv:0710.5645

Liu, T. 1991, PASP, 103, 205

Lomb, N. R. 1976, Ap&SS, 39, 447

Majewski, S. R., Skrutskie, M. F., Weinberg, M. D., & Ostheimer, J. C. 2003, ApJ, 599, 1082

Massey, P., Valdes, F., & Barnes, J. 1992, A User's Guide to Reducing Slit Spectra with IRAF, Apr 1992

Massey, P. 1997, A User's Guide to CCD Reductions with IRAF, Feb 1997

Miceli, A., et al. 2008, ApJ, 678, 865

Mihalas, D., & Binney, J. 1981, San Francisco, CA, W. H. Freeman and Co., 1981. 608 p.

Minniti, D., & Zoccali, M. 2007, ArXiv e-prints, 710, arXiv:0710.3104

Moore, B., Ghigna, S., Governato, F., Lake, G., Quinn, T., Stadel, J., & Tozzi, P. 1999, ApJ, 524, L19

Morgan, S., Wahl, J., & Wieckhorst, R. 2006, Memorie della Societa Astronomica Italiana, 77, 178

Morrison, H. L., Flynn, C., & Freeman, K. C. 1990, AJ, 100, 1191

Newberg, H. J., et al. 2002, ApJ, 569, 245

Nikolov, N. S., Bukhantsova, N., & Frolov, M. 1984, Sofia : Sofiiski universitet "Kliment Okhridski", 1984.

Oosterhoff, P. T. 1939, The Observatory, 62, 104

Ostlie, D. A., & Carroll, B. W. 1996, An Introduction to Modern Stellar Astrophysics, by D.A. Ostlie and B.W. Carroll. Benjamin Cummings, 1996. ISBN 0-201-59880-9.

Peacock, J. A. 1999, Cosmological Physics, by John A. Peacock, pp. 704. ISBN 052141072X. Cambridge, UK: Cambridge University Press, January 1999.

Press, W. H., & Rybicki, G. B. 1989, ApJ, 338, 277

Press, W. H., Teukolsky, S. A., Vetterling, W. T., & Flannery, B. T. 1992 Numerical Recipies in C, Cambridge, New York: Cambridge University Press

Preston, G. W. 1959, ApJ, 130, 507

Preston, G. W., Shectman, S. A., & Beers, T. C. 1991, ApJ, 375, 121

Pritzl, B. J., Smith, H. A., Catelan, M., & Sweigart, A. V. 2001, AJ, 122, 2600

Quinn, P. J., & Goodman, J. 1986, ApJ, 309, 472

Rattenbury, N. J., Mao, S., Sumi, T., & Smith, M. C. 2007, MNRAS, 378, 1064

Reimann, J. 1994, Ph.D. Thesis, Univ. Cal., Berkeley

Rest, A. 2002, Ph.D. Thesis

Robin, A. C., Reylé, C., Derrière, S., & Picaud, S. 2003, A&A, 409, 523

Sandage, A., & Wildey, R. 1967, ApJ, 150, 469

Sandage, A. 1993, AJ, 106, 703

Sandage, A. 1993, AJ, 106, 687

Sandage, A. 2004, AJ, 128, 858

Scargle, J. D. 1982, ApJ, 263, 835

Schlegel, D. J., Finkbeiner, D. P., & Davis, M. 1998, ApJ, 500, 525

Searle, L., & Zinn, R. 1978, ApJ, 225, 357

Sesar, B., et al. 2007, AJ, 134, 2236

Simon, N. R., & Lee, A. S. 1981, ApJ, 248, 291

Simon, N. R., & Teays, T. J. 1982, ApJ, 261, 586

Smith, H. A. 1986, PASP, 98, 1317

Smith, H. A. 1995, Cambridge Astrophysics Series, Cambridge, New York: Cambridge University Press, —c1995

Smith, J. A., et al. 2002, AJ, 123, 2121

Stellingwerf, R. F. 1978, ApJ, 224, 953

Stetson, P. B. 1996, PASP, 108, 851

Stetson, P. B. 1987, PASP, 99, 191

Stoughton, C., et al. 2002, AJ, 123, 485

Suntzeff, N. B., Kinman, T. D., & Kraft, R. P. 1991, ApJ, 367, 528

Sweigart, A. V., & Catelan, M. 1998, ApJ, 501, L63

Tody, D. 1986, Proc. SPIE, 627, 733

Tody, D. 1993, Astronomical Data Analysis Software and Systems II, 52, 173

van Albada, T. S., & Baker, N. 1973, ApJ, 185, 477

van den Bergh, S. 1967, AJ, 72, 70

Vivas, A. K., et al. 2004, AJ, 127, 1158

Vivas, A. K., & Zinn, R. 2006, AJ, 132, 714

Welch, D. L., & Stetson, P. B. 1993, AJ, 105, 1813

West, A. 2008, (Private Communication)

White, S. D. M., & Rees, M. J. 1978, MNRAS, 183, 341

Wilhelm, R., Beers, T. C., & Gray, R. O. 1999, AJ, 117, 2308

Wilhelm, R., et al. 2007, ArXiv e-prints, 712, arXiv:0712.0776

Woźniak, P. R., et al. 2004, AJ, 127, 2436

York, D. G., et al. 2000, AJ, 120, 1579

Zhao, C., & Newberg, H. J. 2006, ArXiv Astrophysics e-prints, arXiv:astro-ph/0612034

Zhevakin, S. A. 1953, Astr. Zh. 30, 161

Zinn, R. 1980, ApJ, 241, 602

Zinn, R. 1986, ApJ, 304, 579

Zinn, R. 1985, ApJ, 293, 424

Zinn, R. 1993, The Globular Cluster-Galaxy Connection, 48, 38

Zoccali, M., Hill, V., Lecureur, A., Barbuy, B., Renzini, A., Minniti, D., Gomez, A., & Ortolani, S. 2008, ArXiv e-prints, 805, arXiv:0805.1218